Hassan Noor Khan, M.Sc.

Measurement Based Backscatter RFID System Analyzer for Tag Localization

DOCTORAL THESIS

to achieve the university degree of

Doktor der technischen Wissenschaften

submitted to

Graz University of Technology

Supervisor

Univ.-Prof. Dipl.-Ing. Dr.techn. Wolfgang Bösch

Institute of Microwave and Photonic Engineering

Assoc. Prof. Dr. Pavel Nikitin
(University of Washington & Honeywell Inc.)

Graz, May 2017

AFFIDAVIT

I declare that I have authored this thesis independently, that I have not used other than the declared sources/resources, and that I have explicitly indicated all material which has been quoted either literally or by content from the sources used. The text document uploaded to TUGRAZonline is identical to the present doctoral thesis.

Signature: _____

Date: _____

Dedication

To my parents,
Dr. Noor-ul-Islam Khan and Mrs. Qaiser Noor.
They nourished, nurtured and polished me so that I can reach this point!

A Comparison of Selected Analyses for Estimating Environmental Variation in Early Generations and Advanced Lines of Wheat (Triticum aestivum L. em thell)

by

Noor-ul Islam Khan

A THESIS

submitted to

Oregon State University

in partial fulfillment of
the requirement for the degree of

Doctor of Philosophy

Completed March 6, 1987

Commencement June, 1987

Oregon State University, 1987 to Graz University of Technology, 2017.
The legacy continues...

Acknowledgments

Pursuing a PhD has been a childhood dream for me, aptly delineated by the picture of me and my father on the dedication page. There have been many personalities during the course of my educational journey, starting from the Harding Elementary School in Corvallis, Oregon, USA to over here at the Graz University of Technology, Graz, Austria.

First and foremost, I express indebtedness to my doctoral supervisor Univ.-Prof. Dipl.-Ing. Dr.techn. Wolfgang BÖSCH, Head of the Institute of Microwave and Photonic Engineering (Institut für Hochfrequenztechnik, IHF). He has been motivating, encouraging, and enlightening over the course of the past 4 years. We first got in contact in 2010, with my arrival in Graz being delayed due to some administrative factors. I am thankful to him for his patience and keeping faith in me. Moreover, I am obliged for being employed for 2 years as a University Project Assistant under the project *SeCoS*.

Secondly, I am grateful to my external supervisor Dr. Pavel NIKITIN, Principal RF Engineer, Honeywell, USA & Affiliate Associate Professor, University of Washington. His review and technical comments for my thesis were of great value. It's an honor to have your name on my thesis.

The major part of learning which I have achieved over the past 4 years, is owed to my co-supervisor Dipl.-Ing. Dr.techn. Jasmin GROSINGER. Being your mentee, it has been a wonderful and learnable experience. You have really invigorated my passion for research and have sharpened my writing skills. Beholden I am, really describes my feelings for your contribution and guidance over the course of the past 4 years.

I am thankful to both of the Higher Education Commission of Pakistan and the Austrian Research Promotion Agency for supporting my doctoral studies.

At the IHF, there are many personalities whom I want to say thanks for their roles in the past 4 years. I came to know Ao.Univ.-Prof. Dipl.-Ing. Dr.techn. Erich LEITGEB in 2010. He has been very kind and cooperative, especially in the initial months of my stay in Graz, back in 2013. It was always a pleasure to have a chat with Asst.Prof. Dipl.-Ing. Dr.techn. Michael GADRINGER. He always catered my requests for new books to be purchased. I appreciate the technical support provided by Ing. Andreas MERDONIG and Mr. Dominik AMSCHL. As IT guys, they were always there to help in a crisis, from a hard disk failure to the purchase of a new software. It's because of their timely support that I always had the most updated version of Matlab! Ms. Gabriele MÖRTH as the Institute's secretary has always been helpful in the administrative affairs. I was fortunate to have some good colleagues at work. When I started in May 2013, my office-mates Dipl.-Ing. Dr.techn. Bernhard AUINGER and Dipl.-Ing. Philipp FREIDL, both were accommodating and it was an enjoyable room environment. It was really a

pleasure sharing space with you guys. Special thanks to my colleague Dipl.-Ing. Lukas GÖRTSCHACHER, as part of the RFID group at IHF, we developed a good rapport and were able to achieve productive research. The discussions I had with you during the last past year, always helped me in getting rid of ambiguities. A special mention for helping me out in the channel measurements last year in the IHF lab. I wish you best of luck for your dissertation.

It was an honor for me to serve as the student representative of the Doctoral School of Information and Communications Engineering (ICE). I thank Univ.-Prof. Dipl.-Ing. Dr.techn. Gernot KUBIN, Head of the Co-ordination team of the Doctoral School of ICE. I am also appreciative for the administrative help tendered by Ms. Astrid BRODTRAGER and Ms. Alexandra ZAVEC at the Dean's Office of the Faculty of Electrical and Information Engineering.

Prof. Dr. Noor M. SHEIKH, former Dean and Professor at the Faculty of Electrical Engineering, University of Engineering & Technology (UET) Lahore, Pakistan has been a source of guidance ever since the start of my bachelor studies in the year 2000. Your students have been paying homage to you for the past 4 decades. My senior at UET and colleague at the FAST-National University of Computer & Emerging Sciences (FAST-NUCES), Pakistan, Prof. Dr. Sheikh M. SAJID has been the connection between me and Graz. As a former student here at the IHF, you have left an inspiring legacy. The connection of you, Dr. Noor and Dr. Erich was instrumental in me landing here in Graz for my PhD.

On social front in Graz, I wish to pay my due regards to Mr. Mohammed Musheerul ISLAM, M.Sc., Project Manager AVL Graz. You and your family have been always there for us in the hour of need. You were always proactive in passing on your relevant experience, for helping our settlement in Graz. We travel to different places and make new friends. I have enjoyed the company of Mr. Waqas AHMED, NFC Firmware Engineer NXP Semiconductors, Graz. You always contrived opportunities, be it a cricket match or a day's trip outside Graz. It always helped me to freshen up my mind. Mr. Dr. Doris WIESAUER, my general physician deserves to be thanked for her medical assistance for me and my family since 2013.

To be honest, I have reached this stage in the pursuit of my father Dr. Noor-ul-Islam KHAN's dream. You have always been an inspiration to me. Be it your Doctorate in my childhood, your ascension to the ultimate post of Director General of Ayub Agricultural Research Institute in Faisalabad, Pakistan in my youth and recently being the Chief Executive of the Punjab Agricultural Research Board, Pakistan, you have always inspired me in more than one way. I have always been under this pressure of being your eldest son. The expectations from me were always high, may be beyond what I could have mustered up. I am glad that I am able to full fill your long-standing unfulfilled

dream in life. My mother, Mrs. Qaiser Noor is the one who has taught me the basics of life. I strongly believe, it's her interpersonal skills that have filled the gap which my father lacked (outside the professional world!). Her love, affection, and dedication to the cause of my father's career, education of me and my siblings can't be expressed in words. Love you Maa. I also appreciate the blessings of my father-in law, Mr. Sheikh Afzaal Ahmad. His tranquil nature has always inspired me to live a peaceful and easy going life.

Being the eldest son of my family, there were many things I was taking care of. I am grateful to my brother-in law, Mr. Muhammad Sohaib Miraj and my brothers Ahsan Noor Khan, M.Sc. and Mr. Zeeshan Noor Khan. They have been taking care of me and my family's social obligations amicably over the past 4 years. I wish good luck to Ahsan for his doctoral studies a the Queen Mary University of London. It took 30 years to bring the 2nd PhD in our family, I hope it will only take 3 more years for the third one.

Last but not least, it's the love of my wife, Mrs. Zaira Mairaj which has kept me going in the pursuit of my dream for the past many years. You have truly been a huge support system for me, especially during these past 4 years over here in Graz. I hope, once I am done with my studies, our roller-coaster life will become more stable. It's a blessing to have kids, Miss Mahnoor and Master Jasim. They have been the source of joy and eternal bliss, ever-since they arrived in our lives. Mahnoor, I promise to spend more time with you and Jasim, and will be more involved in your activities.

Hasan Noor Khan
May 2017,
Graz, Austria.

ABSTRACT

Measurement Based Backscatter RFID System Analyzer for Tag Localization

Ubiquitous computing coupled with the need of indoor localization has enabled the adaptation of ultra-high frequency radio frequency identification (RFID) technology. Low cost of batteryless RFID tags (and their long life), less maintenance, light weight and practically limitless identification scope are the salient features substantiating the adaptation of RFID based localization systems.

For any engineering design, system level simulators provide a reasonable insight of the prospective hardware performance. Making the simulator a measurement based, further enhances the accuracy of results.

In this thesis, I describe the design of a measurement based system analyzer in Matlab®/ Simulink® for estimating the direction of arrival (DoA) and the range of an RFID tag. The intended usage of this measurement based system analyzer in this thesis is for RFID tag localization in a severe multipath environment. The advantages of the system analyzer are its flexibility in changing the design parameters and different design topologies. The radio frequency (RF) components are developed in the SimRF™ toolbox of Simulink®, thus replicating real RF components.

The DoA and the range estimation is based on the techniques of space-domain phase difference of arrival and frequency-domain phase difference of arrival, respectively. Furthermore, the system analyzer is utilized for testing the theoretical concept of multifrequency based phase difference of arrival. Two wireless channel measurement campaigns are discussed in the thesis, based on these measurements the performance of the system analyzer is discussed. The system analyzer performance has also been verified by incorporating channel measurements inside an anechoic chamber.

Contents

List of Figures

List of Tables

Abbreviations

ASK	**a**mplitude **s**hift **k**eying.
CRT	**C**hinese **r**emainder **t**heorem.
CTF	**c**hannel **t**ransfer **f**unction.
CW	**c**ontinuous **w**ave.
DoA	**d**irection **o**f **a**rrival.
FD-PDoA	**f**requency **d**omain **p**hase **d**ifference **o**f **a**rrival.
IoT	**i**nternet **o**f **t**hings.
IQ	**i**nphase **q**uadrature phase.
LoS	**l**ine **o**f **s**ight.
MF-PDoA	**m**ulti-**f**requency **p**hase **d**ifference **o**f **a**rrival.
MIMO	**m**ultiple**i**nput **m**ultiple-**o**utput.
NLoS	**n**on-**l**ine **o**f **s**ight.
PDoA	**p**hase **d**ifference **o**f **a**rrival.
PDP	**p**ower **d**elay **p**rofile.
RF	**r**adio **f**requency.
RFID	**r**adio **f**requency **i**dentification **s**ystem.
RMSE	**r**oot **m**ean **s**quare **e**rror.
RMS	**r**oot **m**ean **s**quare.
RSS	**r**eceived **s**ignal **s**trength.
RX	**r**eceive.
SD-PDoA	**s**pace **d**omain **p**hase **d**ifference **o**f **a**rrival.
SIMO	**s**ingle-**i**nput **m**ultiple-**o**utput.
SISO	**s**ingle-**i**nput **s**ingle-**o**utput.
tag	transponder.
TX	**t**ransmit.
UHF	**u**ltra **h**igh **f**requency.

ULA **u**niform **l**inear **a**rray.

VNA **v**ector **n**etwork **a**nalyzer

List of Latin Symbols

a	distance between centers of RX1 and RX2 antennas.
f	frequency.
h	channel coefficient (tag signal).
h^b	backward (reverse) channel attenuation.
h^f	forward channel attenuation.
k	wave number.
L	complex valued carrier leakage.
M	number of carrier frequencies in MF-PDoA technique.
$m(t)$	modulation function.
$n^{pb}(t)$	passband noise signal.
N_o	noise power spectral density.
$P(\tau)$	power delay profile.
P_{LoS}	power of the line of sight component.
$P_{\text{multipath}}$	power of multipath components.
R	range.
$S-$	scattering parameters.
S_{Abs}	Absorb state.
S_{Ref}	Reflect state.
t	time.
$x^{pb}(t)$	passband signal.
x_{CW}	continuous carrier wave.
x_{RX}	backscattered received signal at the RFID reader.
x_{Tag}	received signal at tag.

List of Greek Symbols

α	incidence angle.
η	modulation efficiency.
λ	wavelength.
ν	power transmission coefficient.
ξ_k	coprime number.
ρ	reflection coefficient.
τ	time delay.
τ_{m}	mean delay spread.
τ_{RMS}	RMS delay spread.
ϕ	DoA.
ψ	tag signal phase.
ψ^b	phase shift of backward (reverse) channel.
ψ^f	phase shift of forward channel.
ψ^{leak}	phase of the carrier leakage signal.
$\psi^{\Delta\sigma}$	phase shift due to tag modulation.
ω	angular frequency.
Δf	frequency separation between two different carrier frequencies.
ΔF	maximum separation between the highest and lowest frequencies in MF-PDoA.
$\Delta\psi$	phase difference.
$\lvert\Delta\sigma\rvert$	normalized radar cross section area of tag.

Chapter 1

Introduction

1.1 Historical Perspective

It is well established that backscatter modulation is the linchpin of ultra-high frequency (UHF) radio frequency identification (RFID) technology. Retrospectively, the origins of backscatter communication can be traced back to the times of Alexander Graham Bell [1]. Bell invented the photophone, intended for passive wireless audio communication. The device communicated audio signals by concentrating ambient light onto a mirrored reflecting surface. The sound waves (to be communicated) supplied to the mirror made it to vibrate, consequently modulating the reflected beam of light. The accompanied receiver of the photophone employed a photosensitive material to demodulate the incident modulated light beam and drawing accordingly a time-varying current into an earphone. Therefore, reproducing the transmitted audio signal. The photophone was able to deliver messages over a distance of 214 meters.

The early 20th century witnessed a furtherance in the backscatter technology, with the light source replaced by a radio frequency (RF) source. Leon Theremin is credited for inventing the first ever passive audio backscatter RF system operating in the UHF frequency range [2]. It was quite a long-range eavesdropping device known as the "The Great Seal Bug," presented in 1945 to the U.S Ambassador to the Soviet Union [3, 4]. Theremin's ingenious design based on transmitting an audio speech signal by using sound waves to deform a thin wall of a cavity resonator which in turn detunes a monopole whip antenna [5].

Due to the sensitive nature of Theremin's work, the exact date of his invention is not

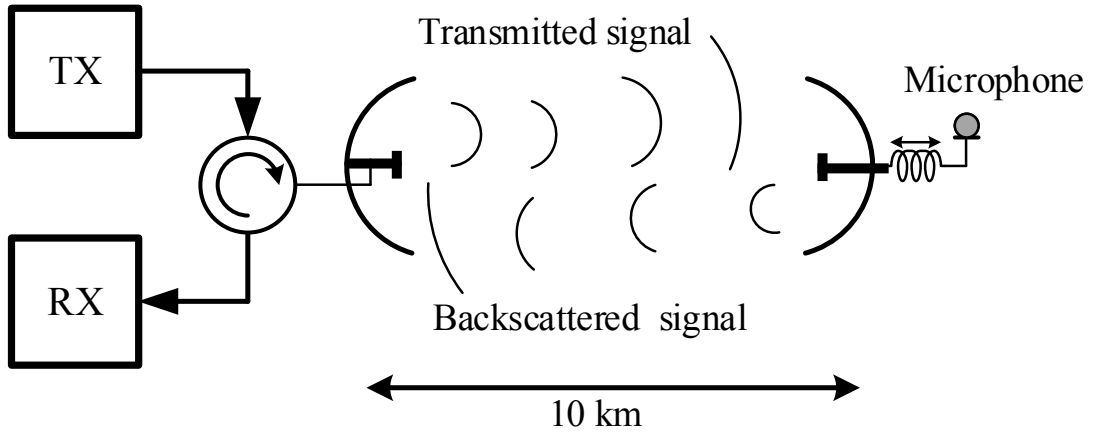

FIGURE 1.1: Basic backscatter modulation system [6].

clear. His contemporary researcher, H. Stockman investigated backscatter modulation in his seminal paper in 1948 [7]. Figure 1.1 shows one of his designs [6]. Stockman employed a conventioanl microphone and speaker coil to modulate the lateral-position of a receiving antenna as per the sound waves received by the microphone attached to the receiving antenna. This so called positional modulation resulted in the signal being reflected back to the transmitter where the sound wave is demodulated and reproduced. Stockman named this technology as "Number Identification Systems" (NIS) and it can be stated that his NIS is the precursor to today's RF identification systems, i.e., RFID.

Fast forwarding the time to the last decade of the 20th century and the early 2000's, there are few noticeable events which changed the landscape of RFID technology. It was at Massachusetts Institute of Technology, U.S in 1997 that Kevin Ashton, Sanjay Sarma, Sunny Siu and David Brock collaborated to form an RFID based research consortium called the Auto-ID Center. The target of their research was to create a global open standard system to facilitate deployment of RFID in any region in the world [8]. Later on, they renamed their research group as Auto-ID Labs [9]. In 2003, Wal-Mart made it mandatory for its top 100 suppliers to furnish RFID enabled shipments by the beginning of 2005 [10, 11]. From a commercial point of view, this facilitated the rapid adaptation of the RFID technology in the mainstream business, especially in the inventorying and supply chain management.

Contemporary research has enabled the RFID technology being incorporated in many useful applications [12, 13]. Advancement in cost-effective chip manufacturing has helped

RFID to compete with the cheap barcode technology. RFID is still not as cheap as traditional labeling technologies. However, added services can be achieved if RFID technology is adopted. Most sought after applications have been in areas such as payment systems, access control, communication and transportation, sensors and metering applications, distribution logistics, parcel and document tracking, automotive systems, livestock/pet tracking, and hospitals/pharmaceutical applications [14–18].

RFID also has the adequacy to initiate novel applications and contribute towards the venture Internet of Things (IoT) [19, 20], thus initiating new enabling technologies. IoT is a scheme which will enable ubiquitous computing by assigning distinct identifiers to humans, objects and animals. The scheme will enable data transfer over a network without human-to-human or human-to-computer interaction [21]. Coincidentally, it was Kevin Ashton who coined the term of IoT in 1999 [22]. It is predicted that IoT will have passive (batteryless) RFID tags as a main constituent. However, some technicalities have to be resolved before this concept matures [23]. Identity and location are the two parameters at the core of every RFID based localization system. For optimum performance of RFID systems, identification is to be linked with localization. Keeping the cost-benefit ratio in consideration, the best choice is to employ passive tag technology which relies on backscatter modulation.

1.2 Motivation and Relevant Research

The dawn of IoT enabling technologies incorporating RFID technology will turn our planet into a connected World [21, 24–28]. These overwhelming new possibilities of information and communication technologies are accompanied by an increased demand for security and privacy. While connectivity of everyday things is the foundation of the IoT, pure connectivity on its own does not automatically provide any added value for humans. There have to be applications benefiting the social needs. This was the main theme of the cooperative research project "***SeCoS***: **Se**cure **Co**ntactless **S**phere–Smart RFID-Technologies for a Connected World[1]."

RFID tag positioning is a crucial prerequisite for many wireless sensing applications such as asset tracking, industrial automation, and home care and healthcare systems. In indoor environments, the layout structure and moving objects give rise to a severe

[1]SeCoS was funded by the Austrian Research Promotion Agency (FFG).

multipath radio propagation environment. Hence, it will affect the accuracy of the indoor positioning. A multiple-input multiple-output (MIMO) RFID reader allows combating these phenomena and thus improves the positioning precision of the RFID system [29].

Under the auspices of the SeCoS project, there was an application to achieve coarse-grained localization of RFID tags inside an engine test bed facility at AVL, Graz. The project included a work package for the design and realization of a prototype MIMO RFID reader suitable for positioning of RFID tags. An initial channel measurement campaign in a realistic, reproducible test scenario was the starting point for the investigation. Based on this, a MIMO RFID reader system analyzer (simulator) was to be designed that localizes UHF RFID tagged objects in severe industrial multipath environments, i.e., like an engine test bed facility at AVL in Graz.

The advancement in computer technology has enabled a reasonable growth in the field of simulation theory. Simulation platforms can be termed as software brassboards [30]. They facilitate in constructing virtual communication systems for further exploration. It allows system parameters to be easily tweaked. The result of such modifications can be promptly evaluated by using interactive and graphical displays of the simulation results.

Modern communication system design process can be categorized into two phases, i.e., the system design process and the deployment process. Simulation is used extensively during both of these two phases of the overall design flow. Primarily, simulations are used for performance evaluation, design tradeoff studies and parameter optimization. Moreover, after the system deployment in the field, simulations come handy in analyzing test procedures, end-of-life predictions, and anomaly investigations [30].

Different simulation tools have been reported, which can be categorized based on what they are designed for. I will be restricting the survey only to system level simulators. SERFID [31] models the entire RFID system including the numerous hardware tags and readers and their electromagnetic environment. The communication links between each tag and reader are modeled using high level functional models (timed transaction level model). SERFID is basically a fault simulator that provides fault detection in critical RFID systems operating in harsh environments (railway, aeronautic, food production, product manufacturing).

A quite advanced open-source system is the PARIS Simulation Framework [32, 33]. It is a complex time-domain system level simulator built in MATLAB which features tag behavioral models and hybrid ray tracing/stochastic RF propagation channel models.

The PARIS Simulation Framework is quite demanding as far as computational power is concerned. There are some simulation frameworks which concentrate on a specific component of an RFID system, like for tags [34, 35] and for RFID antennas [36]. The platform of RFIDSim [37–39] is an open source simulator based on ISO/IEC 18000-6C (EPCglobal Class-1 Gen-2) protocol [8, 40, 41], having a discrete event simulation core [42]. It provides physical models based on Rician fading and a nonlinear tag behavior. Another system level tool is the ASD Kit and Library [43, 44], which is developed and sold by CISC Semiconductor. It is a simulation/emulation tool with emphasis on tag modeling.

In wireless systems realm, there are consequential differences between computer based simulations and physical channel measurement based simulations. As simulation models based on numerically generated data or by using some approximate channel models [45–47], can only incorporate an approximation of the wireless channel in question. By conducting channel measurements, we can capture the true behavior of a wireless channel [48, 49]. The wireless channel can be probed in both of the time and the frequency-domains [50]. Elektrobit Propsound CS^{TM} MIMO channel sounder [51, 52] reproduces the real-world propagation phenomena such as multipath fading, sliding delays, attenuation, path loss, Doppler shift, shadowing and noise. It enables systematic, repeatable testing of wireless systems in realistic, time variant conditions in laboratory [53]. It is tempting to claim that channel measurements provide the real answer to what the system performance will be, since it is based on actual physical hardware.

1.3 Signal Representation

In this section, I will explain the signal constellation model based on [54]. The RF frontend antenna configuration defines the isolation between the forward and reverse channels in RFID systems [55]. Two main choices for the RF frontend antenna configuration are bistatic and monostatic, aptly explained in [6, 55–57]. The signal constellation model of [54] is based on a bistatic RF frontend design. Therefore, I will deliberate upon a bistatic single-input single-output (SISO) RFID system. Then the SISO signal model will be extended to a bistatic single-input multiple-output (SIMO) system.

1.3.1 SISO RFID System

Passive RFID communication relies on backscatter communication from the transponder (tag) to the reader receiver [58, 59]. As the tag is passive (batteryless), the energy required to wake up the tag is supplied by the reader via transmitting a continuous carrier wave. This continuous carrier also leaks into the receiver antennas. As in backscatter RFID communication we have a dyadic (two way) channel, which we can bifurcate, i.e., the channel from the reader-transmitter to the tag as the forward channel and the channel from the tag to the reader-receiver as the reverse channel (or uplink) [60]. A generic, i.e., SISO RFID system is depicted in Figure 1.2. A comprehensive baseband signal formulation is detailed in [54]. The transmitted continuous carrier wave (CW) is:

$$x_{\mathrm{CW}} = \sqrt{2}\sin(\omega_c t), \tag{1.1}$$

where $\omega_c = 2\pi f_c$ is the angular frequency and f_c is the chosen carrier frequency in Hertz.

As explained in the preceding paragraph, passive RFID tags harvest energy from the incident carrier wave. The consequence of this is a substantial leakage of the transmitted CW into the RFID reader receiver. [54] has devised an ingenious method to separate the carrier leakage and tag signal. We can define the static carrier leakage as

$$x_{\mathrm{L}} = \sqrt{2}|L|\sin(\omega_c t + \psi^{leak}), \tag{1.2}$$

where ψ^{leak} is the phase shift resulting from the propagation delay between the transmit and receive antennas. The magnitude of $|L|$ depends whether we are using a monostatic or bistatic antenna configuration. As for a monostatic setup, there is a single common

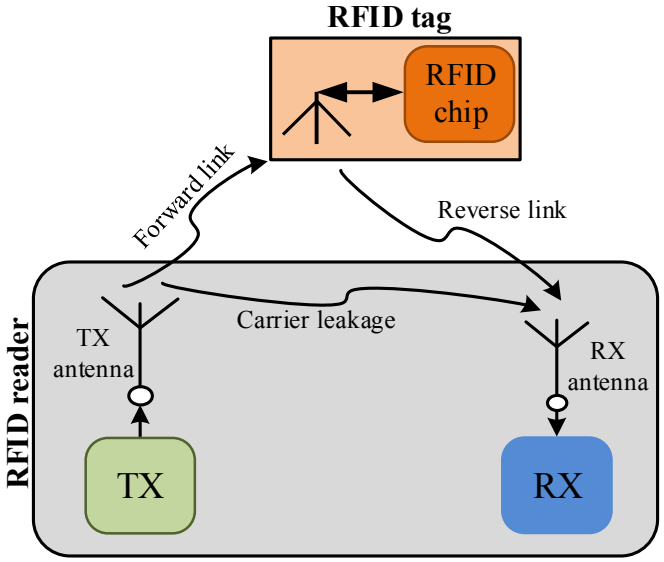

FIGURE 1.2: A bistatic SISO RFID system.

antenna for both of the transmit (TX) and receive (RX) channels. Both of these are separated by a circulator or a directional coupler. Consequence of a monostatic configuration is a strong correlation between uplink and downlink communication channels. Contrary to this, in a bistatic antenna setup we have a separate antenna for both of the TX and RX. In this case, the magnitude of correlation between the uplink and downlink channels depends on the antenna separation between the TX and RX antennas.

In UHF backscatter RFID communication, predominantly, the tag employs amplitude shift keying (ASK) as the modulation scheme to send data (tag ID) back to the RFID reader receiver RX. Most often, pure ASK is not suitable and special pulse shaping filters (e.g., raised cosine) are normally utilized to enhance the spectral efficiency in compliance with the local regulations [61, 62]. The prevalent design of an RFID tag comprises of an antenna and an integrated chip, as detailed in Figure 1.3. An RFID tag is characterized by [63]:

i. Input impedance of the tag antenna: $Z_{\text{Ant}} = R_{\text{Ant}} + jX_{\text{Ant}}$

ii. Input impedance of the RFID chip in the absorb state: $Z_{\text{Abs}} = R_{\text{Abs}} + jX_{\text{Abs}}$

iii. Input impedance of the RFID chip in the reflect state: $Z_{\text{Ref}} = R_{\text{Ref}} + jX_{\text{Ref}}$.

Backscatter communication is achieved by interchanging the RFID chip impedance between the absorb and reflect state impedances, i.e., Z_{Abs} and Z_{Ref}, respectively. The choice of the reflect state or the absorb state depends upon the tag ID (or the data)

to be backscattered to the RFID reader. The reflection coefficients in the S_{Abs} and the S_{Ref} states of the tag are defined by [64],

$$\begin{aligned} \rho_{\text{Abs}} &= \frac{Z_{\text{Abs}} - Z_{\text{Ant}}^*}{Z_{\text{Abs}} + Z_{\text{Ant}}}, \\ \rho_{\text{Ref}} &= \frac{Z_{\text{Ref}} - Z_{\text{Ant}}^*}{Z_{\text{Ref}} + Z_{\text{Ant}}}, \end{aligned} \tag{1.3}$$

where ρ_{Ref} and ρ_{Abs} are the reflection coefficients for the reflect and absorb state of the RFID tag, respectively. Few important parameters for the further discussion are defined in the following [58, 63]:

i. T_{Chip}: is the minimum power required by an RFID tag chip to wake up its circuitry. The threshold value of T_{Chip} depends upon the frontend specifications of the RFID chip [65].

ii. ν: is the power transmission coefficient, given by [66, 67]

$$\nu = 1 - |\rho_{\text{Abs}}|^2 = \frac{4R_{\text{Abs}}R_{\text{Ant}}}{|Z_{\text{Abs}} + Z_{\text{Ant}}|^2}. \tag{1.4}$$

Basically, ν is an indicator of the amount of power absorption, in other words, the power supplied to the RFID chip. In an ideal ASK backscatter modulation scenario, the reflection coefficient in the absorbing state is $\rho_{\text{Abs}} = 0$ [68], implying $\nu_{\text{Abs}} = 1$. This is also a manifestation of $Z_{\text{Ant}} = Z_{\text{Abs}}^*$, i.e., complex conjugate match for maximum power transfer. In the reflect state, ideally $|\rho_{\text{Ref}}| = 0$, meaning that the signal is totally reflected at the chip input.

iii. P_{Chip}: is the power absorbed by the RFID tag chip. The RFID reader transmits RF power, P_{CW}, and data to the tag over the forward channel. P_{Chip} is defined as [69],

$$P_{\text{Chip}} = \nu P_{\text{Tag}} = \nu |S_{21}|^2 P_{\text{CW}}, \tag{1.5}$$

where P_{Tag} is the chip's input power and S_{21} is the channel transfer function (CTF) of the forward channel. For a workable backscatter communication system, P_{Chip} should be higher than the chip's sensitivity, T_{Chip} [70].

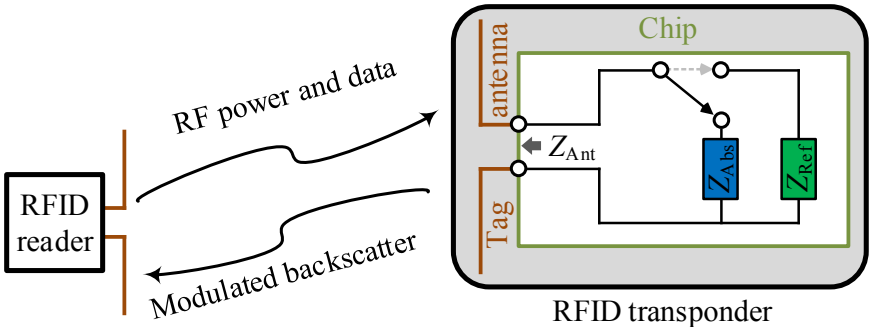

FIGURE 1.3: RFID Tag: Backscatter RFID setup consisting of an RFID reader and an RFID tag. The tag comprises of an antenna and a microchip. The complex input impedance of the antenna is Z_{Ant}. The complex input impedance of the tag's microchip switches between Z_{Abs} and Z_{Ref} as the tag interchanges between the absorb and reflect states, i.e., S_{Abs} and S_{Ref}, respectively [63].

iv. η: is the modulation efficiency . It compares the backscatter power reflected at the chip's input to the available power at the antenna's output, defined as [71]

$$\eta = \frac{2}{\pi^2}|\rho_{\text{Abs}} - \rho_{\text{Ref}}|^2 = \frac{2}{\pi^2}\frac{4R_{\text{Ant}}^2.|Z_{\text{Abs}} - Z_{\text{Ref}}|^2}{|Z_{\text{Abs}} + Z_{\text{Ant}}|^2.|Z_{\text{Ref}} + Z_{\text{Ant}}|^2}. \tag{1.6}$$

Equation 1.6 demonstrates that for an ideal ASK modulated backscatter system, the maximum achievable modulation efficiency is $\eta = 20\%$.

v. P_{RX}: is the power of the signal received at the RFID reader receiver, given by [68]

$$P_{\text{RX}} = |S_{12}|^2\eta P_{\text{Chip}} = |S_{12}|^2\eta|S_{21}|^2 P_{\text{CW}}, \tag{1.7}$$

where $|S_{21}|^2$ is the CTF of the reverse link.

During the forward and idle communication intervals, energy absorption by the RFID tag takes place from the provided electromagnetic field. Inherently, the tag input impedance is matched to the antenna impedance for maximum energy absorption. During the uplink cycles, the tag backscatters energy by interchanging its input impedance between the matched and unmatched state. This results in the reflection of a fraction of the received carrier wave [59]. The modulation function, i.e., $m(t) \in \{0, 1\}$, enables the tag to choose among the absorb ($m(t) = 0$) and reflect ($m(t) = 1$) states. Afterward, data is transmitted to the RFID reader receiver accordingly. The backscattered signal at the tag can be modeled as

$$x_{\text{Tag}}(t) = \sqrt{2}m(t)\sqrt{|\Delta\sigma|}|h^f|\sin(\omega_c t + \psi^f + \psi^{\Delta\sigma}), \tag{1.8}$$

where $|h^f|$ is the forward channel attenuation, ψ^f is the phase shift associated with the forward channel communication and $m(t)$ is the modulation function. The parameter $\psi^{\Delta\sigma}$ is the phase shift incorporated due to the tag modulation and $|\Delta\sigma|$ is the normalised radar cross section (RCS) area of the tag [72].

In the proposed model of [54] , all noise components are modeled additively at the reader receiver, without considering the noise components in the downlink channel. Therefore, the tag signal adds with the carrier leakage and the noise at the reader receiver. The passband signal can be written as:

$$\begin{aligned} x^{pb}(t) = \sqrt{2}|h^f||h^b|m(t)\sqrt{|\Delta\sigma|}\sin(\omega_c t + \psi^f + \psi^b + \psi^{\Delta\sigma}) \\ +\sqrt{2}|L|\sin(\omega_c t + \psi^{leak}) + n^{pb}(t), \end{aligned} \tag{1.9}$$

where $|h^b|$ is the backward (reverse) channel attenuation and ψ^f is the phase shift associated with the reverse channel communication. The complex valued carrier leakage signal can be rewritten as $L = |L|e^{j\psi^{leak}}$.

At the reader receiver, the received signal is downconverted to the baseband. The complex valued baseband signal can be formulated as:

$$x_{\mathrm{RX}}(t) = \sqrt{|\Delta\sigma|}h^f h^b m(t) + L + n(t), \tag{1.10}$$

where $h^f = |h^f|e^{j\psi^f}$ and $h^b = |h^b|e^{j\psi^b}$ are the complex valued forward and reverse channel coefficients, respectively, $|\Delta\sigma| = |\Delta\sigma|e^{j2\psi^{\Delta\sigma}}$ is the complex valued normalised differential radar cross section and $n(t)$ is the complex valued circularly symmetric additive white Gaussian noise (AWGN) with noise power spectral density N_o. Equation 1.10 can be reformulated as:

$$x_{\mathrm{RX}}(t) = hm(t) + L + n(t), \tag{1.11}$$

where $h = \sqrt{|\Delta\sigma|}h^f h^b$ is the combined channel coefficient of the dyadic channel, also incorporating the modulation attributes of the tag. Different stages of the inphase and quadrature (IQ) plane baseband constellation at the RFID reader receiver are shown in Figure 1.4.

In time intervals where the input impedance is well matched to the tag antenna impedance, the tag absorbs energy and equivalently the RFID reader establishes the tag

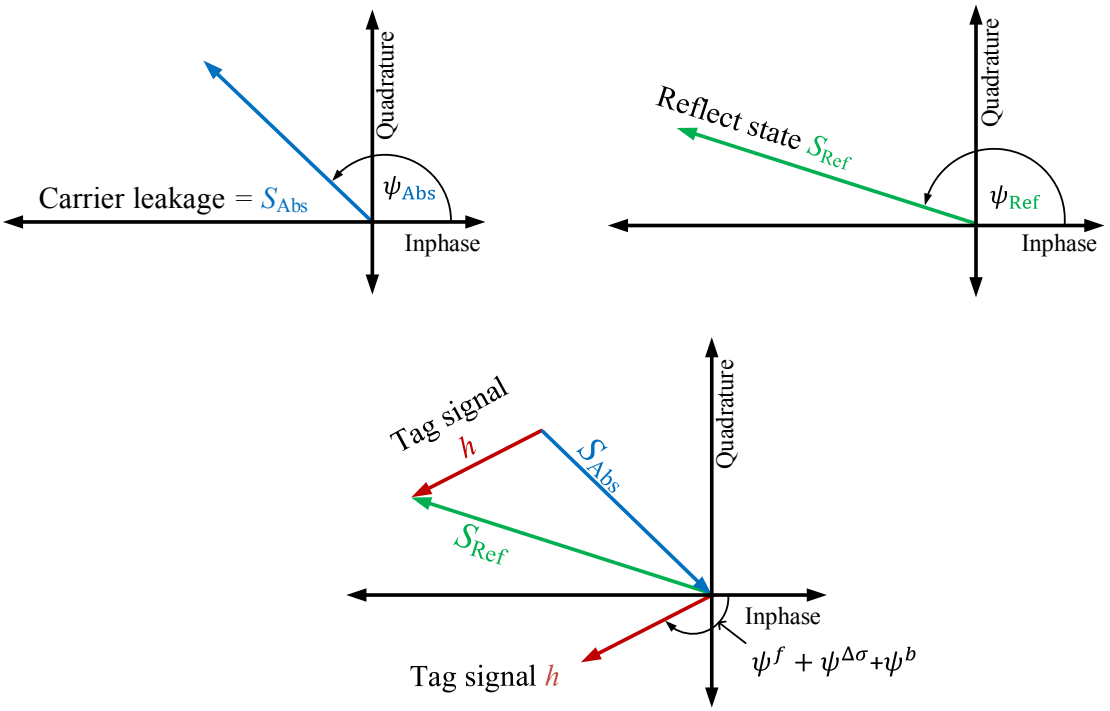

FIGURE 1.4: Baseband signal constellation: The carrier leakage vector is taken equal to the absorb-state vector. Together with reflect-state vector, the tag vector is found using the head-to-tail rule for vector additions [54].

in the absorb state, S_{Abs}. As $m(t) = 0$, the S_{Abs} vector is essentially equal to the leakage signal L. The unmatched input impedance of the tag enables backscatter communication to the reader receiver, and the reader encounters the reflect state, S_{Ref}. In order to get the tag signal (the channel coefficient h), we subtract the S_{Abs} vector from the S_{Ref} vector. Therefore the tag signal at the reader receiver is [54],

$$h = S_{\text{Ref}} - S_{\text{Abs}}. \tag{1.12}$$

1.3.2 SIMO RFID System

MIMO processing is a canonical method to improve wireless link capacity and reliability. In indoor environments, the layout structure and moving objects can cause reflection, refraction, diffraction, dead spots, and absorption of radio signals. Multipath phenomenon is pervasive, consequently jeopardizing the accuracy of an indoor positioning system [73]. In such multipath channels, MIMO techniques allows combating these phenomena by utilizing diversity, i.e., reliability against outage events [74]. By this, the positioning precision of an RFID system is improved. There are two further variants of MIMO, i.e., multiple-input single-output (MISO)and SIMO. In MISO technique, diversity is emplyed at the RFID transmitter side [75]. In this research, I needed to implement receiver diversity, i.e., SIMO technique. A basic SIMO backscatter RFID system is depicted in Figure 1.5. In SIMO configuration, we have multiple number of antennas at the reader receiver, i.e., N_R.

For a SIMO RFID system, the forward channel coefficient and tag backscatter modulation remains the same as in Equation 1.9 for the SISO case. The tag signal adds with the carrier leakage at the ith receive antenna [54]:

$$\begin{aligned} x_i^{pb}(t) = \sqrt{2}|h^f||h_i^b|m(t)\sqrt{|\Delta\sigma|}\sin(\omega_c t + \psi^f + \psi_i^b + \psi^{\Delta\sigma}) \\ +\sqrt{2}|L_i|\sin(\omega_c t + \psi_i^{leak}) + n_i^{pb}(t), \end{aligned} \tag{1.13}$$

where $|h_i^b|$ is the reverse channel attenuation from the tag to the ith receiver antenna and ψ_i^{leak} represents the phase shift experienced by the radio signal in traveling from the tag to the ith receive antenna. In similar vain, $|L_i|$ and ψ_i^{leak} are the magnitude and phase shift of the carrier leakage at the ith receive antenna. The complex baseband

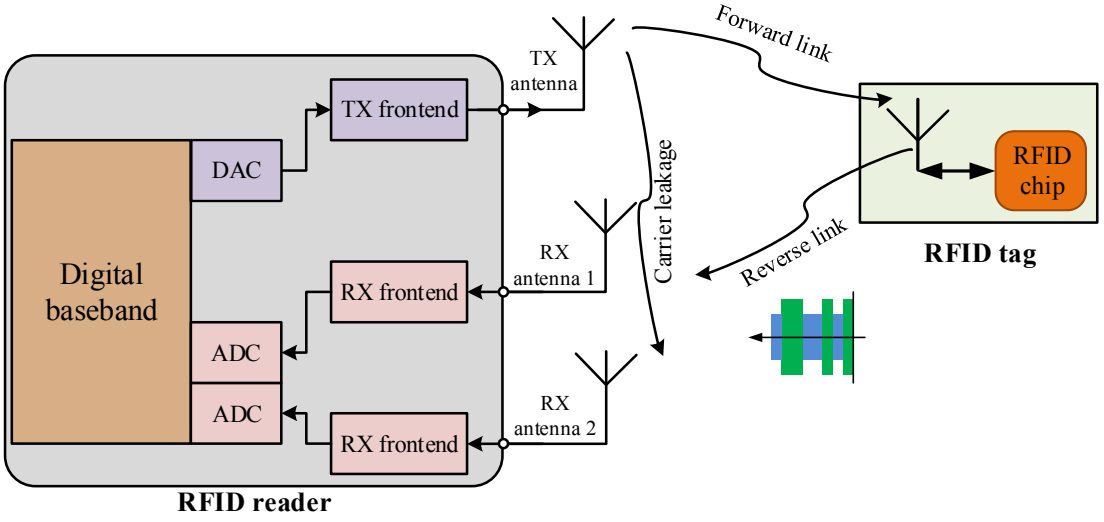

FIGURE 1.5: Basic Structure of a SIMO RFID System in a bistatic configuration: The RFID reader consists of one transmit and two receiver antennas. Information is processed in the digital baseband subsection, then passed on to digital-to-analogue converter (DAC) block. Transmitter frontend sends the data from the RFID reader transmitter to the tag in the form of a continuous analog waveform (CW). The RFID tag gets requisite energy to power-up its circuitry and starts backscatter communication via ASK to the two reader receiver antennas, i.e.,RX antenna 1 and RX antenna 2. The analog wave forms reaches the analog-to-digital (ADC) converters via the RX frontend.

The data send by the tag is then processed in the digital baseband subsection.

signal at the ith receive antenna can be modeled as

$$x_{\mathrm{RX}_i}(t) = \sqrt{|\Delta\sigma|} h^f h_i^b m(t) + L_i + n_i(t). \tag{1.14}$$

In this, [54] defines $h_i^b = |h_i^b| e^{j\psi_i^b}$ as the complex valued reverse channel coefficient, $L_i = |L_i| e^{j\psi_i^{leak}}$ denotes the carrier leakage and $n_i(t)$ is the complex valued circularly symmetric AWGN with noise power spectral density N_o. Combining the channel coefficients, as in Equation 1.11:

$$x_{\mathrm{RX}_i}(t) = h_i m(t) + L_i + n_i(t), \tag{1.15}$$

where $h_i = \sqrt{|\Delta\sigma|} h^f h_i^b$ is the combined channel coefficient of the dyadic channel from the transmitter to the tag and back to the ith receive antenna. As previously, the modulation attributes of the tag are also incorporated via the term $\sqrt{|\Delta\sigma|}$. For the case of space domain phase difference of arrival (SD–PDoA), I have employed a receiver antenna of a 2 element uniform linear array (ULA), i.e., $i = 1, 2$. Therefore, the tag signal at each of the two antennas of the SIMO reader receiver is,

$$h_i = S_{\mathrm{Ref}_i} - S_{\mathrm{Abs}_i}. \tag{1.16}$$

The associated phases of the tag signals h_i, $i = 1, 2$ will be utilized in the system analyzer of section 3.2 for the direction of arrival (DoA) estimation (as elaborated in section 1.5.1) and in the system analyzer of section 3.3 for the range estimation (as elaborated in section 1.5.2).

In this model, only the received signal from a tag bears the information about the location of the tag. The tag signal phases (ψ_1 and ψ_2) for both RX1 and RX2 in the IQ plane can be written, respectively as,

$$\psi_1 = \psi^f + \psi^{\Delta\sigma} + \psi_1^b, \tag{1.17}$$

$$\psi_2 = \psi^f + \psi^{\Delta\sigma} + \psi_2^b. \tag{1.18}$$

We can assume that both ψ^f and $\psi^{\Delta\sigma}$ have equal influence on the two receiver antennas in our SIMO RFID reader. As a result, a phase difference of $\Delta\psi = (\psi_2 - \psi_1)$ in the IQ constellation of both receiver paths incorporates the information about the tag location.

1.4 Fundamentals of Wireless Localization

Radio technology has been at the forefront of localization systems since the discovery of radar technology. As of present, on of the most successful and prevalent radio-based localization system is the global positioning system (GPS). The GPS technology relies on an unobstructed line of sight (LoS) to the GPS satellites for providing accurate location information anywhere on earth. However, the biggest drawback of GPS based navigational systems is that they can't be used within indoor environments. For indoor environments, we have to resort to other technologies such as wireless local area networks (WLANs), RFID, Bluetooth, ZigBee, infrared, cellular mobile communication (GSM, UMTS) etc. [76–78].

In majority of the indoor localization based on wireless networks/sensors, there is an assumption that the signal is predominantly traveling along an LoS path. But when the object to be localised is not in the LoS path, multipath phenomenon makes it it difficult to distinguish which radio signals are coming directly from the object and which are from the scatterers. As a consequence, the accuracy of wireless networks/sensors based indoor positioning is compromised.

The indoor localization schemes based on wireless technologies can be grouped into three broad categories [79, 80]:

1. Fingerprinting/Mapping: In deployment of radio infrastructure, geometry of a site plays an important role in the subsequent performance of radio wave propagation. Power delay profile (PDP) metric helps in characterizing a wireless channel. The mapping approach considers characteristics such as PDPs (as a function of the measured location). This basically gives a one-to-one mapping of the PDP to a particular location inside the measured space [81, 82]. This approach is particularly useful in wideband or ultra-wideband (UWB) systems. UWB systems offer leverage of distinguishing between the LoS and non-line of sight (NLoS) components coming from the object to be localized. The inherent nature of mapping is such that the system localization performance gets better by rich multipath propagation. However, the prevalent RFID systems are intrinsically narrowband, therefore this approach is not applicable for localizing RFID tagged objects [83].

2. Geometric: As the title implies, this approach depends on geometric-based parameters such as DoA, received signal strength (RSS), range, or time of arrival

(ToA) of the received radio signal at the wireless sensors. After obtaining the location-based information via RSS, DoA, range and/or ToA, different algorithms are employed to estimate the location of the object.

DoA gives the direction of arrival of the received radio signal by employing an antenna array. In severe multipath scenarios, banking upon only on DoA estimation results in low localization accuracy. In ToA based localization systems, the time of arrival of the first detected peak of the received radio signal is used to estimate the distance between the transmitter and receiver [76]. Both DoA and ToA are used in traditional radar and GPS based localization systems. The RSS is a single metric and can be measured by most of the wireless devices. The RSS value decays linearly with the log-distance between the wireless transmitter and receiver, the observed RSS value is mapped to the distance from the transmitter. RSS value can be calculated by [84],

$$\mathrm{RSS}_d = 10\log_{10}P_\mathrm{r} = 10\log_{10}P_\mathrm{t} - 10a\log_{10}d + X, \tag{1.19}$$

where a is the distance-power gradient., X is a log-normally distributed stochastic variable (shadow fading), P_r is the received power, P_t is the transmitted power. The performance of RSS based indoor localization systems is not that accurate, albeit the method itself is very simple. Due to shadow fading and multipath fading, the instantaneous value of RSS in indoor environments varies over time, even at a fixed location [85]. For this reason, in traditional localization systems RSS based methods are not utilized.

3. Proximity: In this category, the area (in which an object is to be localized) is filled by a large number of wireless sensors. When the to-be localized object enters in the sensing range of a sensor, the location of the object is taken as of the sensor. If multiple sensors detect the object, then the one with the strongest signal is estimated to be the location of the object. A typical example could be of localizing a mobile in a cellular network. It is accomplished through the position of the base station to which the mobile is device is connected to. In this case the localization accuracy is on the order of the size of the cellular network's cell size.

1.5 RFID Localization

Object inventorying was the initial motivation behind inventing the RFID technology [86–88]. Over the past decade, the research paradigm has been shifted towards RFID based localization. Localization principle using the RFID technology is quite similar to the radar ranging problem. However, RFID based systems differ in some aspects from the radar ranging problem. In radar systems the distance between a transmitter and a receiver is not that short, whereas in RFID systems it is on the order of less than 10 m. As a consequence, the overall signal delay is on the order of a few tens of nanoseconds. As majority of RFID systems are narrowband, measuring the time of arrival is quite difficult. An alternative can be to utilize the phase information of the received radio signals for the localization purpose. [89] provides a detailed overview of different RFID based localization techniques and trends.

Contemporary research utilizing the phase difference of arrival (PDoA) technique has shown satisfactory results [90, 91]. As outlined in [90], the PDoA based techniques can be used in three different manners to determine the location of an RFID tag. They are namely:

1. Time domain phase difference of arrival (TD–PDoA)
2. Frequency domain phase difference of arrival (FD–PDoA)
3. Space domain phase difference of arrival (SD–PDoA)

As in this thesis, I have based the RFID system analyzer on the techniques of SD–PDoA and FD–PDoA, therefore these two are explained a bit in the following sections.

1.5.1 SD–PDoA Based DoA Estimation

PDoA technique estimates the DoA by measuring the different phase delays exhibited by radio signals (operating at the same carrier frequency) at several reader receiver antennas [90]. This is in essence equivalent to the beamforming technique. Figure 1.6 depicts a simple geometrical arrangement for the implementation of PDoA based DoA estimation. The arrangement in Figure 1.6 is of a bistatic antenna configuration. The reader receiver antennas are forming a ULA of two antennas with spacing a. The forward channel coefficient from the TX to the RFID tag is h^f and the reverse channel from the

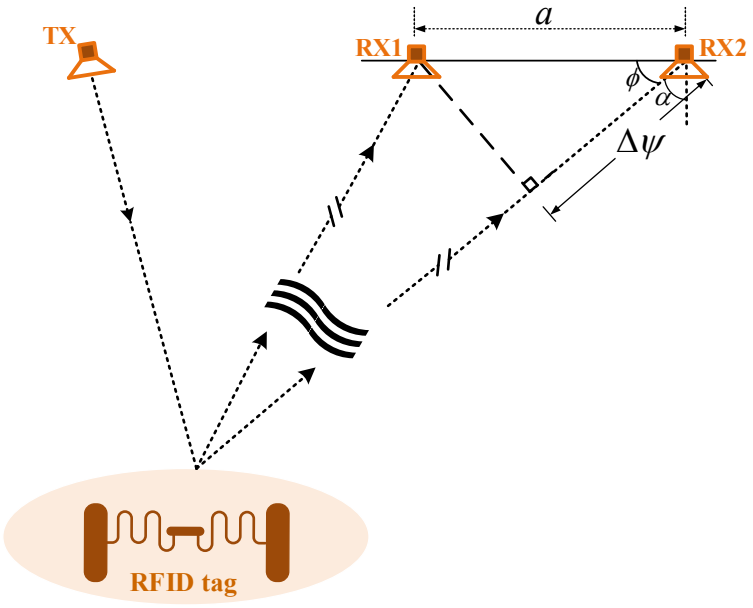

FIGURE 1.6: Geometrical depiction of the SD–PDoA technique. Both of RX1 and RX2 are considered to be in the far-field of the RFID tag antenna. The angle ϕ is the DoA and subtracting it from the perpendicular, we get the incident angle α.

tag to the ith receiver antenna is h_i^b. As shown in [92, 93] in a ULA of N elements, if the distance D between a tag and a reader receiver is much larger than the array size, i.e., $D \gg (N-1)a$, the phase difference between two neighboring elements of the ULA is

$$\Delta\psi = \psi_2 - \psi_1 = ka\cos(\phi). \tag{1.20}$$

Here $k = 2\pi/\lambda$ is the wave number, λ denotes the wavelength of the signal, ϕ is the DoA, ψ_1 is the phase difference measured at RX1 of the ULA in Figure 1.6 and ψ_2 is measured at RX2. Therefore, from the above equation, the DoA is estimated as [94]

$$\phi = \arccos(\Delta\psi/ka). \tag{1.21}$$

1.5.2 FD–PDoA Based Range Estimation

Range of an RFID tag is an important factor to be estimated for accurate localization. It can be achieved by estimating the signal attenuation due to free space loss. But the RSS localization is compromised due to strong multipath signals. The situation can be alleviated by deploying reference tags [95] but it accentuates the overall budget constraints. Presently, the ranging of ISO 18000–6C [40] compliant UHF RFID tags is constrained by the governing regulations of the UHF band spectral usage [70]. Moving to the UWB range [32] is also solution but the overall setup costs increases.

The FD–PDoA is basically a ranging method. Transmitted electromagnetic waveforms of different carrier frequencies experience different phase delays while traversing the same distance in a wireless channel, as depicted in Figure 1.7. This phase difference $(\psi_2 - \psi_1)$ of received waveforms is exploited for the estimation of range between an RFID tag and an RFID reader [96]. In this scheme we have signals operating at two different carrier frequencies, i.e., f_1 and f_2. The underlining assumption is that $f_2 > f_1$. The transmitted waveform $x(t)$ at the RFID reader transmitter is expressed in terms of phase as,

$$x(t) = \exp(j2\pi f_1 t + j2\pi f_2 t). \tag{1.22}$$

The RFID reader transmits two continuous wave (CW) signals towards the tag. These two waveforms are then sent back by the RFID tag to the RFID reader receiver, using backscatter modulation technique. These two waveforms cover almost the same distance, but their phase delays are proportional to their respective carrier frequencies.

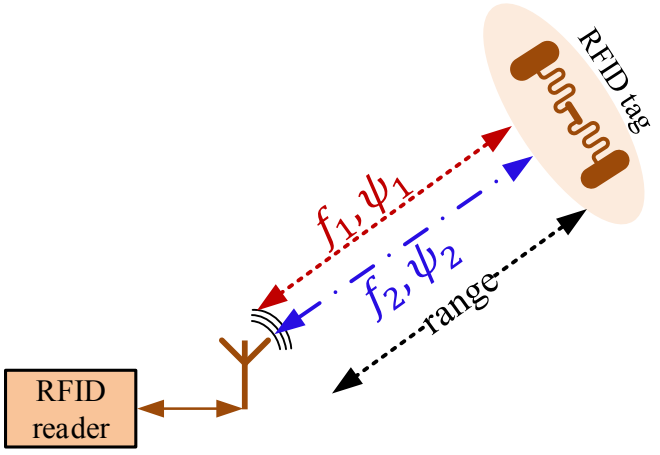

FIGURE 1.7: Dual frequency FD–PDoA ranging technique for a monostatic RFID reader setup [90].

We assume R as the distance between the RFID reader and the tag. Assuming a combined (over both the forward and backward links) channel fading of h and $\delta(t)$ as the backscatter modulation signal at the tag. $\delta(t)$ is inherently a complex signal, therefore accounting for both the phase and amplitude modulations. Both of the transmitted CWs operating at f_1 and f_2 will be downconverted coherently at the RFID reader receiver, employing two separate mixers (operating at the two carrier frequencies f_1 and f_2) and later demodulated, yielding two separate signals y_1 and y_2. The detailed schematic of a bistatic antenna configuration is shown in Figure 1.8. The output signal at the RFID reader receiver will be like

$$y_i(t) = h\,\delta(t)\,\exp(-j\psi), \quad i = 1, 2. \tag{1.23}$$

For a monostatic antenna configuration, the distance from the RFID transmitter to the RFID tag and backwards is $R + R = 2R$. For this, we may establish the relationship between distance R and a generic phase θ using the basic mathematical relationship of

$$\theta = \omega t = 2\pi f \frac{2R}{c} = \frac{4\pi}{c} f R, \tag{1.24}$$

from which the range can be derived as

$$R = \frac{c}{4\pi} \frac{\theta}{f}, \tag{1.25}$$

where c is the speed of light and θ represents the phase, assuming the initial transmitted

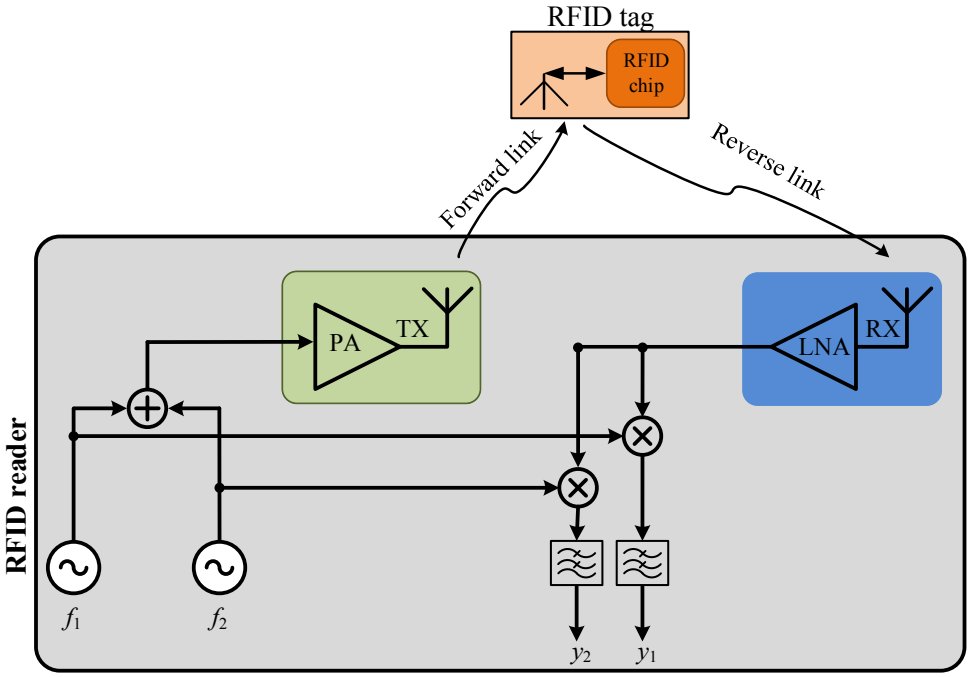

FIGURE 1.8: Schematic diagram of the concept of dualFor the case of a bistatic TX frequency RFID system [80], where PA is the power amplifier before the transmitter antenna TX and LNA is the low noise amplifier after the receiver antenna RX.

phase at time t is $\theta_1 = 0$. At time $t + k$, the tag backscatters the signal back to the RFID reader receiver with a phase of θ_2. The total phase variation over the backscatter communication channel (TX–tag –RX) is

$$\theta = \theta_2 - \theta_1 = \theta_2. \tag{1.26}$$

This overall phase θ is constituted by

$$\theta = \theta_{\mathrm{d}} + \theta_{\mathrm{TX}} + \theta_{\mathrm{RX}} + \theta_{\mathrm{Tag}}, \tag{1.27}$$

where θ_{d} is the phase delay due to propagation over a backscatter channel. θ_{TX}, θ_{RX} and θ_{Tag} are the phase irregularities introduced due to the transmitter circuits, receiver circuits and the tag's reflection characteristics, respectively. All of the last three phases in equation 1.27 incorporate additional phase rotation, thus leading to inaccurate range estimation via equation 1.25. These phases will be calibrated out [97], as explained in section 3.3.1. Referring back to equation 1.25, we have

$$\psi_1 = \frac{4\pi f_1 R}{c}, \tag{1.28}$$

$$\psi_2 = \frac{4\pi f_2 R}{c}, \tag{1.29}$$

where we have taken ψ_1 and ψ_2 as the phase variations associated with the carrier frequencies f_1 and f_2, respectively. By taking the difference of phases observed at two different frequencies, we can estimate the range between the RFID reader and the tag by [98],

$$\Delta\psi_{12} = \frac{4\pi(\Delta f_{12})R}{c} \Longleftrightarrow R = \frac{c(\Delta\psi_{12})}{4\pi(\Delta f_{12})}, \tag{1.30}$$

where $\Delta\psi_{12} = \psi_2 - \psi_1$ is the observed phase difference and $\Delta f_{12} = f_2 - f_1$ is the frequency separation between the two carrier frequencies. As the phase difference $\Delta\psi$ is bounded by $(\psi_2 - \psi_1) \leq 2\pi$, the corresponding maximum unambiguous range is [80]

$$R_{\max} = \frac{c}{2\Delta f_{12}}. \tag{1.31}$$

The significance of $R_{\max}$ is that when the actual distance exceeds $R_{\max}$, we encounter range ambiguity. In this case the phase difference can be expressed as

$$\Psi_{12} = \Delta\psi_{12} + 2m\pi, \tag{1.32}$$

where $m \geq 0$ is an unknown integer. Incorporating this range ambiguity in equation 1.30, we have

$$\hat{R} = \frac{c(\Delta\psi_{12})}{4\pi(\Delta f_{12})} + \frac{cm}{2(\Delta f_{12})}. \tag{1.33}$$

The above equation implies that for a given phase difference, we can get infinite range estimates with a separation of $R_{\max}$ between the two adjacent range estimates. In this case $\hat{R}$ can also be found as (R mod $R_{\max}$).

The range estimation formula derived in equation 1.30 is for a monostatic antenna configuration. In that case, the distance from the TX to tag (R_1) and back to the RX (R_2) is the same ($R_1 + R_2 = R + R = 2R$). For the case of a bistatic TX–RX antenna configuration, $R_1 \neq R_2$. Therefore, equation 1.30 has to be remodeled, hence bifurcating the complete backscatter phase variation $\Delta\psi_{12}$ into $\Delta\psi_{\text{TX–Tag}}$ and $\Delta\psi_{\text{Tag–RX}}$. Then assuming a distance R_1 from the RFID TX to the tag and R_2 the distance from the tag to the RFID reader receiver, by remodeling equation 1.30 we get

$$R_1 = \frac{c(\Delta\psi_{\text{TX–Tag}})}{2\pi(\Delta f_{12})}, R_2 = \frac{c(\Delta\psi_{\text{Tag–RX}})}{2\pi(\Delta f_{12})}. \tag{1.34}$$

Therefore, the complete range from the TX–Tag–RX can be calculated as

$$\overbrace{R_1 + R_2}^{2R} = \frac{c}{2\pi}\left(\frac{\Delta\psi_{\mathrm{TX-Tag}} + \Delta\psi_{\mathrm{Tag-RX}}}{\Delta f_{12}}\right). \tag{1.35}$$

Equation 1.35 is valid for both of the backscatter links, i.e., TX–Tag–RX1 and TX–Tag–RX2.

1.6 Contribution and Thesis Outline

In all of the aforementioned simulation platforms/frameworks, none of them incorporate real channel measurements in a system simulator which models true UHF RF signals. The framework of this research is to bridge the gaps between system and hardware–level simulation, based on Matlab®/Simulink® [99, 100]. I have combined real channel measurements with a system analyzer designed using the SimRF™ [101] environment in Simulink®. The RF parts of the system analyzer are built using the SimRF™ toolbox[2] , which runs on top of the RF Toolbox™ [103], providing a component library and simulation engine for the design of RF systems, within the Simulink® environment. Interfaces to Simulink (from SimRF™) enable signal generation and analysis features found both in the Communications System Toolbox™ [104] and the DSP System Toolbox™ [105]. It supports circuit envelope and harmonic balance simulation, multifrequency analysis, and multi–port component models. Rest of the system blocks (non–RF) are built using the Communications System Toolbox™ and the DSP System Toolbox™ in Simulink®. This is the first of its kind system analyzer built in the SimRF™ environment, employing true RF signal generation. Such a system level emulation platform provides flexibility in order to emulate various hardware aspect.

The system analyzer is modeled for the application of narrowband UHF RFID tag localization using the PDoA techniques [90]. Basically, I have developed two different topologies in order to estimate the DoA and the range of the RFID tag, based on the SD–PDoA and the FD–PDoA techniques, respectively. As expected by previous research, using this channel measurement setup, the system analyzer is able to provide coarse–grained localization results of a prospective hardware setup in such a severe multipath environment or in fact, in any other environment. Although, UWB RFID systems

[2]In the R2017a release of Matlab®/Simulink®, the SimRF™ product has been renamed as the RF Blockset™ [102].

give better localization performance [106–108], but in applications where pinpoint localization is not required, narrowband systems in the UHF band employing receive antenna diversity have been found to perform adequately [109, 110]. Moreover, the low cost of UHF RFID systems also favors their adaptation.

In the following, I will describe the contents of individual chapters of this thesis briefly.

Chapter 2 provides the details of the channel measurement campaign, the antenna setup, etc. The wireless channel is the most crucial factor in designing any wireless communication system. I will present the statistical analysis of the channel measurement campaign conducted at AVL, Graz. Parameters like PDP, root mean square (RMS) delay spread and power ratio (of the line of sight to the multipath components) are calculated. This analysis is always crucial for justifying the behavior of localization systems in a wireless channel.

Chapter 3 presents the design of a real channel measurement based system analyzer. The motivation has been to localize a tagged object in a severe multipath environment. The RF blocks of the analyzer are designed in the SimRF™ toolbox of Simulink® [101], hence emulating true RFID signals in the UHF range. The standout feature of the analyzer is its flexibility. Different parameters can be tweaked as per the application. In my application, the most important feature of the analyzer is the ability to incorporate the channel measurements in order to estimate the DoA and range of an RFID tag. I have designed two different topologies of system analyzer based on the concepts of SD–PDoA and FD–PDoA, for estimating the DoA and range of an RFID tag, respectively. By this, a coarse–grained localization of an RFID tagged object can be estimated inside a severe multipath indoor environment. Moreover, in future extensions, more system nonlinearities can be incorporated in the RF sections of the analyzer, hence emulating the real hardware setup more precisely. A test case can be to implement the nonlinear behavior of an RFID chip impedance as a function of the incident power [111]. The system analyzer's performance has been verified by using channel data of a measurement campaign inside an anechoic chamber.

Chapter 4 The range estimation system analyzer presented in chapter 3 is further exploited by investigating the theoretical concept of multifrequency PDoA (MF–PDoA). For this, another channel measurement campaign was conducted in an indoor laboratory environment, i.e., a multipath environment. Both the two cases of equal frequency

based MF–PDoA and the Chinese remainder theorem (CRT) based unequal frequency separation MF-PDoA techniques have been tested using the real channel measurements. The range estimation results of the CRT based MF-PDoA based technique has shown to enhance the accuracy of an RFID based localization system, as predicted by theory.

Chapter 2

Multipath UHF RFID Channel

The stringent constraint in any wireless communication system is the wireless channel itself. Localization using UHF RFID technology is quite intricate, mainly due to a wireless channel [112–114]. The development of wireless communication systems requires extensive field tests to estimate its performance. Radio system development and later deployment requires statistical analysis of the propagation channel characteristics as well [62, 115]. Radio wave propagation measurements [116, 117] offer a method to characterize different wireless environments. Characterization of mobile radio channels can be formalized from the general description of linear time-variant channels [118].

In this chapter, I will describe the measurement campaign conducted at AVL Graz, inside a severe multipath channel, i.e., in an engine test bed facility. The measurement campaign was conducted to obtain real channel measurement data which will be later utilized in the measurement based system analyzer. Statistical analysis of the channel measurements is also presented in this chapter [119] which will be helpful in gaining an insight for the performance analysis of the system analyzer in chapter 3. The indoor radio channel in an industrial environment exhibits a severe multipath propagation scenario due to the prevalent metallic structures. To achieve better localization in this multipath environment, a SIMO antenna setup was employed, as shown in Figure 1.5.

2.1 RFID Channel Measurement Setup

As mentioned in section 1.2, under the auspices of the *SeCoS* project there was a task to design a system analyzer capable of achieving coarse-grained localization of RFID tags

inside an engine test bed facility at AVL, Graz. For this sake, the starting point was to characterize a severe multipath industrial channel. Therefore, a channel measurement campaign was conducted in a realistic and reproducible indoor multipath environment, i.e., in an engine test bed facility at AVL, in Graz. The feasibility of such a system was carried out in [120]. Channel transfer functions (CTFs) were measured using the vector network analyzer (VNA) ZVA 67 from Rohde & Schwarz at several LoS and NLoS tag antenna positions. The CTFs were measured versus frequency at 30 tag antenna positions within the room. Floor plan of the tag antenna positions within room no. 326 is shown in Figure 2.1 and the investigated reader and tag antenna positions are listed in Table 2.1. The measurement environment includes a large metallic engine test bench in the middle of the room, some metallic obstacles like high rise tables, metallic tools and some boxes, as shown in Figure 2.4. Position numbers 19–30 are the tag positions where we do not have an LoS channel between the tag and reader receivers. The tag antenna track from position 1 to 18 provides a strong LoS propagation channel between the reader and tag antennas. We have tested our system simulator for these eighteen positions. At each antenna position, the CTF measurement versus frequency is repeated 20 times [121].

The measurements were conducted in a frequency range from 700 MHz to 1200 MHz. As explained, a SIMO antenna configuration was employed to combat the multipath phenomenon. Therefore, having one transmitter (TX) antenna and two reader receiver antennas (RX1 and RX2). The antenna setup is depicted in Figure 2.2. The spacing a between the center of the reader receiver antennas, i.e., RX1 and RX2, is kept about 30 cm. All four of the TX, RX1, RX2 and the tag antennas are connected to the VNA using 50 Ω coaxial cables. The channel measurements were performed with two different antennas used as the RFID tag antenna, as shown in Figure 2.3. Firstly, in the "Reference" scenario a commercially available patch antenna was used as the RFID tag antenna. Secondly, in the "Tag" scenario a custom-built patch antenna was used as the RFID tag antenna, which has a typically low gain as state of the art tag antennas have. The matching of the custom-built tag antenna was found to be -13 dB at 890 MHz. The tag antenna was surmounted on a mobile fixture, so that it can be positioned on LoS and NLoS positions inside the engine test bed facility. The transmitter (TX) and reader antennas (RX1 and RX2) are Motorola AN480 [122] patch antennas.

The VNA is connected via the local area network (LAN) to a personal computer

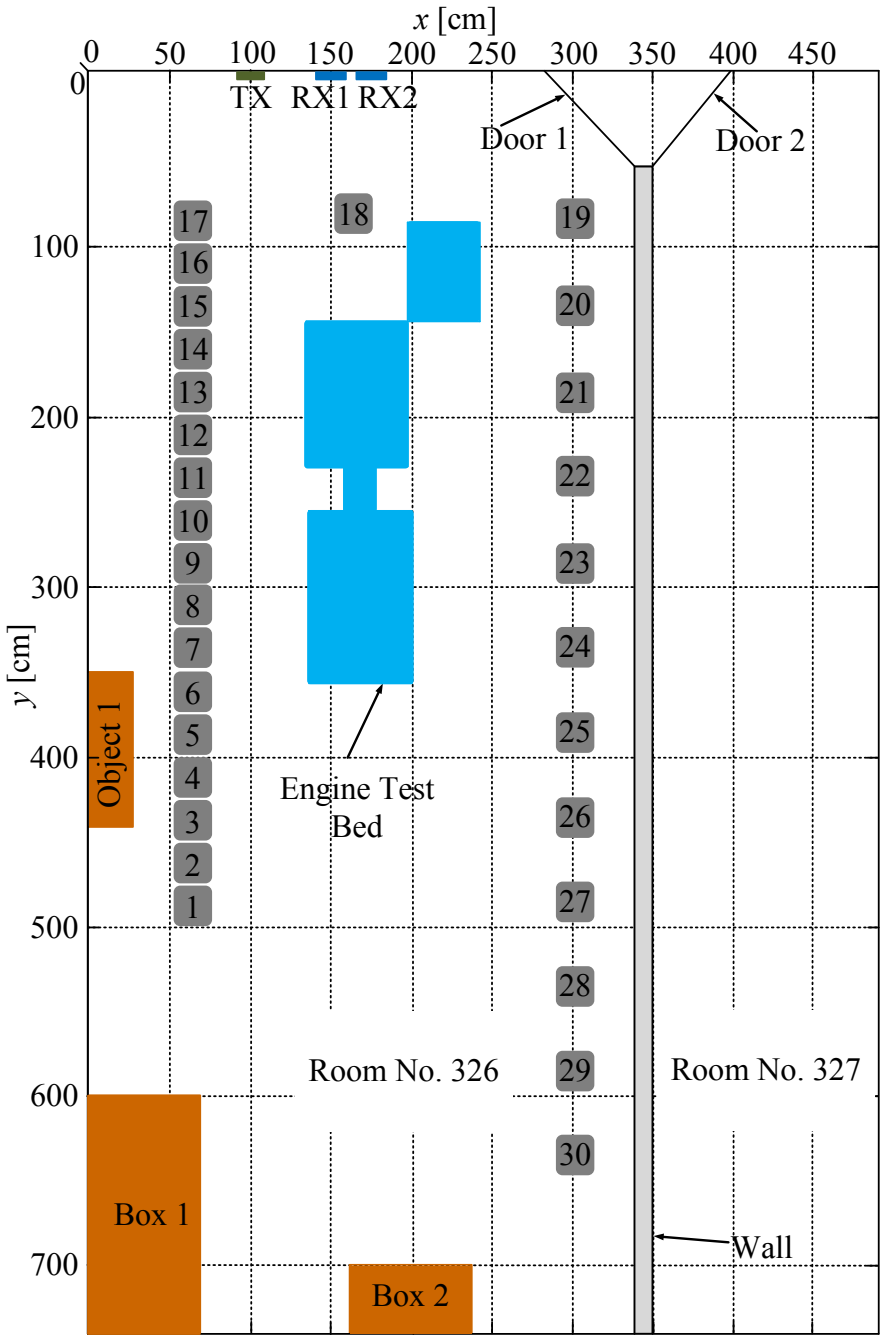

FIGURE 2.1: Channel measurement campaign: Numbered from one to eighteen. The numbered 19 till 30 are the NLoS positions and 31 till 34 are the four interfering tag positions. There were some boxes and objects in the room, depicted with brown color. The engine test bench can also be seen in the middle of the figure.

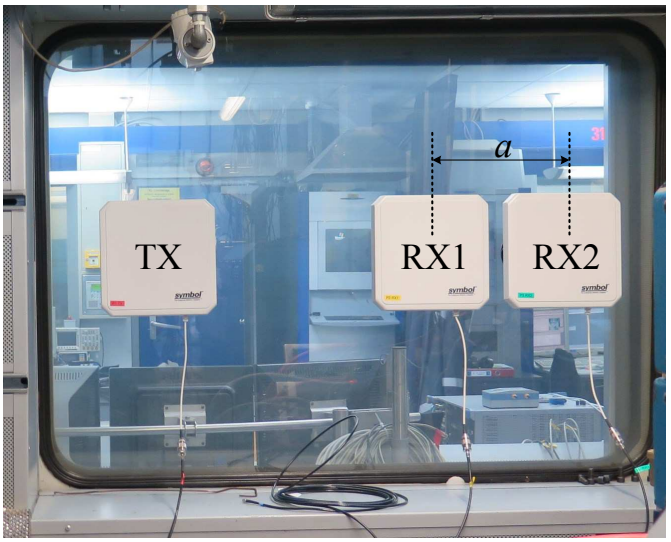

FIGURE 2.2: Antenna setup in the AVL measurement campaign. The antennas were attached to the glass window of the engine test bed room. The measurement scripts were run on a PC, behind the glass window.

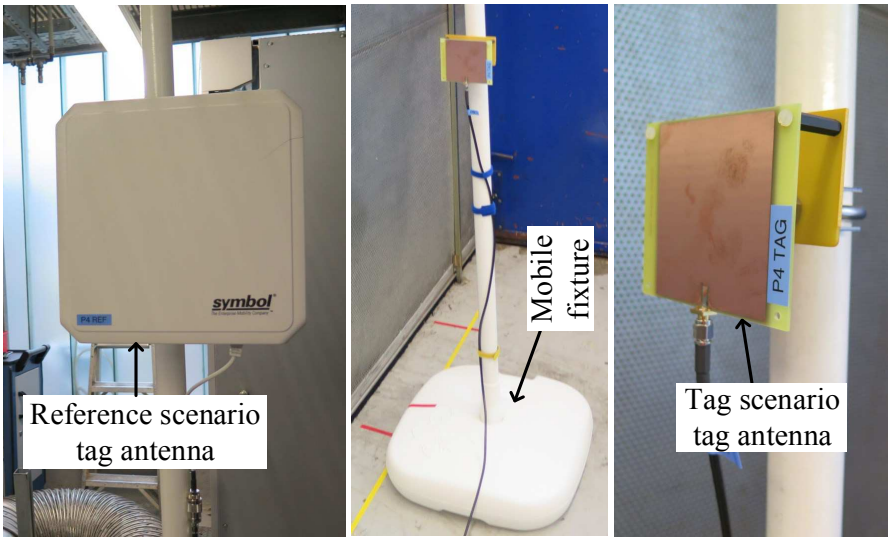

FIGURE 2.3: Antennas used as RFID tag in the Reference and the Tag sceanrio.

TABLE 2.1: Detailed tag antenna positions: Reader antennas (TX, RX1, RX2) and tag antenna positions in Cartesian coordinates

Position Number	***x*** **(meters)**	***y*** **(meters)**	**Position Number**	***x*** **(meters)**	***y*** **(meters)**
1	0.63	4.85	16	0.63	1.1
2	0.63	4.6	17	0.63	0.85
3	0.63	4.35	18	1.65	0.8
4	0.63	4.1	19	0.85	3
5	0.63	3.85	20	1.35	3
6	0.63	3.6	21	1.85	3
7	0.63	3.35	22	2.35	3
8	0.63	3.1	23	2.85	3
9	0.63	2.85	24	3.35	3
10	0.63	2.6	25	3.85	3
11	0.63	2.35	26	4.35	3
12	0.63	2.1	27	4.85	3
13	0.63	1.85	28	5.35	3
14	0.63	1.6	29	5.85	3
15	0.63	1.35	30	6.35	3

(PC) that executes the measurement script. The reader antennas are positioned at the entrance of the engine test bed and are at the same height of 1.5 m as the tag antenna, as shown in Figure 2.2. The measurement reference plane is at the input of the antennas. The operating frequency used is 890 MHz. The VNA generates continuous sinusoidal waves (without modulation) for the channel measurements [123].

2.2 Statistical Analysis

The complex CTFs, i.e., the scattering (S-) parameters were acquired using the VNA as per the port configuration listed in Table 2.2. S_{41}, S_{24} and S_{34} are the CTFs, $H(f)$ used for the analysis. Where S_{41} corresponds to the channel from the transmitter antenna (TX) to the tag antenna, S_{24} and S_{34} correspond to the channels from the tag to the reader receiver antenna one (RX1) and the reader receiver antenna two (RX2), respectively. The frequency of the transmitted signal was swept from 700 MHz to 1200 MHz

TABLE 2.2: VNA port configuration

Antenna	VNA port number	Antenna	VNA port number
TX	1	RX1	2
Tag	4	RX2	3

FIGURE 2.4: Engine test bed environment. Both of the LoS (green tape) and the NLoS (yellow tape) trails are shown in the figure, with red tapes depicting the position numbers.

corresponding a resolution of

$$\Delta\tau = \frac{1}{(1200\,\text{MHz} - 700\,\text{MHz})} \approx 2\,\text{ns}, \tag{2.1}$$

in the delay domain. The wireless channel was probed at 251 points in the measured frequency range, implying a separation of

$$\Delta f = \frac{(1200\,\text{MHz} - 700\,\text{MHz})}{251} \approx 2\,\text{MHz}, \tag{2.2}$$

between two adjacent frequency points, giving a maximum resolvable time delay of [116, 124]

$$\frac{1}{\Delta f} = 502\,\text{ns}. \tag{2.3}$$

2.2.1 Power Delay Profiles

In radio planning, radio wave propagation is governed by the geometry of the site, especially the size, density, structure of buildings, indoor floor layout, furnishings' locations etc. The power delay profile (PDP) depicts the average of these effects [125]. It indicates the received signal power versus time delay. A detailed overview of this topic is provided in Chapter 2 of [32]. Basic power delay profiles are shown in Figure 2.5. In a PDP, the first arriving component corresponds to the LoS communication path between the transmitter and the receiver. All the remaining components in the the PDP are depicting the NLoS communication between the transmitter and the receiver. One noticeable feature of a PDP is the exponential decay, although it is not the case for all of the wireless channels. Another feature of PDP is the clustering of the multipath components (MPC), constituting the NLoS part of the PDP. Different clusters correspond to different scatterers in the wireless channel [115].

In this work, the measured CTFs S_{41}, S_{24}, and S_{34} were converted to the delay domain using an inverse Fourier transform (IDFT). Before applying IDFT, the CTFs were multiplied by a Hanning window $hann(f)$ [123, 126] to suppress aliasing. The effect of this spatial averaging is a reduction in the noise peaks, which are assumed to be uncorrelated between measurements and uncorrelated with wanted signals. The degree of noise smoothing is related to N. For additive white Gaussian noise with zero mean and σ_n as the standard deviation, the averaged noise standard deviation is reduced to

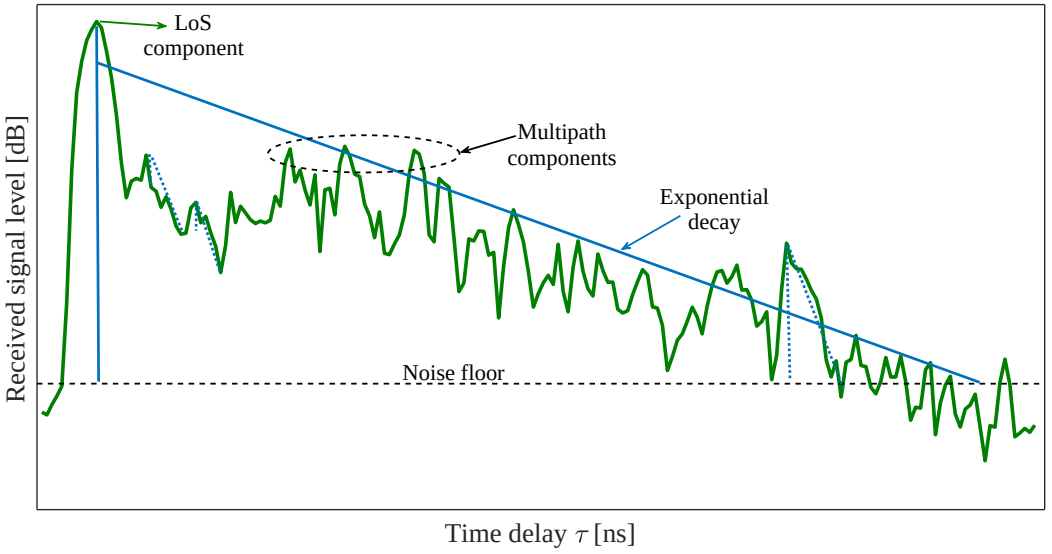

(a) A typical power delay profile with a clear LoS component.

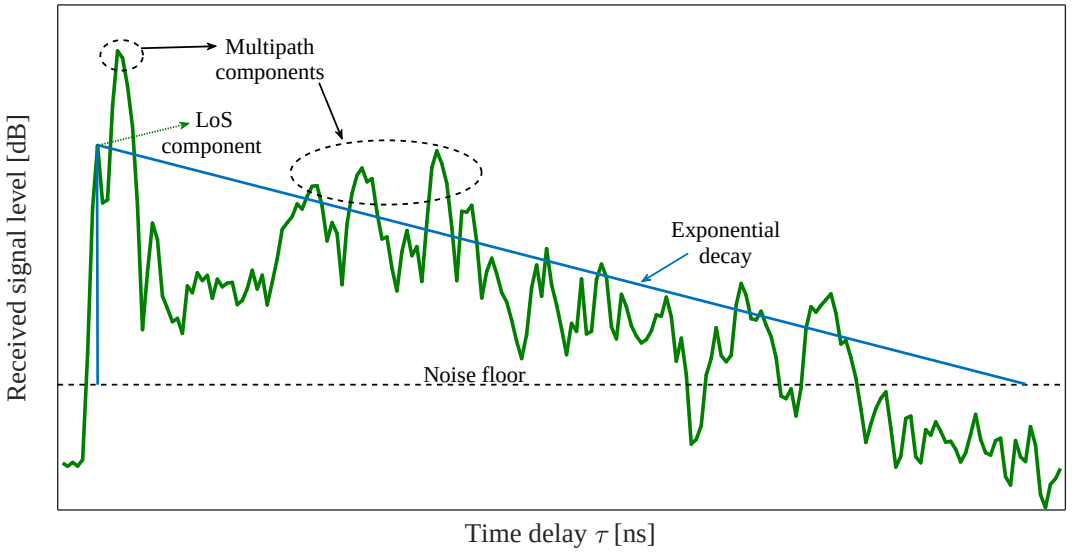

(b) A typical power delay profile with a stronger NLoS component.

FIGURE 2.5: Power delay profile of an indoor wireless channel.

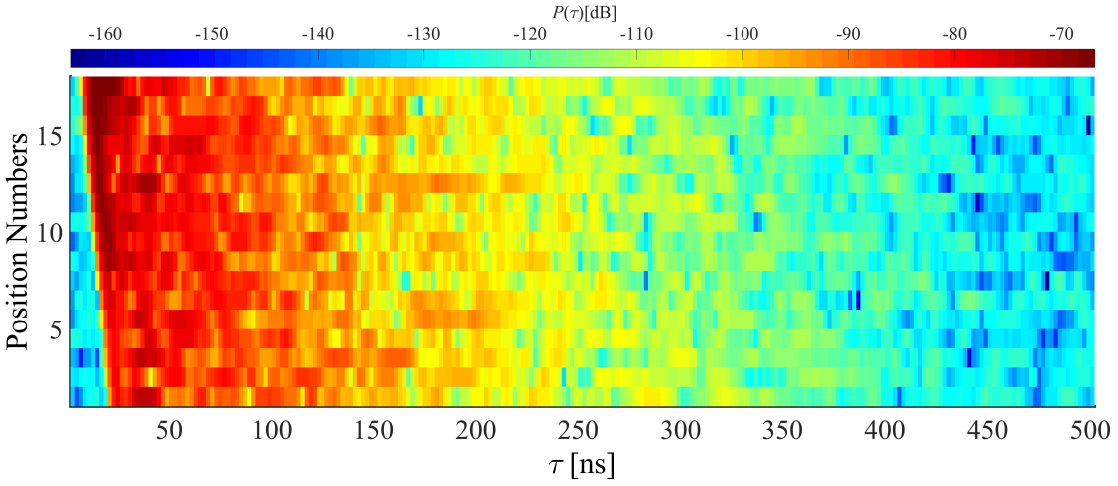

(a) PDP of the Tag-RX1 channel for the LoS case in the Tag scenario.

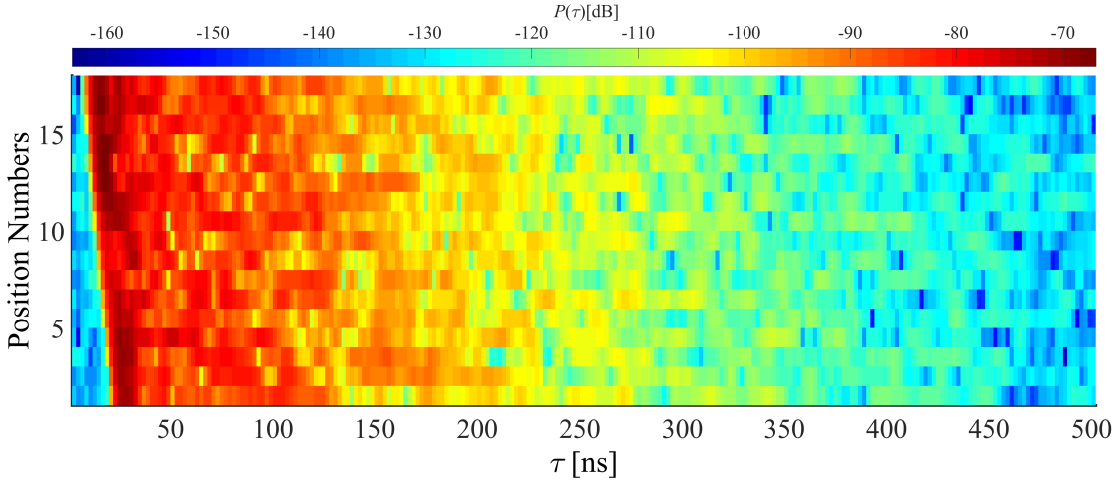

(b) PDP of the Tag-RX2 channel for the LoS case in the Tag scenario.

FIGURE 2.6: Contour plots of power delay profiles for the LoS case in the Tag scenario.

$\sigma_n/\sqrt{N}$, which is equivalent to 20log$N$ enhancement in the SNR [121]. Therefore, the power delay profile P as a function of delay τ is calculated as [123, 126–128]

$$P(\tau) = |IDFT[H(f) * hann(f)]|^2. \tag{2.4}$$

In Figure 2.6 and Figure 2.7, for the LoS and NLoS case, respectively, in the Tag scenario, the average-PDP (APDP) is plotted on the z-axis with delay domain on the x-axis and different position numbers on the y-axis. For the LoS-positions which are nearer to RX1 and RX2 and are unobstructed by the large engine test bed, the LoS component is stronger than the multipath components. To be able to get reasonable results from a narrowband ranging/DoA estimation system, it is paramount to have the

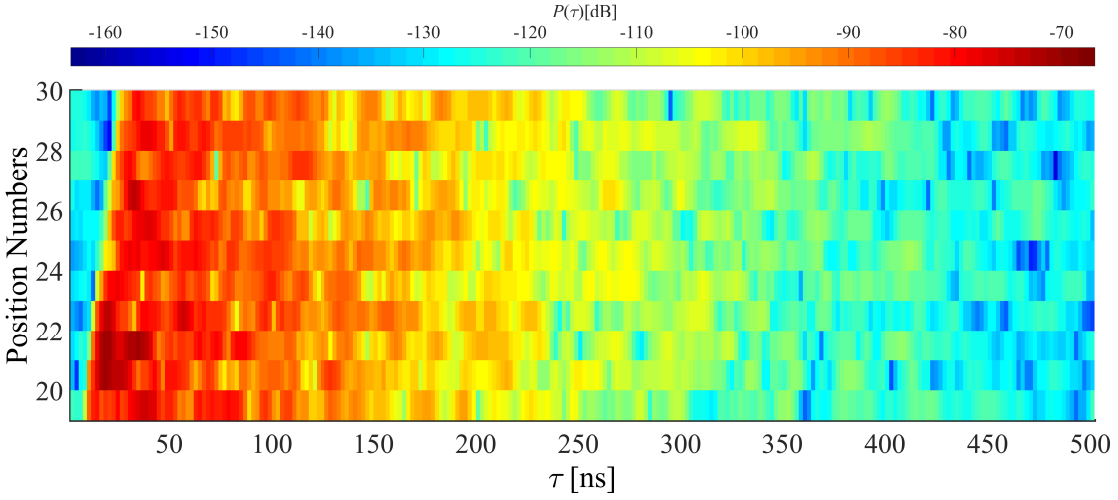

(a) PDP of the Tag-RX1 channel for the NLoS case in the Tag scenario.

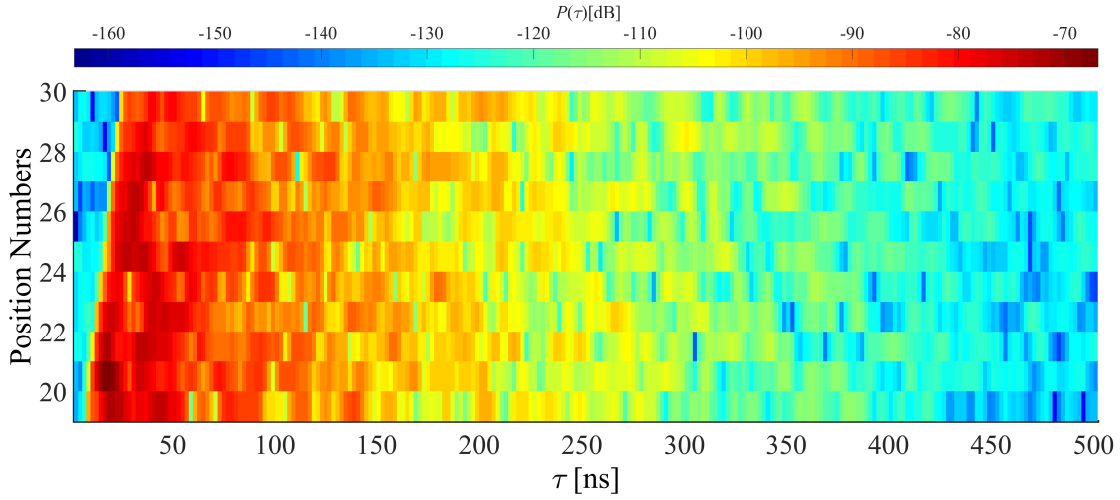

(b) PDP of the Tag-RX2 channel for the NLoS case in the Tag scenario.

FIGURE 2.7: Contour plots of power delay profiles for the NLoS case in the Tag scenario.

LoS component the dominant one in the APDP. It is also evident that with increasing the distance between the tag and reader receiver antennas, the delay of the LoS component arrival is increasing. For the LoS case in the Tag scenario, the maximum $P(\tau)$ is -55.38 dB and minimum is of -80.12 dB. For positions 1 till 5 at RX2, strong multipath components are present. For the NLoS scenario, the maximum $P(\tau)$ is -70.02 dB and minimum values is -83.86 dB. Similar results were achieved for the Reference scenario measurements, with better received power values. The APDPs for all the positions in the Tag and Reference scenarios are plotted in Appendix A.

2.2.2 Dispersion Parameters

In addition to fading, the radio channel also incorporates time dispersion. When a narrow pulse is sent across a wireless channel, multiple copies of the transmitted pulse (spread-out in time) are received at the receiver. The extent of this spread-out of transmitted signal in time, is dependent on the amount of multipath richness present in the environment.The spreading of a narrow pulse is measured quantitatively in terms of the standard deviation about the mean delay, i.e., the delay spread. The delay spread is vital in figuring out the affordable data rate without encountering distortion in a channel.

Defining L as the number of distinct multipath components, P_l (linear value) is the power of the lth multipath component and τ_l is the corresponding delay of that multipath component. The mean delay $\overline{\tau}_{\mathrm{m}}$ is the normalized first order moment of the power delay profile $P(\tau)$

$$\overline{\tau}_{\mathrm{m}} = \frac{\sum_{l=1}^{L} P_l \tau_l}{\sum_{l=1}^{L} P_l}. \tag{2.5}$$

RMS delay spread τ_{RMS} is the normalized second order central moment of the average power delay profile and is calculated via the mean delay $\overline{\tau}_{\mathrm{m}}$ [123]

$$\tau_{\mathrm{RMS}} = \sqrt{\frac{\sum_{l=1}^{L} P_l (\tau_l - \overline{\tau}_{\mathrm{m}})^2}{\sum_{l=1}^{L} P_l}}. \tag{2.6}$$

Although these parameters are estimates, they govern some interesting parameters in a wide sense stationary (WSS) channels. $\overline{\tau}_{\mathrm{m}}$ is related to the ranging error in phase based ranging systems. The RMS delay spread is usually reported to increase with increasing distance [129], which is also the case if we look at Figure 2.6 for the LoS case and in Figure 2.7 for the NLoS case, both in the Tag scenario. For both RX1 and RX2 in the LoS case, the least τ_{RMS} is for the 18th position, which is nearest to RX1 and RX2. Moving away to the farthest positions, the τ_{RMS} increase. In the NLoS case, despite the strong multipath components, the τ_{RMS} is increasing form position 19 to wards position 30. The maximum τ_{RMS} is 36.6 ns and 39.45 ns over the reverse links at RX1 and RX2,

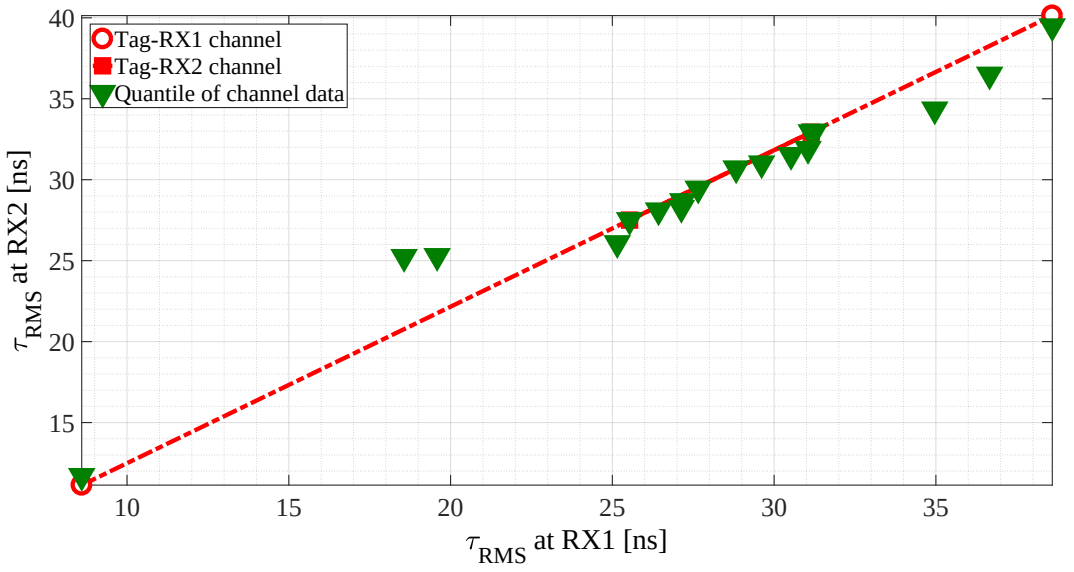

(a) Comparison of the τ_{RMS} of the Tag-RXI channel to the τ_{RMS} of the Tag-RX1 channel in the LoS scenario

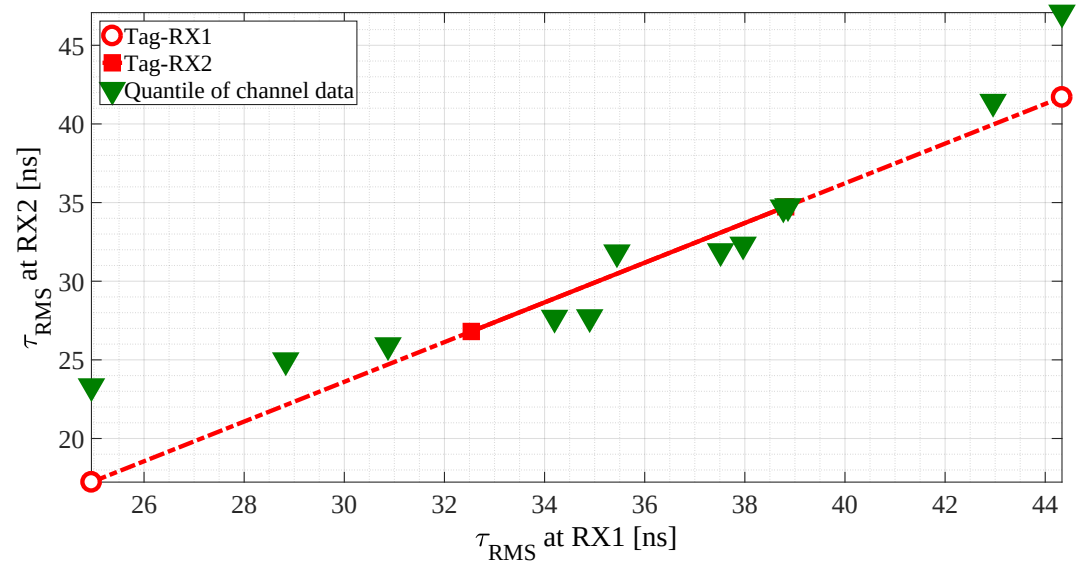

(b) Comparison of the τ_{RMS} of the Tag-RXI channel to the τ_{RMS} of the Tag-RX2 channel in the NLoS scenario

FIGURE 2.8: Comparison of the τ_{RMS} over the reverse SIMO channels in the Tag scenario.

respectively. In the NLoS case in the Tag scenario, the maximum τ_{RMS} is 44.3 ns and 47.1 ns over the reverse links at RX1 and RX2, respectively.

For a reasonable phase-based DoA estimation and range estimation, the wireless channel should behave the same for both RX1 and RX2. For this, the quantile-quantile (qq) plot of τ_{RMS} for RX1 and RX2, for the LoS and NLoS cases in the Tag scenario are shown in Figure 2.8(a) and Figure 2.8(b), respectively. The plot produces an approximately straight line, suggesting that the two sets of sample data have the same distribution. If τ_{RMS} at RX1 and τ_{RMS} at RX2 come from a population with the same distribution, the points of the qq-plot should fall approximately along the reference line $y = x$. The greater the departure from this reference line, the greater the evidence for the conclusion that the two data sets have come from populations with different distributions. In Figure 2.8(a) for the LoS case, both the channels behave quite similar in terms of the τ_{RMS}, even it is not that bad for the NLoS case, as shown in Figure 2.8(b). Majority of the markers in Figure 2.8(a) are near the straight line, showing that over the LoS path, the backward channel conditions are quite similar for both RX1 and RX2. As shown in Figure 2.8(b), the τ_{RMS} of the NLoS path is quite different for both RX1 and RX2. Only a few markers are in close proximity of the straight line, showing a clear demarcation of the two reverse NLoS channels from each other.

2.2.3 Power Ratio: K Factor

For localization, the ratio of the power of the LoS path to the power of the indirect paths (multipaths) is another important parameter. It is termed as the K factor. It gives the effect of the direct (LoS) path on the entire delay profile It can be calculated by [127]

$$K = 10 \log_{10} \left(\frac{P_{\text{LoS}}}{P_{\text{multipath}}} \right). \tag{2.7}$$

Where P_{LoS} is the power of the LoS component and $P_{\text{multipath}}$ is the combined power of the MPCs. $P_{\text{multipath}}$ can be found as

$$P_{\text{multipath}} = P_{\text{LoS+multipath}} - P_{\text{LoS}}. \tag{2.8}$$

By considering the power ratio, we can distinguish between the scenarios leading to high and low τ_{RMS} values. If the direct path is dominant in the PDP, i.e., a high K factor

value, we will be able to get accurate results employing narrowband ranging techniques. Therefore, the K factor value depends on the location inside the engine test bed.

From Figure 2.9, the highest K factor is for the 18th position (for both of the reverse channels, in both of the Reference and Tag scenarios), i.e., right in front of RX1 and RX2. Consequently, experiencing a low τ_{RMS}. Closely looking at Figure 2.9, the SIMO configuration helps in getting a good value of the K factor at least at one of the RX1 and RX2. The positions where this happens, we expect to have better localization results. The values of K factor over the TX–Tag forward channel, for the tag positions 1 and 2 show very poor results. These positions do not have a LoS path between the tag and RX1 & RX2. The path is somewhat obstructed by the large engine test bench. For the rest of the LoS positions, we will study the results in conjunction with the system analyzer.

In the NLoS scenario, the signals predominantly experience scattering, with some diffraction and reflection as well. As evident from Figure 2.10, the K factor values for the TX to tag antenna at the NLoS positions are not encouraging. In particular at the positions where the K factor values are appreciably low at both of RX1 and RX2, the localization results will not be encouraging.

2.3 Summary

In this chapter, the radio channel inside an engine test bed environment has been analyzed via the time delay characterization. The analysis is carried out to analyze the available power of the LoS in comparison to the multipath components, which is paramount for narrowband ranging techniques. The investigation shows that the K factor is predominantly low for the NLoS case, but using a SIMO configuration, a better performance can be achieved. With the delay spread and PDP analysis, as expected the RMS delay spread was found to be increasing with the increase in the TX–RX antenna separation. According to the floor plan, each of the position number 4 up till 18 provides the possibility of a strong LoS communication channel, from the tag antenna to both RX1 and RX2, albeit in the presence of multipath.

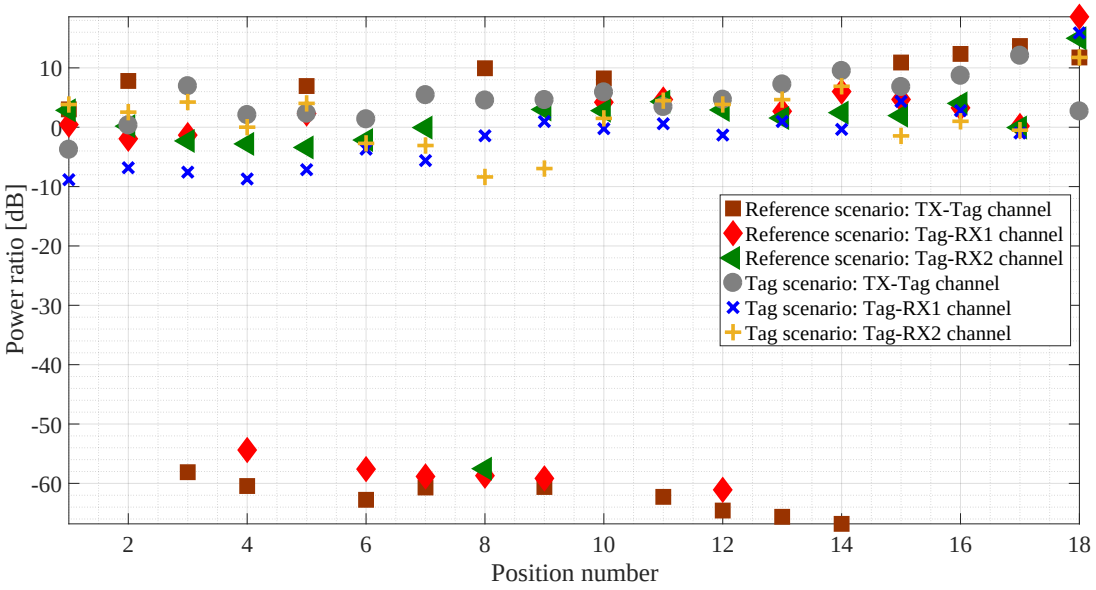

FIGURE 2.9: Power ratio plot for the LoS case.

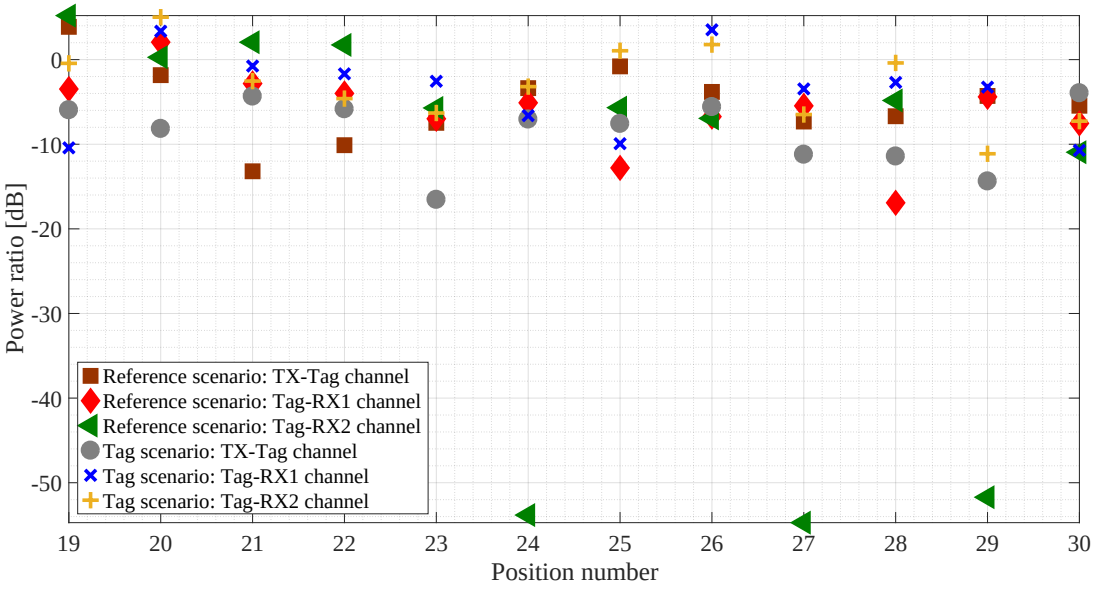

FIGURE 2.10: Power ratio plot for the NLoS case.

Chapter 3

RFID System Analyzer Framework

In this chapter, I will present the development of the measurement based system analyzer. Further, I will incorporate the positioning capabilities in the design of the analyzer, i.e., for the DoA and the range estimation of an RFID tag. The results of DoA and range estimation are discussed later in the chapter.

3.1 Basic System Analyzer

In a large system design, many number of boxes in Simulink™ might cause the system to be difficult to understand, I will simplify the system analyzer implementation by grouping blocks into subsystems. Apart from being lucid, subsystems will make it easy to keep blocks with related functionality together, thus establishing a hierarchical system design with different layers. There is also a provision of executing subsystems conditionally or unconditionally. This depends on the input signal to the subsystem, whether or not the subsystem will be executed.

A generic system analyzer is shown in Figure 3.1. The RF signal of carrier frequency 890 MHz is generated in the "Reader Transmitter" section via the continuous wave (CW) block, i.e., "RFID C.W TX." The CW block is scalable, and can produce a sinusoid up to GHz frequency range. As shown in Figure 3.2, we can adjust the input power level (in W, mW, dBm or dBW), phase of the source wave (in degrees) and the carrier frequency. One configuration block has to be connected to each topology built

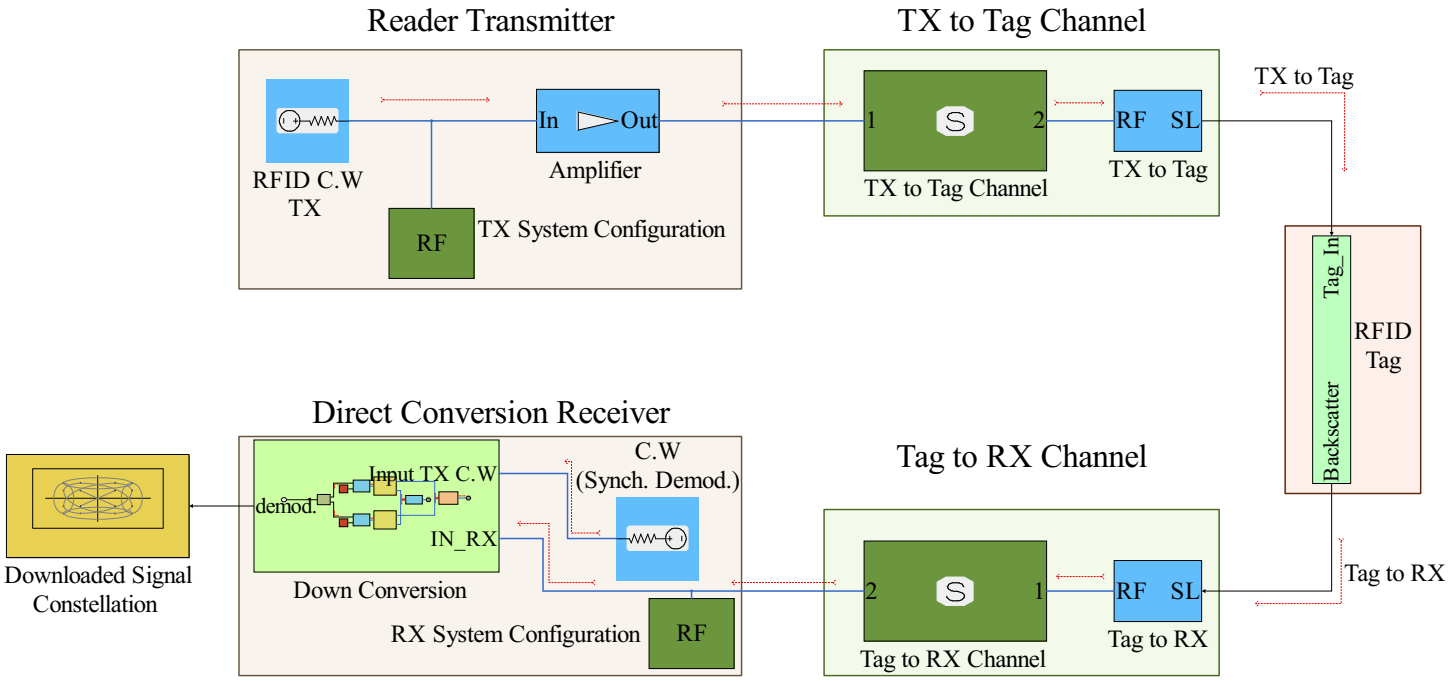

FIGURE 3.1: A generic system analyzer.

in SimRF™. Configuration block in SimRF™ sets the model conditions for a circuit envelope simulation [130]. As depicted in Figure 3.3, the configuration block parameters define a set of simulation frequencies, solver attributes, and thermal noise. By setting appropriate values, the analyzer can be modeled to replicate a real world microwave device.

After passing through the amplifier, the CW is fed to the two-port scattering (S) parameters block, i.e., "TX to Tag Channel." The S-parameters block models a network defined by S-parameters in the SimRF™ circuit envelope simulation environment. The S-parameters block attributes are shown in Figure 3.5. The block can have a maximum of up to four ports. For this case of a generic RFID communication system, I have utilized a 2-port S-parameters block. The S-parameters of a particular channel can be plugged in this S-parameter block in SimRF™. The S-parameters can also be loaded using a compatible touchstone file [130]. This arrangement emulates a real physical channel for the RF signals for our backscatter RFID channel. At port1, we have the CW coming from the amplifier block and port2 is connected to the block "TX to Tag." This block converts the signal from the SimRF™ environment to the normal Simulink® environment. The blocks with blue connecting lines are part of the SimRF™ library.

After passing through the forward channel of "TX to Tag Channel," the signal arrives at the "RFID Tag" block. The tag subsystem is capable of handling realistic modulation states. This block can be modeled as shown in Figure 3.4, based on the design values of [63]

$$\begin{aligned} Z_{\text{Ant}} &= (68 + j442)\Omega, \\ Z_{\text{Abs}} &= (68 - j442)\Omega, \\ Z_{\text{Ref}} &= (2 - j0.1)\Omega. \end{aligned} \tag{3.1}$$

In my design of the system analyzer, the tag antenna is part of the channel measurements. Therefore, I will utilize the concept of ASK modulation efficiency of equations 1.6 and 1.7. A fixed tag ID number is stored in the tag subsystem. The tag backscatters the CW using ASK modulation (as per the tag ID), based on equation 1.7.

After the RFID tag subsystem, the signal is converted back to the SimRF™ environment using the "Tag to RX" block. This block can also be configured for different operating frequencies, as shown in Figure 3.6.

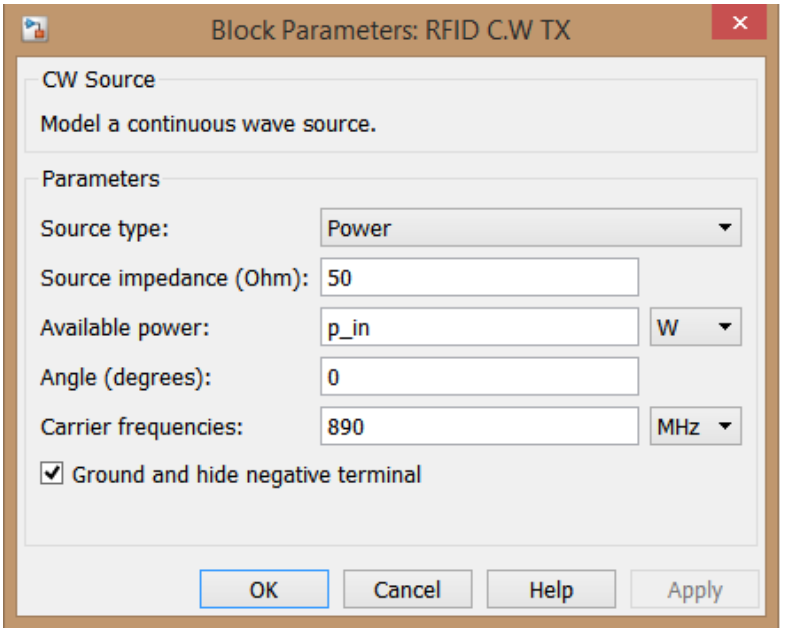

FIGURE 3.2: Continuous wave generation block in SimRF.

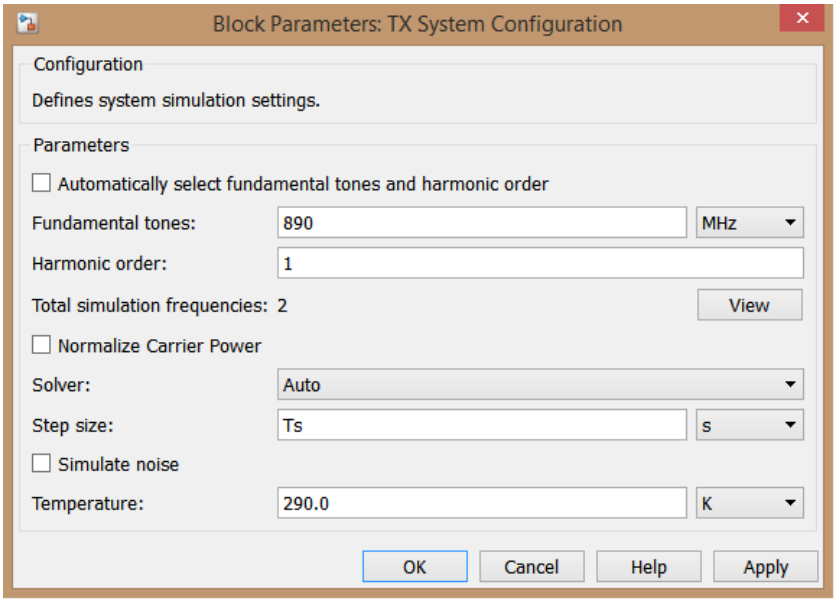

FIGURE 3.3: System configuration attributes list.

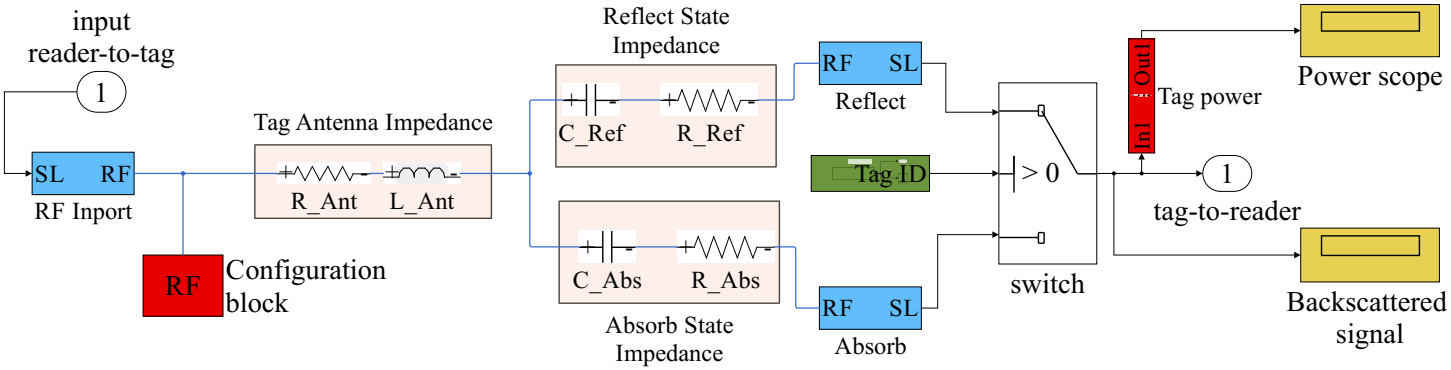

FIGURE 3.4: An RFID tag impedence modelling in SimRF.

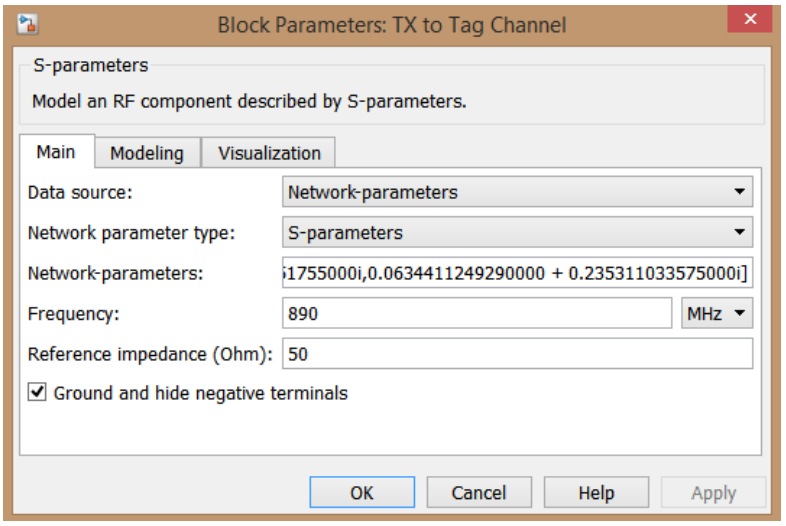

FIGURE 3.5: Attributes of the *S*-parameters block.

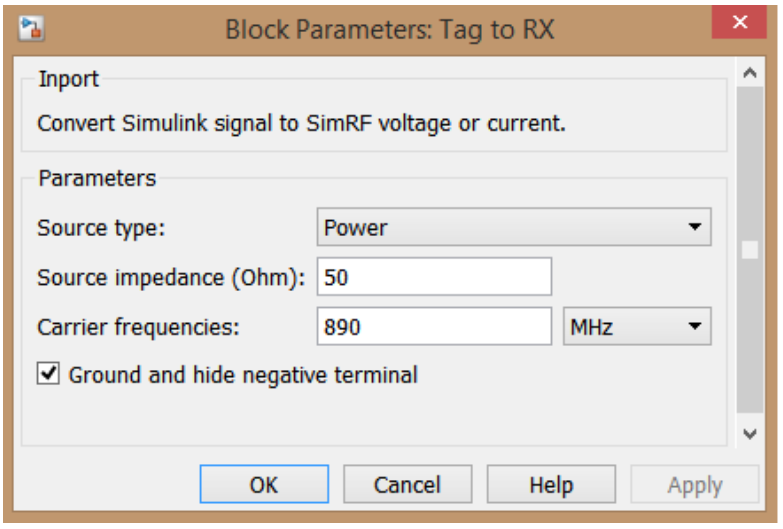

FIGURE 3.6: Block for conversion of signals from the Simulink environment to the SimRF environment.

Once the signal from the tag has been translated into the SimRF environment, it is fed to the port1 of the *S*-parameters block "Tag to RX Channel." This *S*-parameters block is emulating the reverse channel from the RFID tag to the RFID reader receiver. After passing through the reverse channel, the signal is fed to the "Direct Conversion Receiver" block, where the signal is demodulated synchronously. The downconversion subsystem is shown in Figure 3.7 [131]. A CW block (like the one used at the TX) is used here for this purpose. The downconverted signal can be viewed on a "Constellation Diagram Scope." Figure 3.8 shows the constellation diagram of the downconverted signal, i.e., the S_{Ref} and S_{Abs} states.

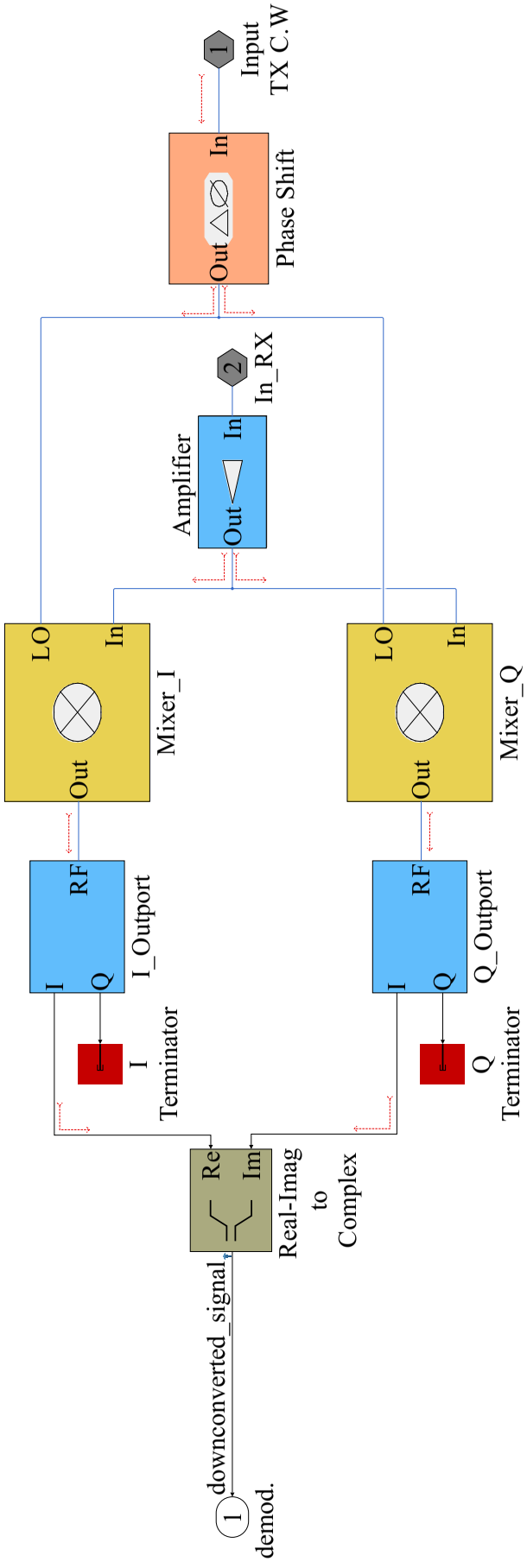

FIGURE 3.7: Signal down conversion subsytem.

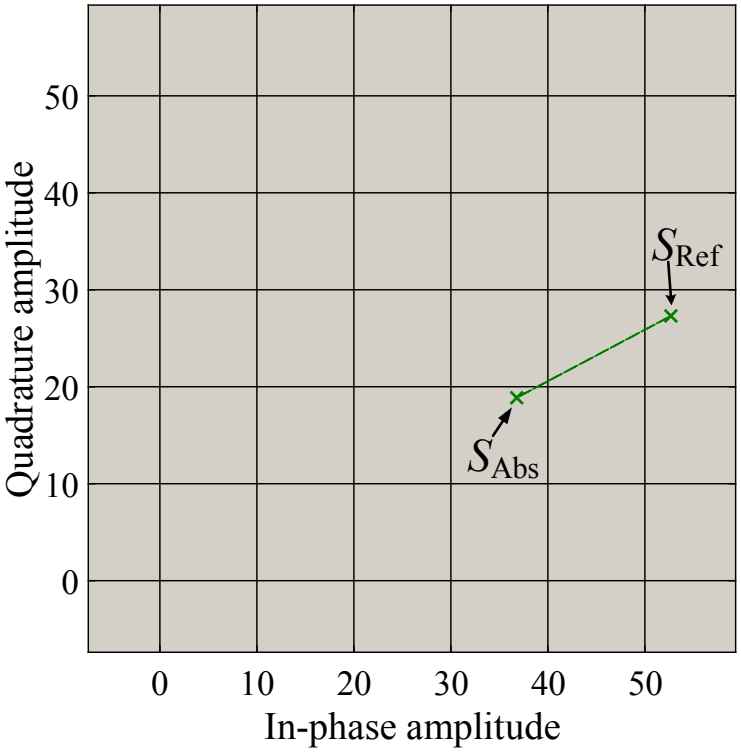

FIGURE 3.8: Downconverted signal constellation.

3.2 Analyzer Implementation for DoA Estimation

The DoA estimation system analyzer is entirely developed in the Simulink® [132, 133] which is a graphical programming extension of Matlab® for modeling, simulating, and analyzing dynamic systems. I have used the SimRF™ tool box within the (Simulink® environment) for handling the RF signals.

The SD-PDoA based system analyzer [134] has six blocks, as shown in Figure 3.9. These blocks are

i. The reader transmitter (continuous carrier wave generation) block

ii. The S-parameters channel block

iii. The RFID tag block

iv. The reader receiver 1

v. The reader receiver 2

vi. The DoA calculation block

The first five blocks are explained in section 3.1. As for the SD-PDoA technique, a SIMO configuration has to be employed. Therefore, the 2-port S-parameter block of the SISO RFID analyzer (Figure 3.1) is extended into a 4-port block. At port1 of the S-parameter block—CW signal is attached as an input, at port2 is the reader receiver number one (RX1), at port3 is the reader receiver number two (RX2) and finally at port4 is the RFID tag subsystem. This arrangement is the same as was in the AVL channel measurement campaign explained in chapter 2. The S-parameters:

$$\mathbf{S} = \begin{bmatrix} S_{11} & S_{12} & S_{13} & S_{14} \\ S_{21} & S_{22} & S_{23} & S_{24} \\ S_{31} & S_{32} & S_{33} & S_{34} \\ S_{41} & S_{42} & S_{43} & S_{44} \end{bmatrix}, \tag{3.2}$$

of a particular position of the tag, are plugged in the S-parameter block in SimRF. The two paths from the TX–tag–RX1 and TX–tag–RX2 constitute the SIMO system.

The received backscattered tag signal waveforms at both RX1 and RX2 are shown in Figure 3.10. Tag ID and Enable ID signals are the control signals, operating in the

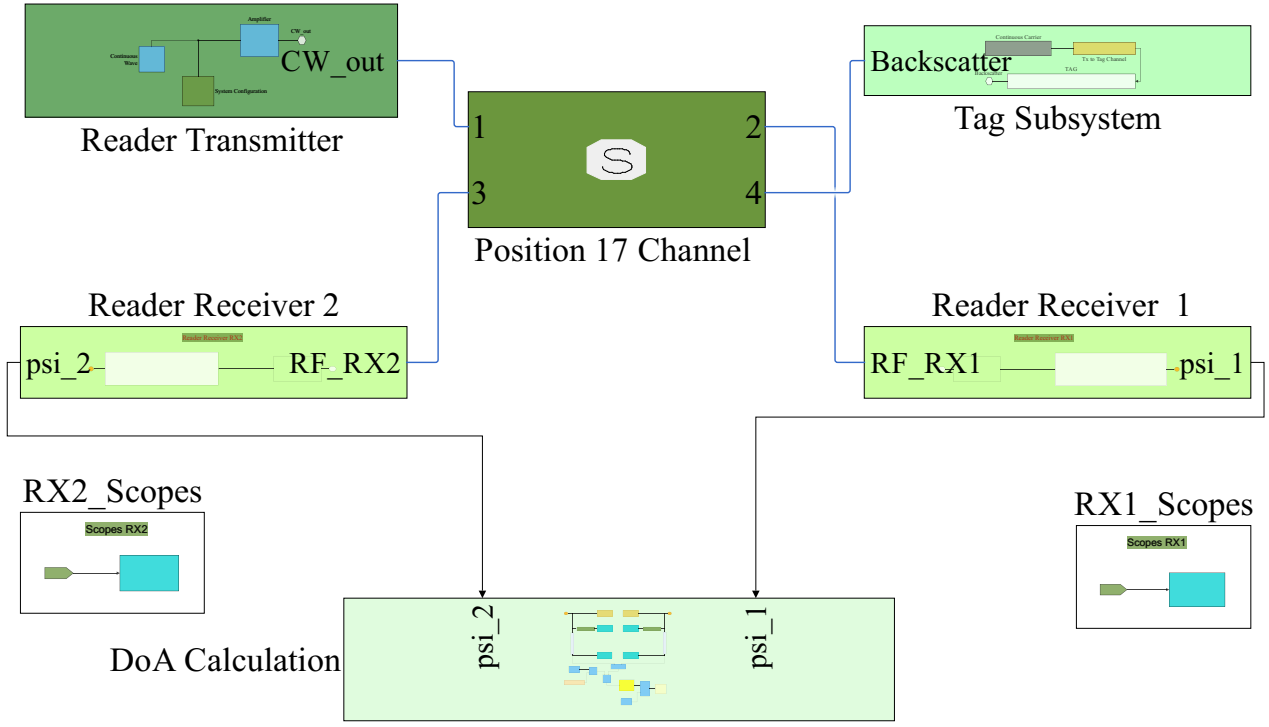

FIGURE 3.9: SIMO RFID Simulink® analyzer: The solid blue connecting lines depict a connection between blocks in the SimRF environment and the black connections depict processing in the Communications system toolbox and the DSP system toolbox [134].

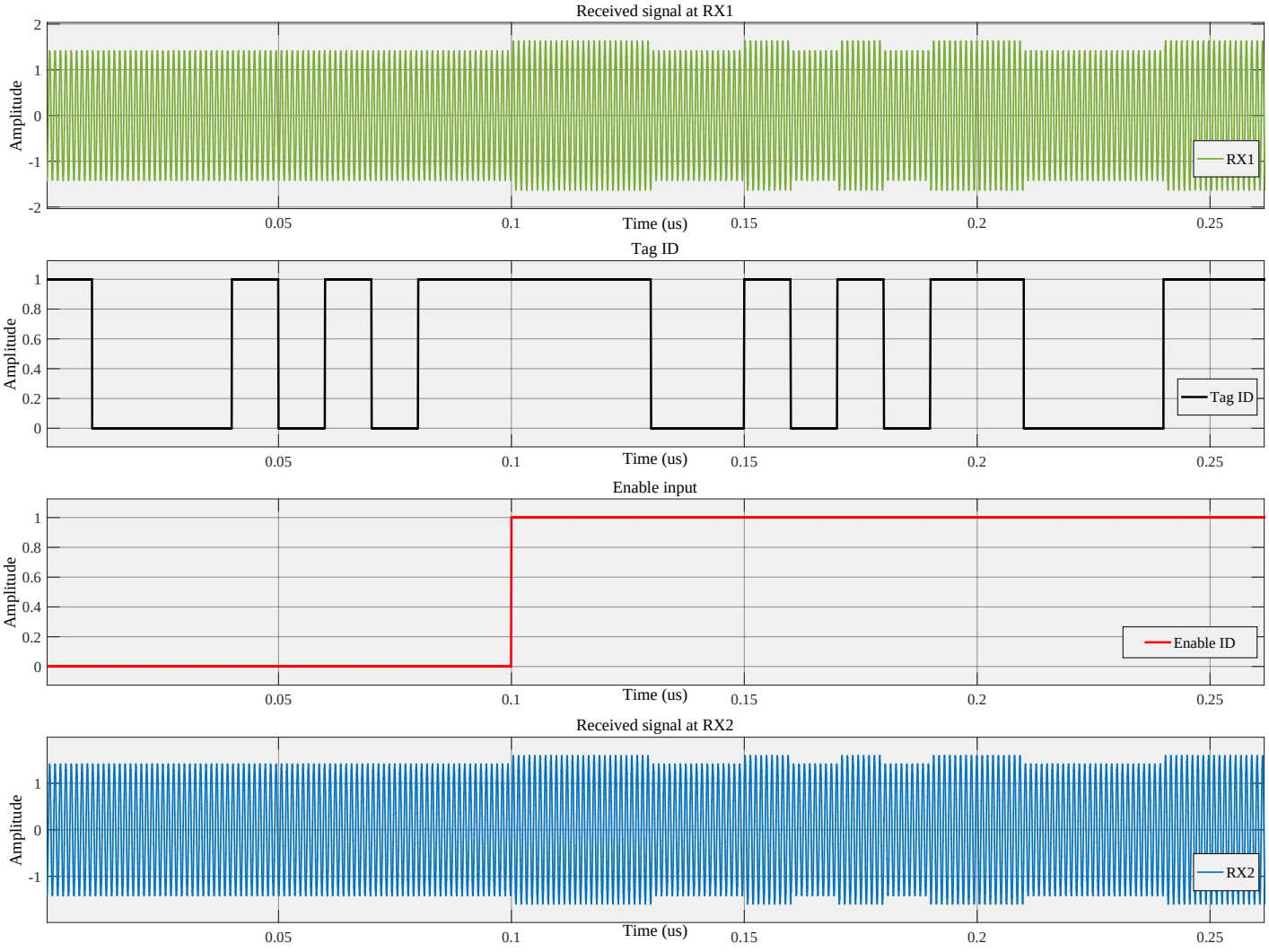

FIGURE 3.10: Received backscattered tag signal waveforms at RX1 and RX2.

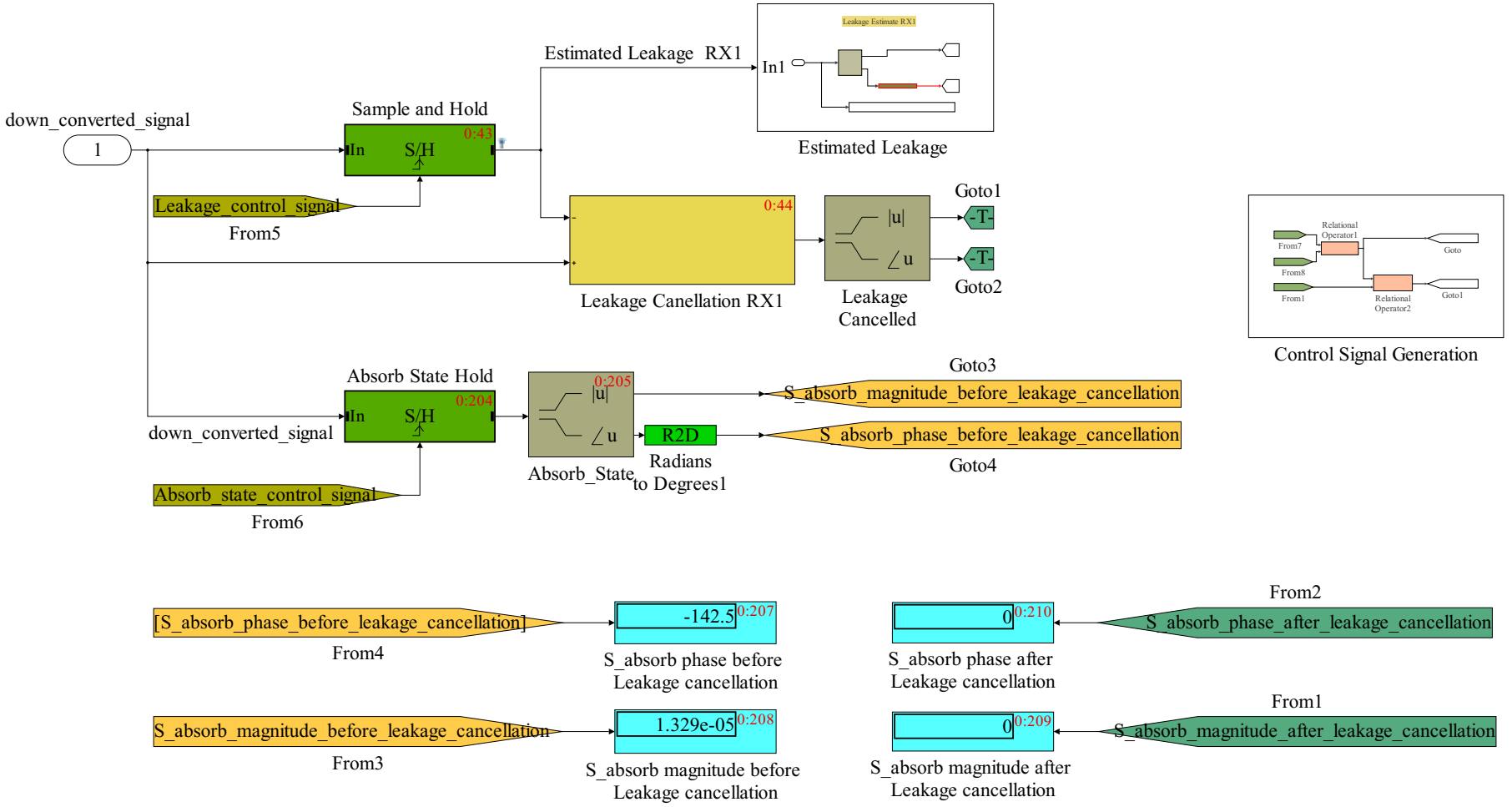

FIGURE 3.11: Leakage cancellation subsystem.

"Tag Subsystem" of Figure 3.9. The Tag ID signal is the serial identification number of a particular tag. The Enable ID is controlling the backscatter modulation via a switch. Until the value of Enable ID is below 1, the S_{Abs} is calibrated, hence the leakage. After the Enable ID goes to 1, the tag backscatters by ASK modulation of the CW carrier signal as per the tag ID. After estimating the value of S_{Abs}, the tag backscatter signal passes through the S-parameters block, thus emulating the two reverse channels from tag to RX1 and RX2. Inside both of the "Reader Receiver 1" and "Reader Receiver 2" subsystems, the backscatter signals are downconverted using the direct conversion receiver shown in Figure 3.7. After downconversion, the signal constellation at both RX1 and RX2 looks like the one in Figure 3.8.

The complex valued downconverted signals from both reader receivers are fed to the leakage cancellation subsystems, which is inside both of the"Reader Receiver 1" and "Reader Receiver 2" subsystems, as shown in Figure 3.11. In the leakage cancellation block, the estimated complex valued-leakage is subtracted from the incoming downconverted signal. The scopes in Figure 3.11 show that the magnitude and phase of the S_{Abs} state are zero, meaning that the value of the leakage signal has been deducted and the S_{Abs} is right at the origin. The leakage canceled IQ constellations for both RX1 and RX2 are shown in Figure 3.12 and Figure 3.13, respectively. After the leakage cancellation, the x, y coordinates of the S_{Ref} state are extracted for both "Reader Receiver 1" and "Reader Receiver 2" subsystems. From this, the phases of tag signal at both RX1 and RX2, i.e, ψ_1 and ψ_2, are calculated using the respective IQ values [135],

$$\psi_1 = \arctan(Q_1/I_1), \tag{3.3}$$

$$\psi_2 = \arctan(Q_2/I_2). \tag{3.4}$$

The values of ψ_1 and ψ_2 are then fed to the final block, the DoA calculation block. The phases are adjusted as taken from the positive x–axis reference, in the coordinate adjustment subsystem inside the "DoA Calculation" subsystem, as shown in Figure 3.14. The "DoA Calculation" subsystem is the implementation of equation 1.21 for finding the DoA, ϕ. The performance metric in this work is the incidence angle α, which is the difference between the perpendicular and the DoA (ϕ) [54]:

$$\alpha = 90 - \phi. \tag{3.5}$$

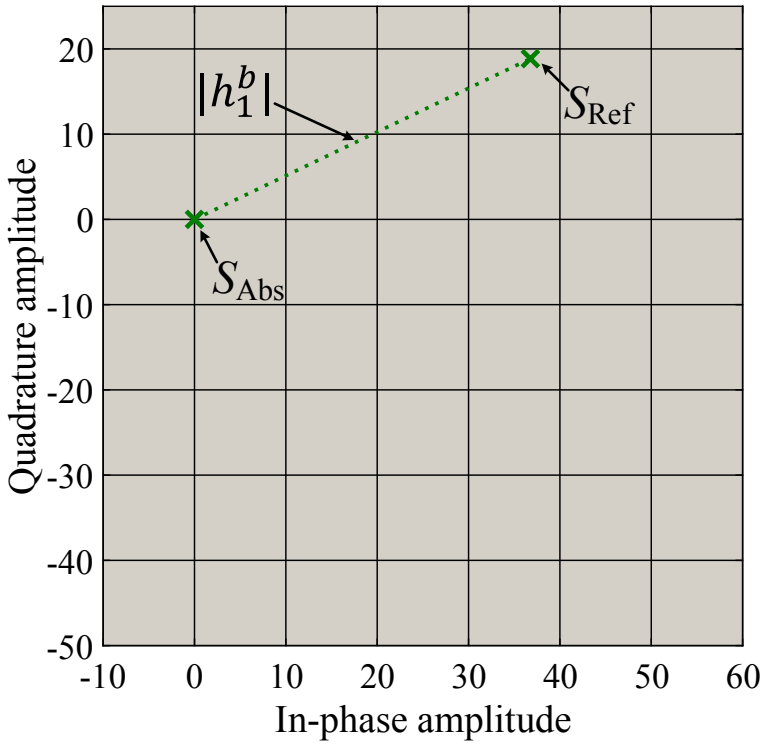

FIGURE 3.12: Leakage canceled signal constellation at RX1.

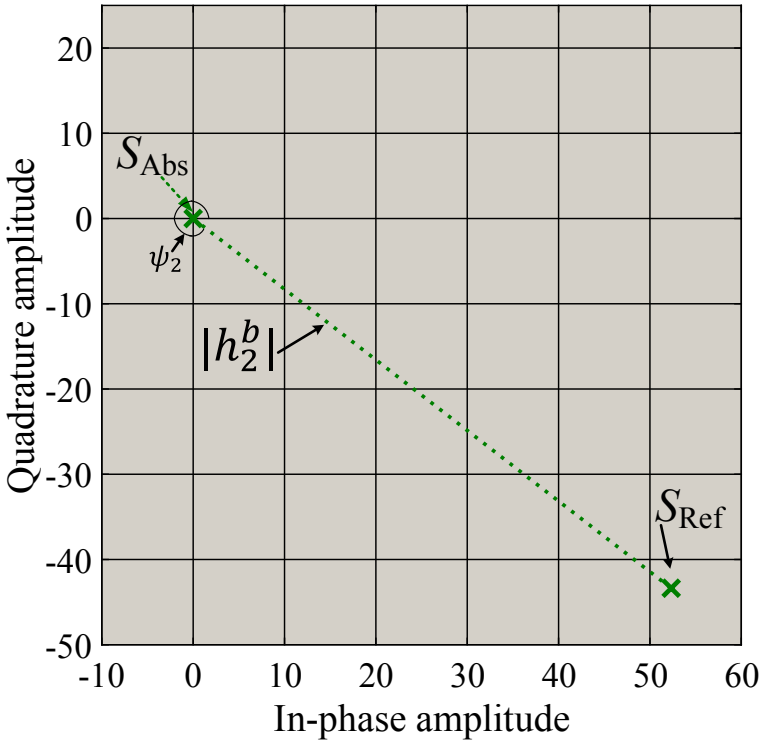

FIGURE 3.13: Leakage canceled signal constellation at RX2.

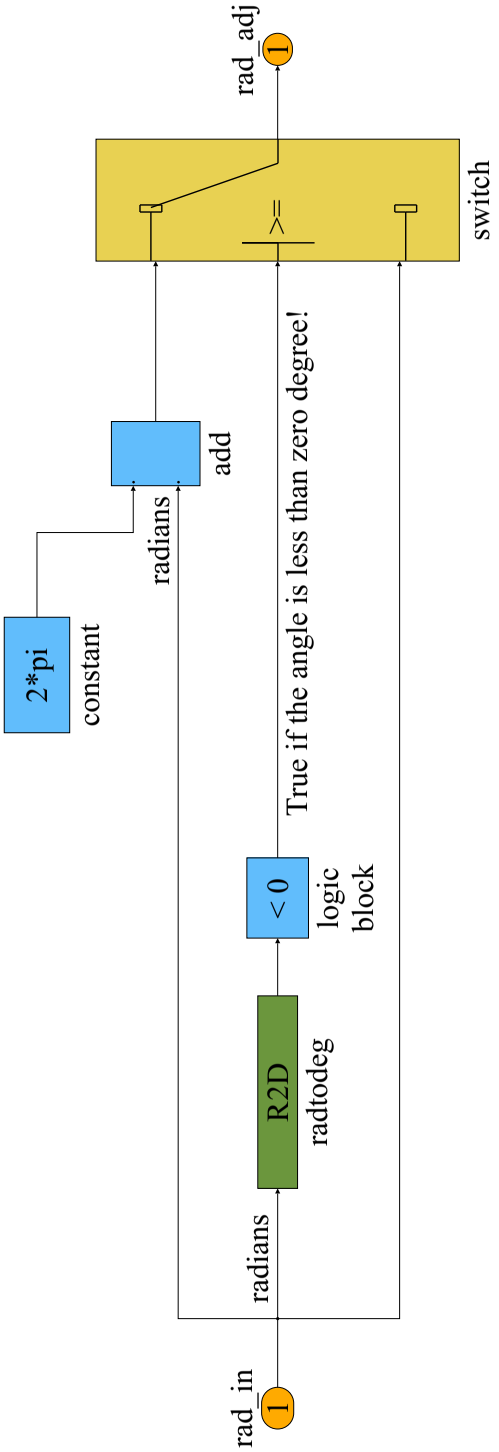

FIGURE 3.14: Adjustment of the coordinates.

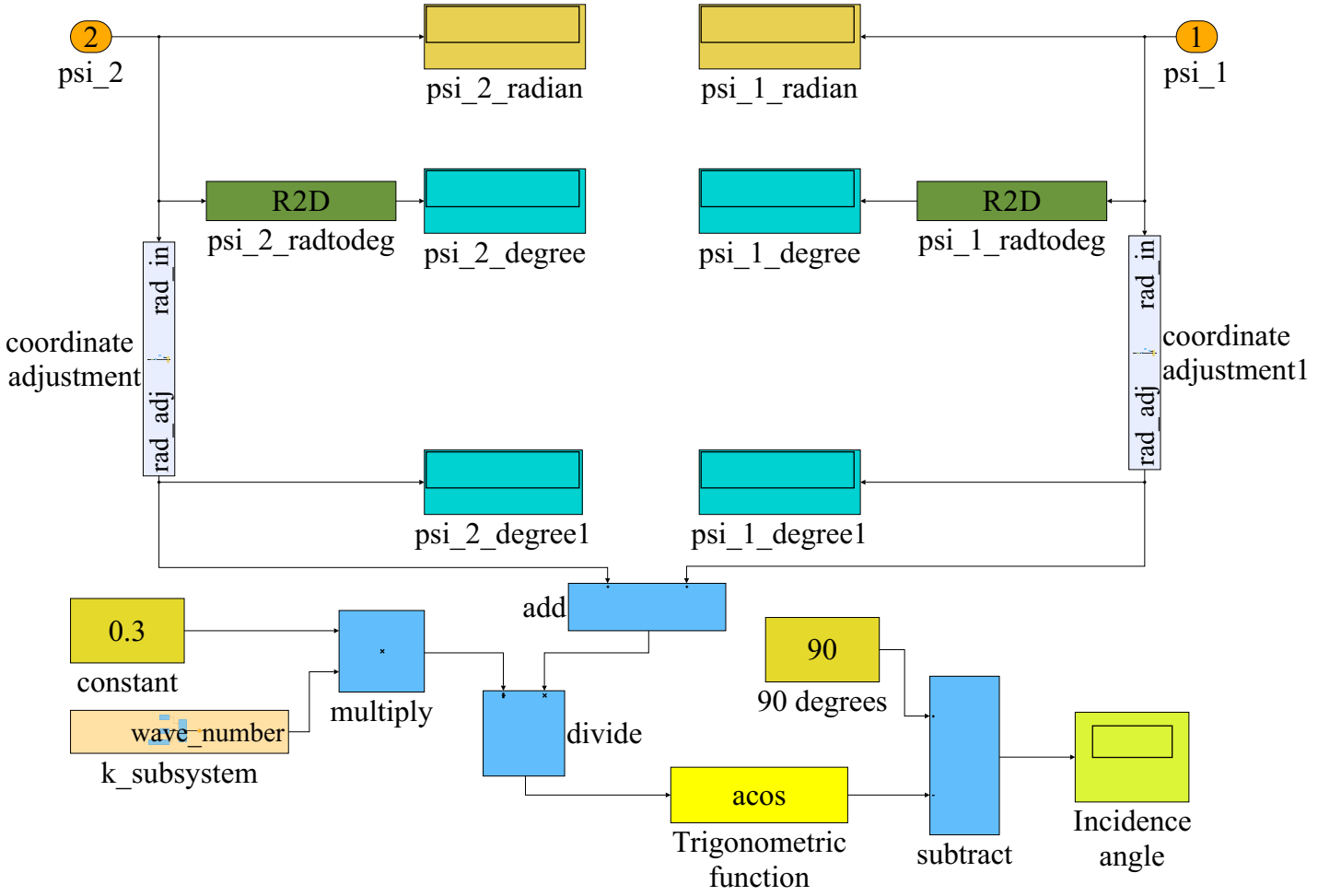

FIGURE 3.15: DoA calculation block.

3.2.1 DoA Verification

In order to validate the system analyzer before using the measured S-parameters of the indoor channel, a measurement campaign was carried out in an anechoic chamber using the same antenna configuration as of the AVL measurement campaign, as shown in Figure 3.16. The origin is taken in the middle of RX1 and RX2. The custom-built patch antenna (used as a tag antenna) is placed on a support made of styrofoam. The tag antenna is placed on 8 positions to the left of the origin (n80–n10) and at 8 positions to the right of the origin (p10–p80). Each of these positions are 10 cm apart, as shown in Figure 3.17. The perpendicular distance from the middle of RX1 and RX2 to the styrofoam is 156.5 cm.

I incorporated the measured S-parameters into the SD-PDoA based system analyzer in order to validate analyzer's performance. The validation results are shown in Figure 3.18. As can be seen that the system analyzer performs quite accurately for almost all of the positions in the anechoic chamber. The exceptions are the two leftmost positions ($n80$ and $n70$) and the two on the right are $p60$ and $p70$. The slight deviation between the geometric and simulated angles can be due to some misalignment, antenna radiation pattern, etc.

3.2.2 DoA Performance Analysis

Plugging the channel S-parameters for each of the 18 LoS positions and 12 NLoS positions separately in the system analyzer, phases at both RX1 and RX2 are extracted as explained in section 3.2. The"DoA Calculation" block in the system analyzer computes the simulated incidence angle, i.e., α_{sim}. The geometric incidence angles for both LoS and NLoS positions are calculated using the geometrical positions of RX1, RX2, and the tag antenna inside the AVL test bed facility. The incidence angle estimation results for the LoS scenario are depicted in Figure 3.19. As discussed in the previous chapter, only coarse-grained localization can be achieved with the employed hardware setup.

The system analyzer performance is evaluated with two different tag antennas. As explained in chapter 2, in the Tag scenario a custom-built patch antenna is used for the tag antenna. Whereas in the Reference scenario a commercially available Motorola AN480 patch antenna is used as a tag antenna. From Figure 3.19 it is evident that the Reference scenario gives better results than the tag scenario. In the Reference scenario

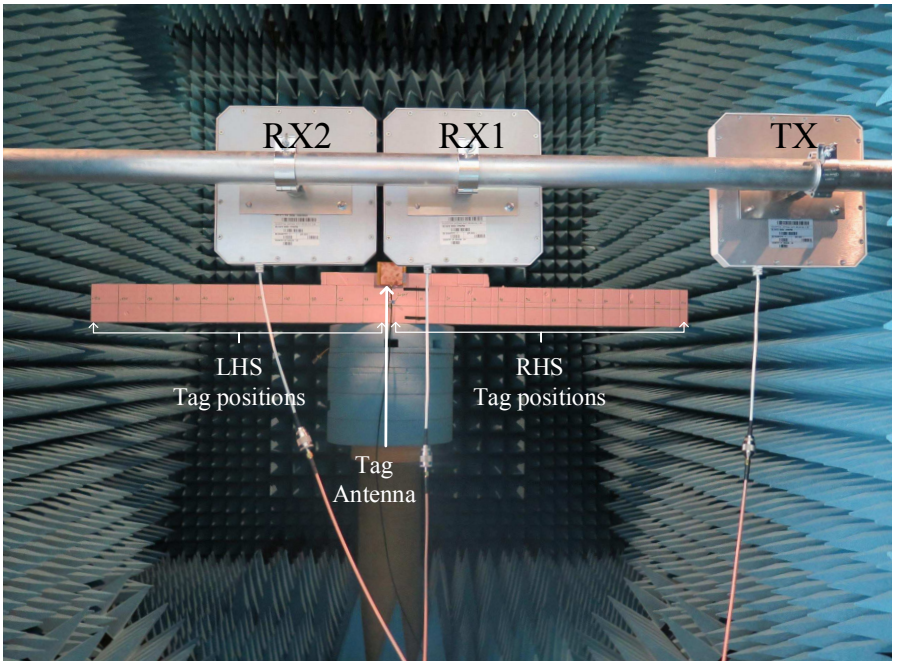

FIGURE 3.16: Antenna setup in the anechoic chamber.

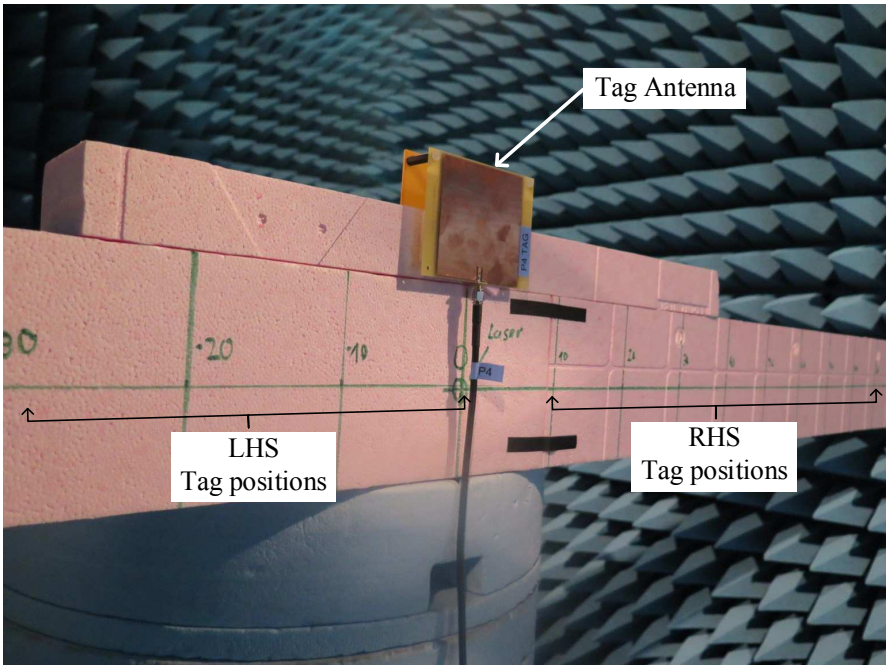

FIGURE 3.17: Different tag antenna positions along the horizontal styrofoam.

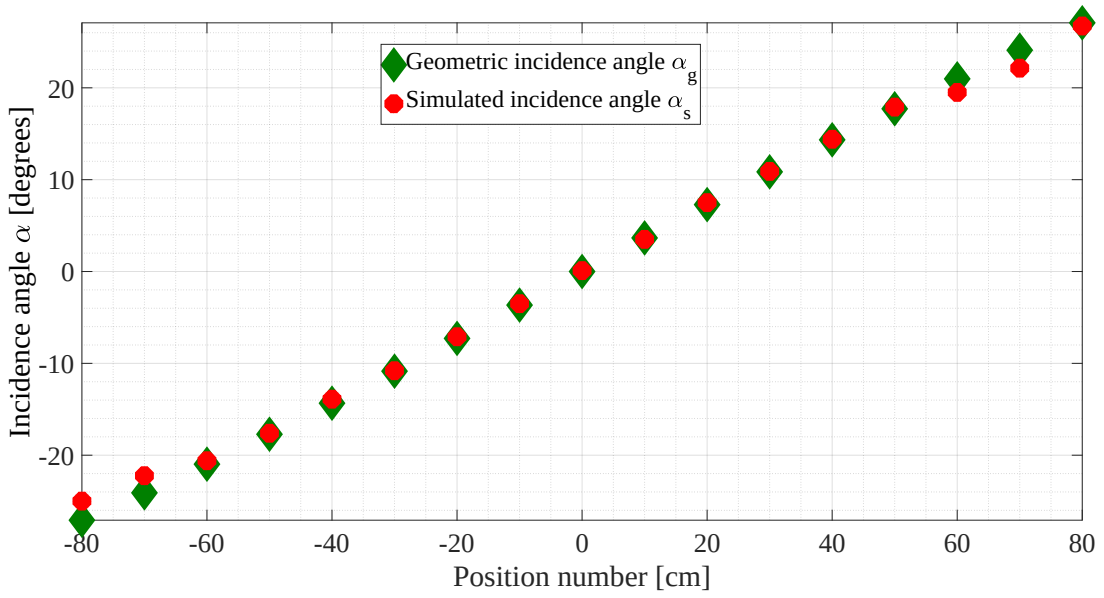

FIGURE 3.18: Validation of the DoA estimation of the system analyzer in the anechoic chamber.

TABLE 3.1: Root mean square error for α_{sim} for both of the reference and tag scenarios.

	Tag Scenario (degree)	Reference Scenario (degree)
LoS	22.04	14.78
NLoS	31.03	25.21

(with $\Diamond$ markers), there are a few outliers at $p5$, $p16$ and $p17$. There is lesser deviation of the $\Diamond$ markers from the $+$ markers (the geometric α_{geo}). Whereas the α_{sim} for the tag scenario ($*$ markers) are quite apart from the α_{geo} at $p1$, $p3$, $p5$, $p6$, $p12$, $p13$, $p14$ and $p17$.

The results are much more evident in the absolute error plots of Figure 3.21 and Figure 3.21, for the LoS and NLoS case, respectively. As noticed, there are large spikes at $p1$, $p3$, $p5$, $p6$, $p12$, $p13$, $p14$, and $p17$ for the Tag scenario. The Reference scenario also has large error values at $p5$, $p16$ and $p17$. Overall, the Reference scenario performs better than the tag scenario for the LoS case.

In the NLoS case, at $p19$, $p20$, $p21$ and $p22$ both the Reference and Tag scenarios are not giving satisfactory DoA estimation results. But for the rest of the NLoS positions, i.e., $p23$–$p30$, Reference scenario is giving satisfactory coarse-grained DoA estimation results. The overall performance of the Tag scenario in the NLoS case is not favorable.

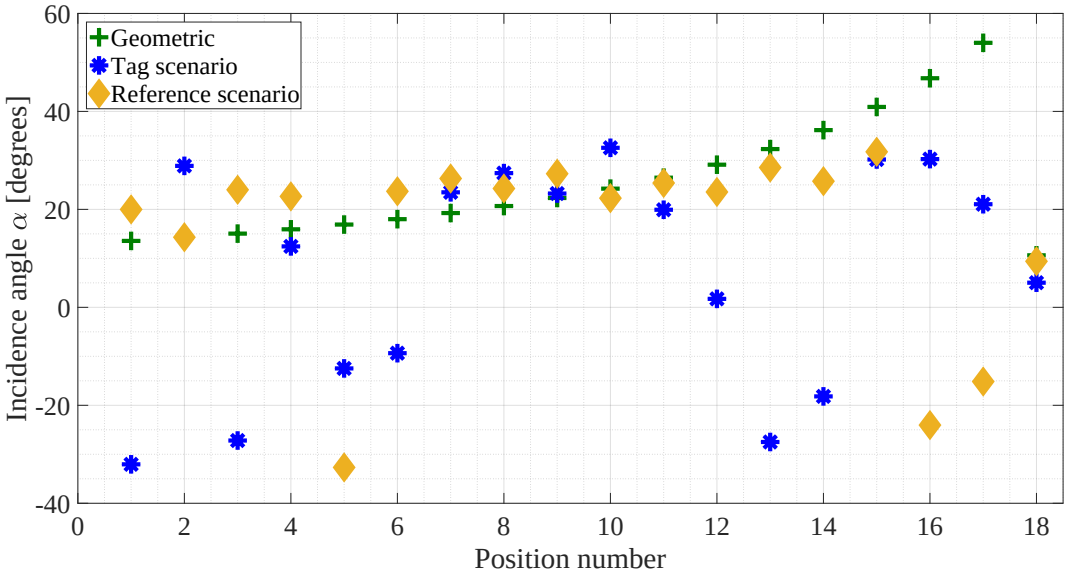

FIGURE 3.19: DoA estimation results of the SD–PDoA based approach for the LoS scenario: The + markers are showing the geometric angles. The ◊ markers are the results for the Reference scenario. Whereas the with * markers are showing the results for the Tag scenario.

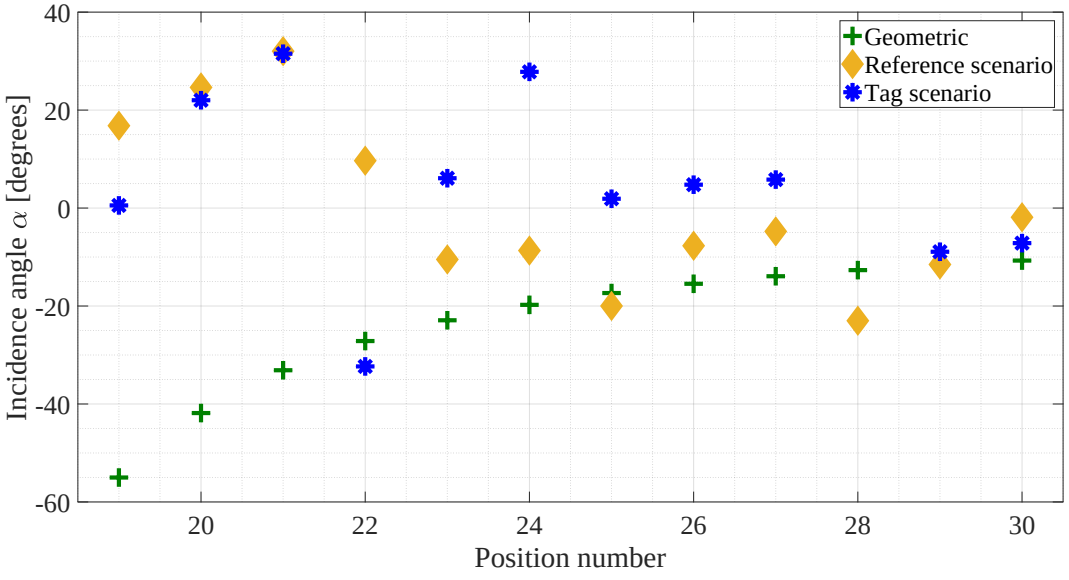

FIGURE 3.20: DoA estimation results of the SD–PDoA based approach for the non-line of sight scenario.

Looking at the absolute error plot of Figure 3.22 for the case of NLoS, it is substantiated that the Reference scenario is performing better than the Tag scenario. To get a single performance metric to understand this fact, the root mean square error (RMSE) of the SD-PDoA based results for both of the Tag and the Reference scenario is calculated by

$$\hat{\alpha} = \sqrt{\frac{1}{N_p} \sum_{p=1}^{N_\mathrm{p}} \left(|\alpha_\mathrm{geo} - \alpha_\mathrm{sim}|^2 \right)}, \tag{3.6}$$

where N_p is the number of tag positions, i.e., 18 for the LoS and 12 for the NLoS case, α_geo is the geometrical incidence angle and α_sim is the simulated incidence angle.

The RMSE values for the LoS and the NLoS case for both of the Tag and Reference scenarios are given in Table 3.1. The RMSE values for the case of the Reference scenario in such a severe multipath environment (inside the AVL engine test bed) are quite reasonable.

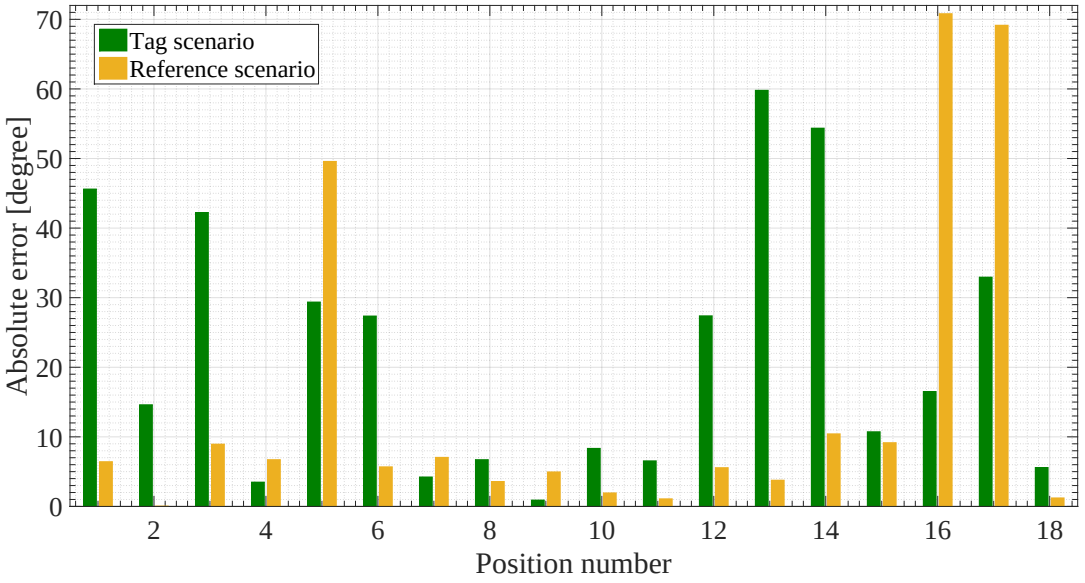

FIGURE 3.21: Localization results of the SD–PDoA based approach for the LoS scenario.

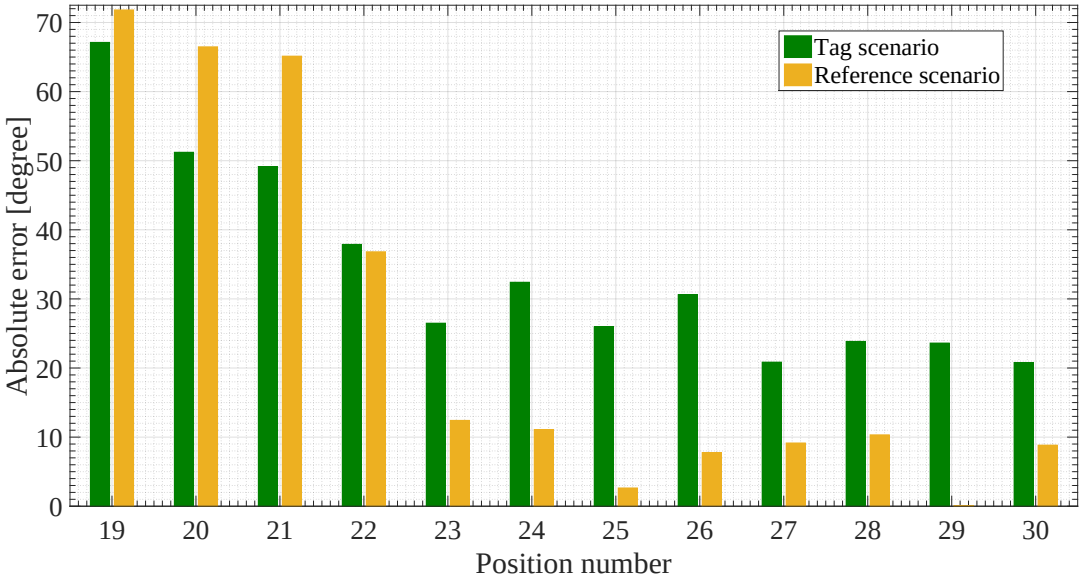

FIGURE 3.22: Localization results of the SD–PDoA based approach for the NLoS scenario.

3.3 Analyzer Implementation for Range Estimation

The concept of FD–PDoA explained in section 1.5.2 is implemented in the system analyzer of Figure 3.23. Basically, in order to incorporate the dual frequency FD–PDoA technique, the 4-port S-parameter block of Section 3.2 is broken into two 2-port S-parameter blocks. The backscatter channel (transmitter to the tag and back to the reader receiver) has been broken into the forward link and the reverse link. The final calculation of the estimated range is done in the "Range Estimation Block," which is in the middle of the topology in Figure 3.23. The blocks on the left hand side (LHS) of the "Range Estimation Block" are operating at frequency f_1, whereas the blocks on the right hand side (RHS) of the "Range Estimation Block" are operating at frequency f_2. Therefore, two topological same systems are operating simultaneously, at two different carrier frequencies. By this, the FD–PDoA based system analyzer is modeled as per the schematic diagram in Figure 1.8.

The port configurations of the S-parameter blocks in the FD–PDoA based system analyzer are kept the same as of the AVL measurement campaign, i.e., the RFID transmit antenna is connected to port1, the tag antenna is connected to port4, RX1 antenna to port2 and RX2 antenna is connected to port3 of the VNA. The S-parameters of a particular position of the tag are plugged in the S-parameter block in SimRF$^{\text{TM}}$.

Both of the LHS and RHS blocks operate at two different carrier frequencies, i.e., f_1 and f_2. In each of the two halves, we start with a CW block. This block sends out the continuous waveform operating at the frequency f_i, where $i = 1, 2$. The initial phase of the CW signal is 0°. After passing through the amplifier section, the CW signal is fed to the port1 of the S-parameter block "TX to Tag Channel@f1" in the LHS and "TX to Tag Channel@f2" in the RHS half of the system simulator.

The blocks "TX to Tag Channel@f1" and "TX to Tag Channel@f2" emulate the real forward channel from the two RFID transmitters (operating at frequencies f_1 and f_2) to the RFID Tag. Specifically, the block "TXtoTagChannel@f$_i$" ($i = 1, 2$) uses the $S_{\text{TX-Tag}} = \begin{pmatrix} S_{11} & S_{14} \\ S_{41} & S_{44} \end{pmatrix}$ matrix, emulating the channel from the transmitter to the tag at frequency f_i, between ports 1 and 4 of the VNA during the measurement campaign. After passing through the S-parameter blocks of both frequencies f_1 and f_2, the CW is fed to the RFID tag. The tag subsystem is capable of handling realistic modulations states. After the tag, the signal is backscattered towards the RFID reader receiver, from

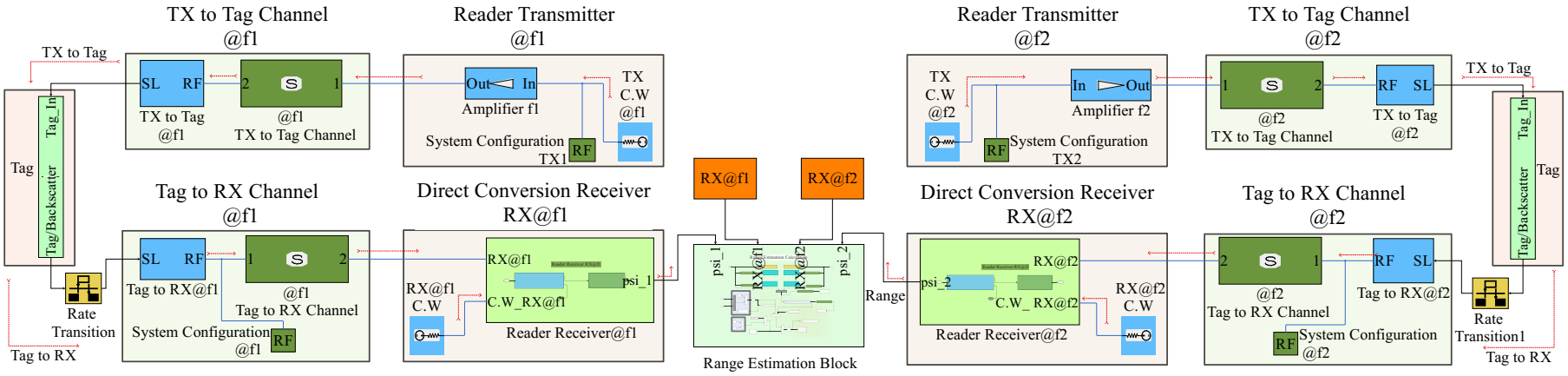

FIGURE 3.23: FD–PDoA based system simulator for range estimation. In the middle of the topology is the "Range Estimation Block", which is doing the final calculations for the range estimation. The topology can be divided in to two halves on either side of this block. The left hand side is operating at frequency f_1 and right hand side is operating at the other frequency f_2. The solid blue line depicts connections in SimRF whereas black lines are normal Simulink connections of blocks. The signal flow in each of the halves starts from the continuous wave block. After passing through the "TX to Tag Channel" (in both of the halves), the waveforms are fed to same copies of an RFID tag. Then on the reverse link, the CW undergoes another change in phase after passing through the "Tag to RX Channel." Then after down conversion, the phases ψ_1 and ψ_2 are fed to the "Range Estimation Block."

both of the two blocks operating at frequencies f_1 and f_2. The output of the tags of the LHS and RHS systems are fed into the reverse channel of the respective operating frequencies, i.e., to the S-parameter blocks named "Tag to RX Channel@f1" and "Tag to RX Channel@f2," respectively. The arguments to these block are the S-parameters $S_{\text{Tag}-\text{RX1}} = \left(\begin{smallmatrix} S_{44} & S_{42} \\ S_{24} & S_{22} \end{smallmatrix}\right)$, if RX1 is used as the receive antenna and $S_{\text{Tag}-\text{RX2}} = \left(\begin{smallmatrix} S_{44} & S_{43} \\ S_{34} & S_{33} \end{smallmatrix}\right)$, if RX2 antenna is used as the receive antenna.

Each of the reader receivers block consists of a downconversion block implemented in SimRF™. The RF signals are coherently downconverted in both reader receiver blocks. The complex valued downconverted signals from both reader receivers are fed to the leakage cancellation blocks. After this, the tag signals operating at f_1 and f_2 are extracted to calculate the phases, i.e, ψ_1 and ψ_2 using the respective IQ values [135].

After extracting the phases ψ_1 and ψ_2 of the signals (operating at carrier frequencies f_1 and f_2, respectively), the range calculations are done in the middle block named "Range Estimation Block." This block is basically the implementation of equation 1.30.

The main purpose of the SIMO configuration is to get the DoA estimation based on the SD-PDoA technique. However, this antenna configuration is also helpful in better range estimation. The range estimation system analyzer works the same for both of the two backscatter links, i.e., TX–Tag–RX1 and TX–Tag–RX2. As the largest room dimension is a known parameter, after getting the range results for both of the backscatter links, clear outliers are shunted out. Like there can be a deep fade over one of the two backscatter links (either to RX1 or RX2). In this case, the wrong range estimate can be ignored. In this way, the SIMO configuration helps in getting trustworthy range results in such a severe multipath environment.

3.3.1 Range Validation

In order to get the value of range error introduced due to the phase irregularities as per equation 1.27, the measured CTFs (S-parameters) in the anechoic chamber for the DoA validation are incorporated in the range estimation system analyzer of Figure 3.23. As a SIMO configuration is employed for the AVL measurement campaign, the CW passes through the TX antenna to the custom-built tag antenna and then back to both RX1 and RX2 antennas. Therefore, the CW suffers from phase irregularity twice in the Motorola AN480 and twice in the custom-built patch antennas. The two Motorola

AN480 antennas were used as transmitter and receiver in the anechoic chamber and the S-parameters were measured. The actual distances with the estimated distances were compared and an offset of 2.68 m was found. Similarly, same measurements were performed using using two custom-built patch antennas as shown in Figure 3.24. The offset found for these patch antennas was 2.4 m. In totality, the offset error due to the entire SIMO configuration becomes 5.08 m. This is the calculated offset coming due to the phase irregularities as mentioned in equation 1.27 [97].

Figure 3.25 depicts the vulnerability of the concept of FD–PDoA based range estimation. Even the slightest of the phase variations can deviate the range results to a large extent. An average offset of 1.2 m exists between the geometric and simulated estimates of Figure 3.25. The corresponding phase difference for this offset is 14.4°. The offset between the geometric ranges and estimated range values is attributed to the nonlinear phase behavior of the custom-built patch antennas. On the other hand, the Motorola antennas have a quite linear phase response over the measured frequency range. The validation will be handy to compare the range estimation results of the AVL measurement campaign in the engine test bed facility.

3.3.2 Range Performance Analysis

The range estimation results of the system analyzer are shown in Figure 3.26 for the LoS case and in Figure 3.27 for the NLoS case. For the LoS case in the Reference scenario, the closest to the geometric range values are the estimated values for the case of 880 MHz–890 MHz pair based simulated range (> markers). There are few outliers for this case, like at $p2$, $p4$, and $p12$. In comparison the other frequency pair based range estimates for the Reference scenario for the LoS case, i.e., for the 890 MHz–900 MHz frequency pair, the results are deviating quite far away from the respective geometric range values for $p1$, $p2$, $p3$, $p4$, $p5$, and $p10$.

In the Tag scenario, the 880 MHz–890 MHz frequency pair based results improve as we get closer to RX1 and RX2, i.e., for $p8$–$p18$. It can be observed, that $p1$–$p4$ can not be realy termed as LoS positions, as the large engine test bench (Figure 2.4) is obstructing the direct path communication between the tag antenna to both of the RX1 and RX2. Therefore, given the fact that for narrowband ranging techniques we require a strong LoS path between the tag and the reader for accurate range results, these results for the LoS case for both of the Reference and the Tag scenario are not the unexpected ones.

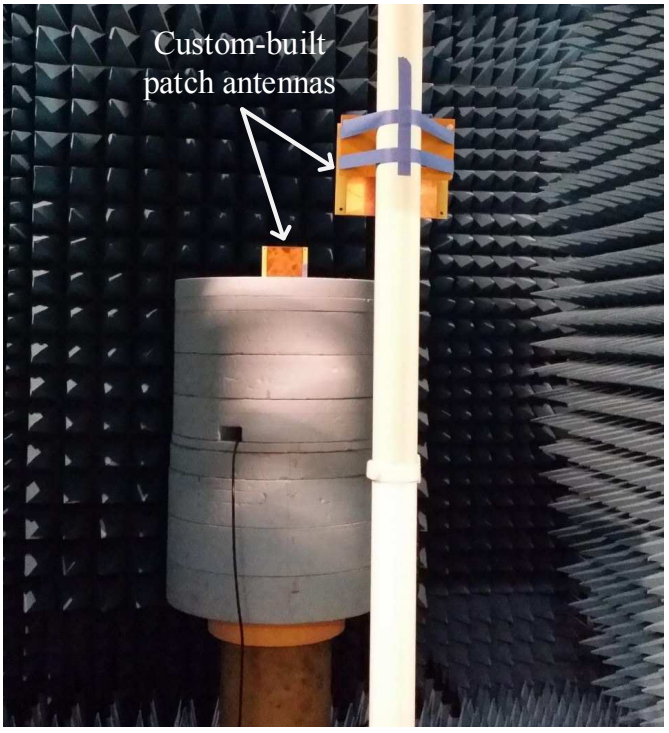

FIGURE 3.24: Anechoic chamber measurements for estimating the range offset introduced due to the custom-built patch antennas.

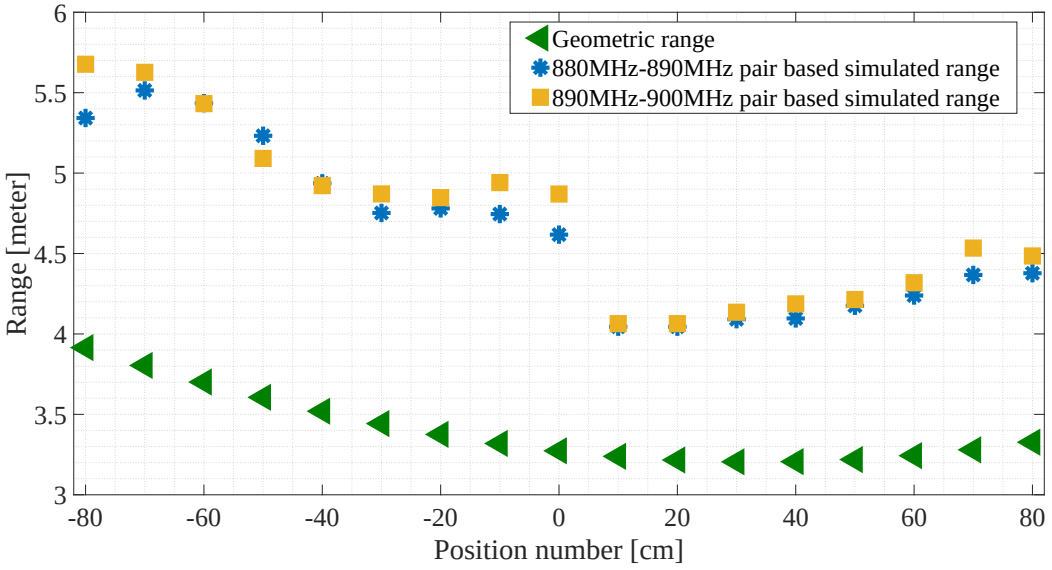

FIGURE 3.25: Validation of the system simulator for the range estimation in the anechoic chamber.

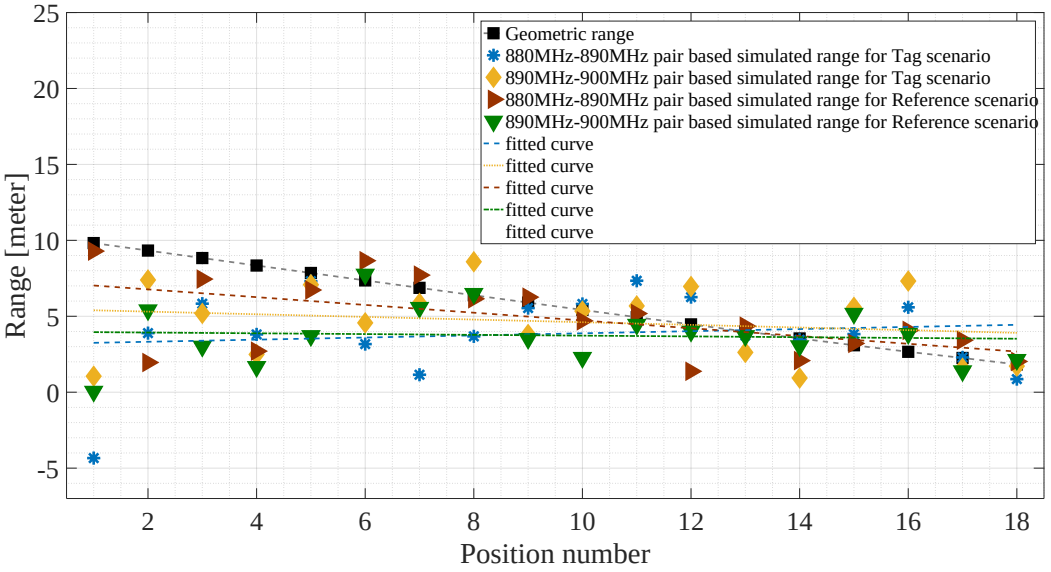

FIGURE 3.26: Range estimation results of the FD–PDoA based approach for the LoS scenario: The dashed-grey line (with ■ markers) is showing the geometric range values. The blue and mustard colored lines (with $*$ and $\Diamond$ markers) are the results for the Tag scenario. Whereas the red and green colored lines (with $>$ and ∇ markers) are showing the results for the Reference scenario.

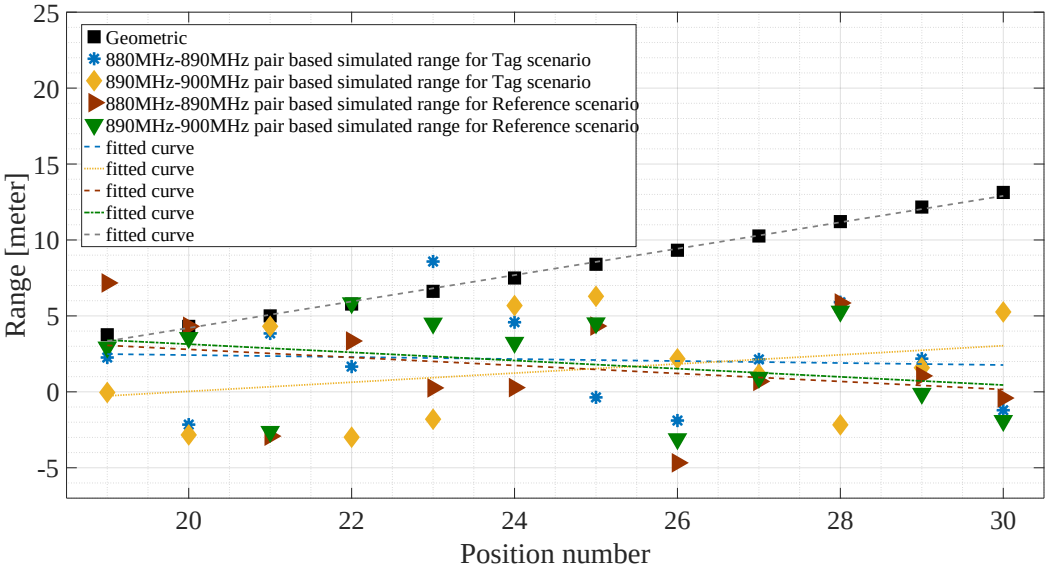

FIGURE 3.27: Range estimation results of the FD–PDoA based approach for the non-line of sight scenario.

TABLE 3.2: Root mean square error of the range estimation for both of the reference and tag scenarios.

	Tag Scenario (meter)		Reference Scenario (meter)	
	880MHz-890MHz	890MHz-900MHz	880MHz-890MHz	890MHz-900MHz
LoS	2.8	2.5	1.5	2.4
NLoS	6.3	6.7	7.1	6.2

For the NLoS case in Figure 3.27, the estimated range values are not satisfactory at all for any of the frequency pairs, in both of the Tag and the Reference scenarios.

In order to have a better view of the magnitude of the error values at respective positions, I have plotted the absolute error values at respective positions in Figure 3.28 for the LoS case and Figure 3.29 for the NLoS case. We can see considerable error spikes for $p1$ till $p4$, as mentioned these positions are not truly LoS ones. For $p5$ till $p18$, reasonable results are achieved as majority of the absolute error values are less then 3 m. The LoS component becomes stronger as the distance between the tag and reader receiver antennas is decreasing. Hence, we are able to achieve a coarse-grained range estimation in the severe multipath environment with the given narrowband setup. Looking at Figure 3.29 for the NLoS case, the large spikes for majority of the NLoS positions (for both of the Tag and the Reference scenarios!) rule out the possibility of accurate localization using this technique in such a severe multipath environment.

As for the case of SD-PDoA, the RMSE values for the range estimates are calculated using the relation

$$\mathrm{RMSE}(\hat{R}) = \sqrt{\frac{1}{N_p}\sum_{p=1}^{N_\mathrm{p}}\Big(|R_\mathrm{geo} - R_\mathrm{sim}|^2\Big)}, \tag{3.7}$$

where N_p is the number of tag positions, i.e. 18 for the LoS and 12 for NLoS case., R_geo is the geometrical range and R_sim is the simulated range. Examining the values in Table 3.2, on average both of the Reference and the Tag sceanrio are giving similar results. The exception is the case of 880 MHz–890 MHz in the Reference scenario, which gives a bit of improvement from the respective case in the Tag scenario.

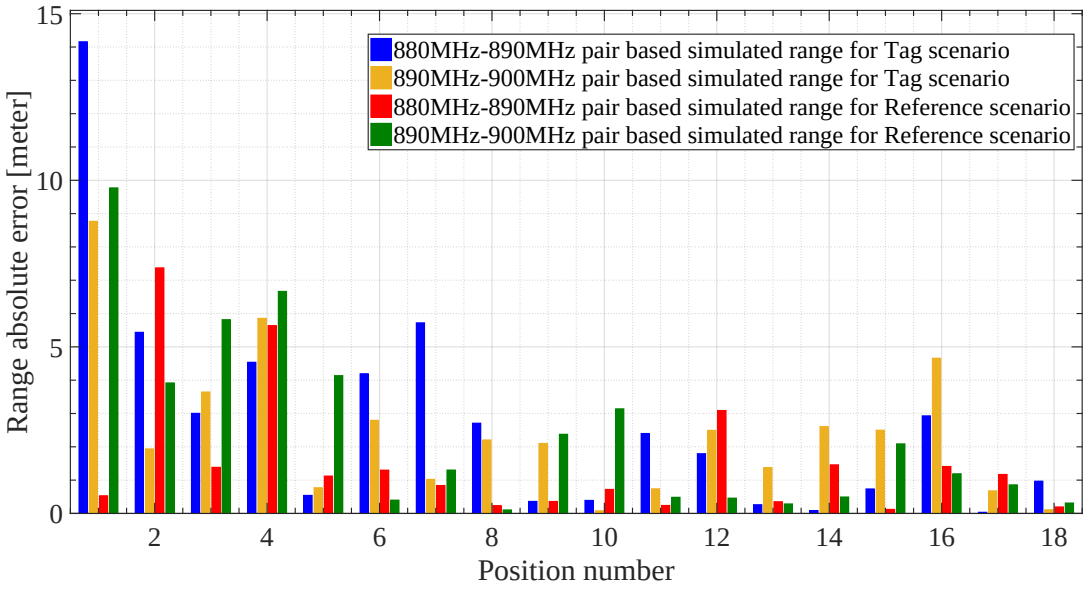

FIGURE 3.28: Localization results of the FD–PDoA based approach for the LoS scenario.

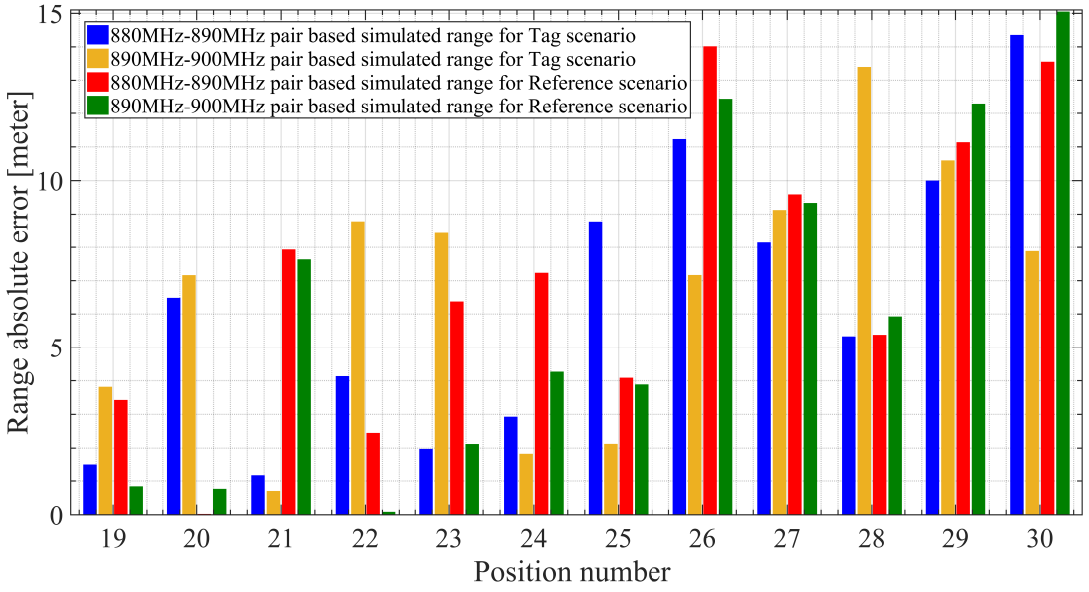

FIGURE 3.29: Localization results of the FD–PDoA based approach for the non-line of sight scenario.

3.4 Summary

In this chapter, I presented the system design of a measurement based system analyzer for the DoA and the range estimation of an RFID tag. I utilized the channel measurements of chapter 2 in the system analyzer to analyze the localization performance of a prospective narrowband RFID system. I have presented two different topological designs of the system analyzer for both of the two applications (DoA and range estimation). The analyzer implementations are based on the concepts of SD–PDoA and FD–PDoA, for the DoA and the range estimation, respectively. The DoA and the range estimation results were also discussed.

Chapter 4

Multifrequency Based RFID Tag Range Estimation

In this chapter, I will extend the utilization of the system analyzer of Figure 3.23 to probe the theoretical concept of CRT [136] based MF–PDoA approach for the range estimation. [137] suggests the theory behind this and discusses computer generated numerical results. The concept is also explained through simulations and experimental work in [138], but the simulations are computer generated and it does not utilize true RF signals in the simulations.

As explained in chapter 3.3, the system analyzer is based on real channel measurements and utilizes true RF simulation frequencies in the range of typical UHF RFID systems. The results of section 3.3 for the narrowband UHF RFID setup employed were not that satisfactory, mainly due to the severe multipath environment inside the AVL engine test bed. In MF–PDoA, more than two frequencies are chosen, either equally spaced or otherwise. For the case of unequal frequency separation between two adjacent frequency pairs, the ingenious selection of different frequency pairs based on the CRT approach for phase unwrapping [139] can enhance the range estimation accuracy.

4.1 MF–PDoA Theory

RFID systems normally have a finite tag range. Therefore, adequate frequency separation can be chosen to counter the unambiguous range estimation problem. Inferring from equation 1.31, we require a small frequency separation (Δf_{12}) for a large maximum unambiguous range. A direct consequence of this will be an amplification in the sensitivity of the phase difference measurements to noise. Concluding this, the deciding factors for selecting a frequency separation are a large maximum unambiguous range and a low sensitivity of the phase difference to noise.

Apart from the above two constraints, the signals might fade at one or both of the two carrier frequencies in the dual frequency FD-PDoA technique. Consequently yielding an unreliable phase and jeopardizing the range estimation results. Employing MF–PDoA approach helps in overcoming the aforementioned issues and improves the range estimation results [98].

In an MF–PDoA based RFID system, transmission of CW signals operating at M frequencies $(f_1, f_2, ...f_M)$ takes place from the RFID transmitter towards the RFID tag. The underlining assumption is that the frequencies are in an increasing order, i.e.,

$$f_1 < f_2 < f_3 ... < f_M. \tag{4.1}$$

Like the case of dual frequency FD-PDoA, we can represent the transmitted signal as

$$x(t) = \exp\left(j2\pi \sum_{i=1}^{M} f_i t\right). \tag{4.2}$$

The received backscattered signal from the RFID tag will be downconverted coherently using M mixers corresponding to the M carrier frequencies and subsequently demodulated separately. In effect, there will be M separate signals. Similar to equation 1.23, the output signal at the RFID reader receiver will be like

$$y_i(t) = h\,\delta(t)\,\exp(-j\psi_i),\ i = 1, 2, ..., M, \tag{4.3}$$

where ψ_i is of the form

$$\psi_i = \frac{4\pi f_i R}{c},\ i = 1, 2, ..., M, \tag{4.4}$$

as expressed in equations 1.28 and 1.29 for the dual frequency FD-PDoA case.. The range is estimated out of the received signal by using a frequency pair of f_i and f_j. In this case $f_i < f_j$ for any of $i, j = 1, 2, 3, ..., M$. Therefore the range estimate can be written as

$$\hat{R} = \frac{c(\Delta\psi_{ij})}{4\pi(\Delta f_{ij})}, \tag{4.5}$$

where $\Delta\psi_{ij} = \psi_j - \psi_i$ and $\Delta f_{ij} = f_j - f_i$ are the observed phase difference and the frequency difference, respectively. Using these M carrier frequencies, we can obtain $N = M(M-1)/2$ number of frequency range estimates [80]. Subsequently, we can fuse these N range estimates to combat noise and selective propagation characteristics.

There are two methods by which this MF–PDoA technique can be employed,

1. Equal frequency separation between adjacent frequency pairs,
2. Unequal frequency separation between adjacent frequency pairs.

For the first case, the frequency spacing between adjacent pairs is

$$\Delta f_{i,i+1}\ i = 1, 2, ..., M-1. \tag{4.6}$$

Consequently, the maximum separation between the highest and lowest frequencies is

$$\Delta F = (M-1)\Delta f. \tag{4.7}$$

The maximum unambiguous range in this case can be modeled as

$$R_{\max} = \frac{c}{2\Delta f} = \frac{(M-1)c}{2\Delta F}. \tag{4.8}$$

In the second case, CRT based unequal frequency separation helps in striking a balance between lowering of the noise sensitivity and maintaining a reasonable maximum unambiguous range. Another advantage of using this CRT based MF–PDoA technique is that it enables us to enhance the maximum unambiguous range.The following elaboration of the theory of MF–PDoA is based on the work proposed in [137]. Considering the k-th frequency pair, i.e.,

$$\Delta f_k = f_{k+1} - f_k, \tag{4.9}$$

where $k = 1, 2, ..., M-1$, a wrapped phase difference of

$$\Delta\psi_k = \psi_{k+1} - \psi_k, \tag{4.10}$$

is observed. Therefore, equation 1.33 can be modeled as

$$R = \frac{c(\Delta\psi_k)}{4\pi(\Delta f_k)} + \frac{cm_k}{2(\Delta f_k)} = \frac{v_k\Delta\psi_k}{4\pi} + \frac{m_k v_k}{2}, \tag{4.11}$$

where $v_k = c/\Delta f_k$. Supposing a constant D_0 (which represents a specific range bin), we can express v_k as a multiple of this constant D_0, i.e., $v_k = \xi D_0$, where ξ_k is a non-negative integer. Rewriting equation 4.11

$$\Delta\psi_k = \frac{2\pi}{\xi_k}\left(\frac{2R}{D_0} - m_k\xi_k\right). \tag{4.12}$$

The maximum unambiguous range in this case becomes

$$R_{\max} = \frac{D_0}{2}\mathrm{LCD}\left(\xi_1, \xi_2, ..., \xi_{M-1}\right), \tag{4.13}$$

where LCD(.) is the least common denominator operator. Additionally, defining the minimum distance between two adjacent ambiguous tag range estimates as

$$D_{\min} = \frac{D_0}{2}\mathrm{GCD}\left(\xi_1, ..., \xi_{M-1}\right), \tag{4.14}$$

where GCD(.) is the greatest common divisor. If we choose ξ_k's as coprimes, $R_{\max}$ is maximized as

$$\bar{R}_{\max} = \frac{D_0}{2}\prod_{k=1}^{M-1}\xi_k, \tag{4.15}$$

and $D_{\min}$ is reduced to

$$D_{\min} = \frac{D_0}{2}. \tag{4.16}$$

Among the five fusion methods reported in [137], I have estimated the range estimates using

$$\hat{R} = \frac{c}{4\pi}\frac{\sum\limits_{i<j}\Delta\psi_{ij}}{\sum\limits_{i<j}\Delta f_{ij}}. \tag{4.17}$$

In order to validate the concept, the measurement data of the anechoic chamber measurement campaign of section 3.3.1 is utilized. The selected frequency pairs (for the

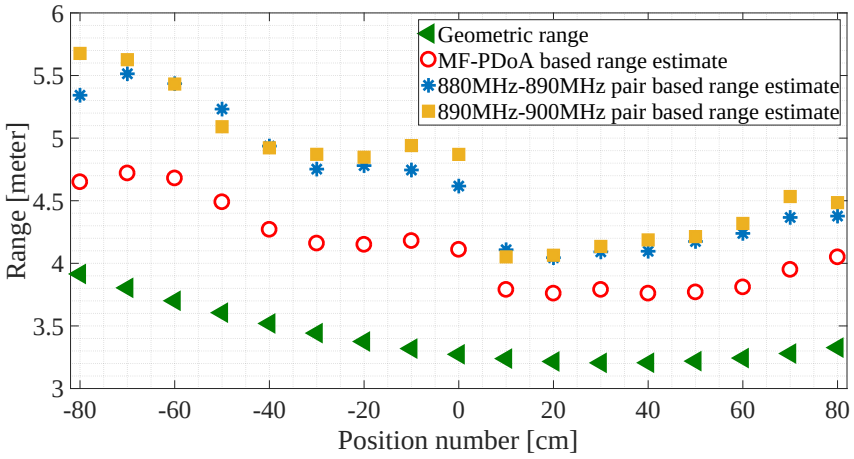

FIGURE 4.1: Validation of the MF–PDoA based range estimation in the anechoic chamber.

equal frequency separation based MF–PDoA) for the anechoic chamber measurements are

1. 872 MHz–881 MHz
2. 881 MHz–890 MHz
3. 890 MHz–899 MHz
4. 899 MHz–908 MHz.

I have utilized the equal frequency separation between adjacent frequency pairs. There is a definite improvement in the range estimation by utilizing the MF–PDoA approach for range estimation, as depicted in Figure 4.1.

4.2 Measurement Setup

Another channel measurement campaign was performed in a realistic indoor multipath environment, conducted in the Microwave laboratory at the Institute of Microwave and Photonic Engineering (Institut für Hochfrequenztechnik, IHF), Graz University of Technology.

Figure 4.2 depicts the IHF Microwave laboratory environment, exhibiting a multipath scenario. A four-port VNA from Rohde & Schwarz was utilized to measure the channel CTFs (S-parameters). The reader antennas and the tag antenna are connected to the

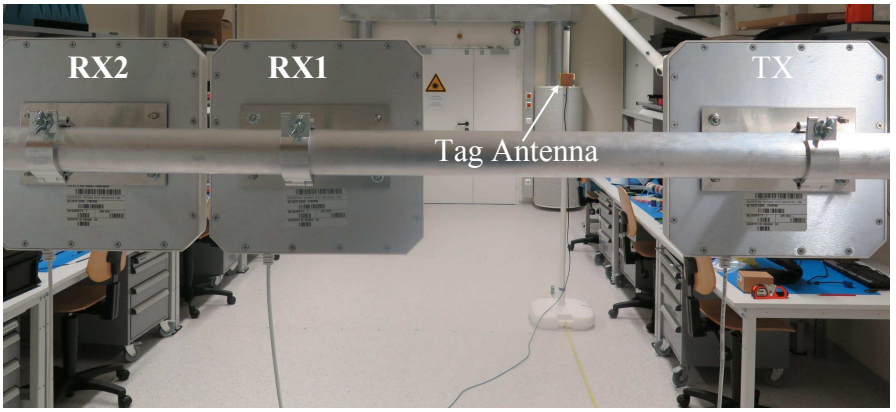

FIGURE 4.2: The IHF lab environment. There is plenty of steel structures, hence giving rise to a severe multipath propagation environment.

FIGURE 4.3: The antenna setup for the measurements. The measurement reference plane is at the input of the antennas. The origin is taken in the middle of RX1 and RX2 antennas. The gap between RX1 and RX2 is kept 27 cm. The distance between the TX and RX2 is 55 cm. The tag antenna was surmounted on a mobile fixture, so that it can be positioned freely in the IHF lab. The VNA generates continuous sinusoidal waves (without modulation) for the channel measurements. The frequency sweep range is from 600 MHz to 1.2 GHz.

VNA using 50 Ω coaxial cables, as shown in Figure 4.3. The VNA port connections are the same as those of the AVL measurement campaign, as listed in Table 2.2. We employed a SIMO antenna configuration, i.e., one transmitter (TX) antenna and two reader receiver antennas (RX1 and RX2), as shown in Figure 4.3. The transmitter and reader antennas are Motorola AN480 [122] patch antennas and the tag antennas are the same as used in the AVL measurements campaign. The antenna matching at the respective frequencies was below -10 dB.

Figure 4.4 is depicting the measurement floor plan in the microwave lab. The TX, RX1 and RX2 antennas were placed in one line along the x-axis, adjacent to each other. The tag antenna is at the same height as of the TX, RX1 and RX2 antennas. The CTFs were measured versus frequency at 14 tag antenna positions at each of the 9 trails. At each tag antenna position, the CTF measurement versus frequency is repeated 20 times for spatial averaging [121]. Figure 4.4 also depicts some obstacles like measurement desks, steel boxes, microwave equipment etc.

As the antenna setup depicted in Figure 4.3 is the same which was used in the AVL measurement campaign, the same range-offset calculated in section 3.3.1 will be used here as well, i.e., an offset of 5.08 m.

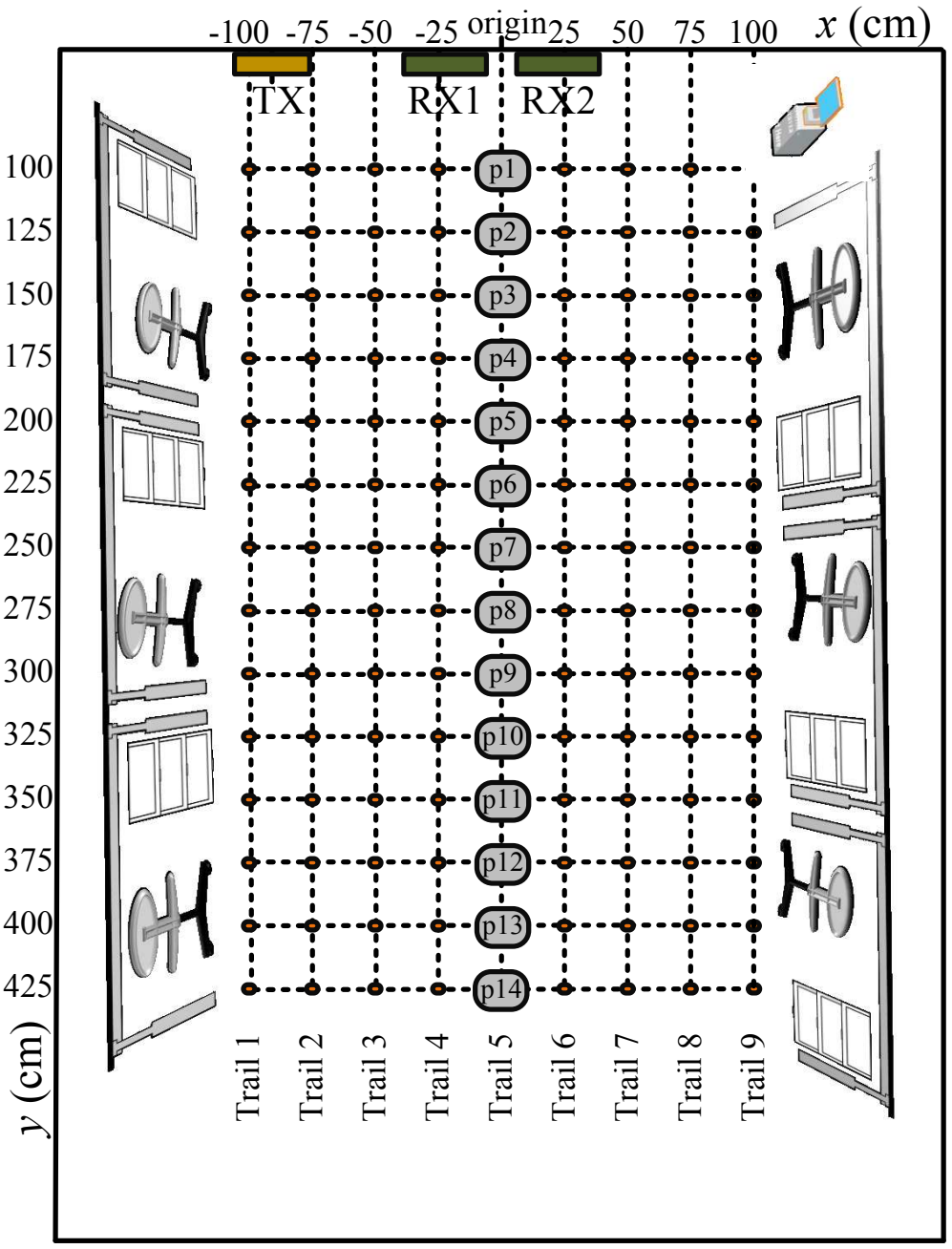

FIGURE 4.4: Measurement floor plan. The measurement area is divided into nine trails along the y-axis, with trail 5 being in the middle of RX1 and RX2 antennas. The spacing between two adjacent trails is kept 25 cm. The tag is placed at 14 positions at each of the nine trails, with the first position ($p1$) is at a distance of 100 cm from the antennas. The spacing between any two positions on a particular trail is kept 25 cm.

4.3 Performance Analysis

For the case of CRT based unequally spaced frequency separation, we can summarize the algorithm presented in [137] as

i. Select a starting frequency, i.e., f_1

ii. Select M number of different frequencies and the total frequency separation of ΔF, i.e., $f_M - f_1$

iii. Select the coprime numbers ξ_k's

iv. Choose an appropriate value of D_o (can be variable for unequal frequency separation case)

v. Calculate $R_{\max,k} = \xi_k D_o/2$

vi. With $R_{\max,k}$ calculated in the previous step, find the value of $\Delta f_{k,k+1}$ using the relationship $\Delta f_{k,k+1} = c/2R_{\max,k}$

vii. Using f_1 and the other Δf_k's, find the remaining $(M-1)$ frequencies

Starting with a frequency of $f_1 = 874\,\text{MHz}$, the chosen coprimes and the resulting values are listed in listed in Table 4.1. Finally, the remaining carrier frequencies for our case of the CRT based (unequal frequency separation) MF–PDoA are $f_2 = 880\,\text{MHz}$, $f_3 = 890\,\text{MHz}$, $f_4 = 895\,\text{MHz}$ and $f_5 = 904\,\text{MHz}$. The maximum unambiguous range $R_{\max,k}$ for all of the four pairs is well above the geometrical ranges of our measurement scenario in the IHF Microwave laboratory.

For the comparative analysis of the CRT based approach to that of the single frequency pair based range estimation, I have chosen two single frequency pairs constituting the equal frequency separation case. The two pairs are of $f_1 = 880\,\text{MHz}$, $f_2 = 890\,\text{MHz}$ and $f_1 = 890\,\text{MHz}$, $f_2 = 900\,\text{MHz}$, respectively.

For the case of CRT based MF–PDoA range estimation, I have used the carrier frequencies calculated in the preceding paragraph. Figure 4.5 depicts the range estimation results for the three cases.

It can be observed that on average, CRT based MF–PDoA range estimation results are better than the two single frequency pairs base range estimation results. For almost

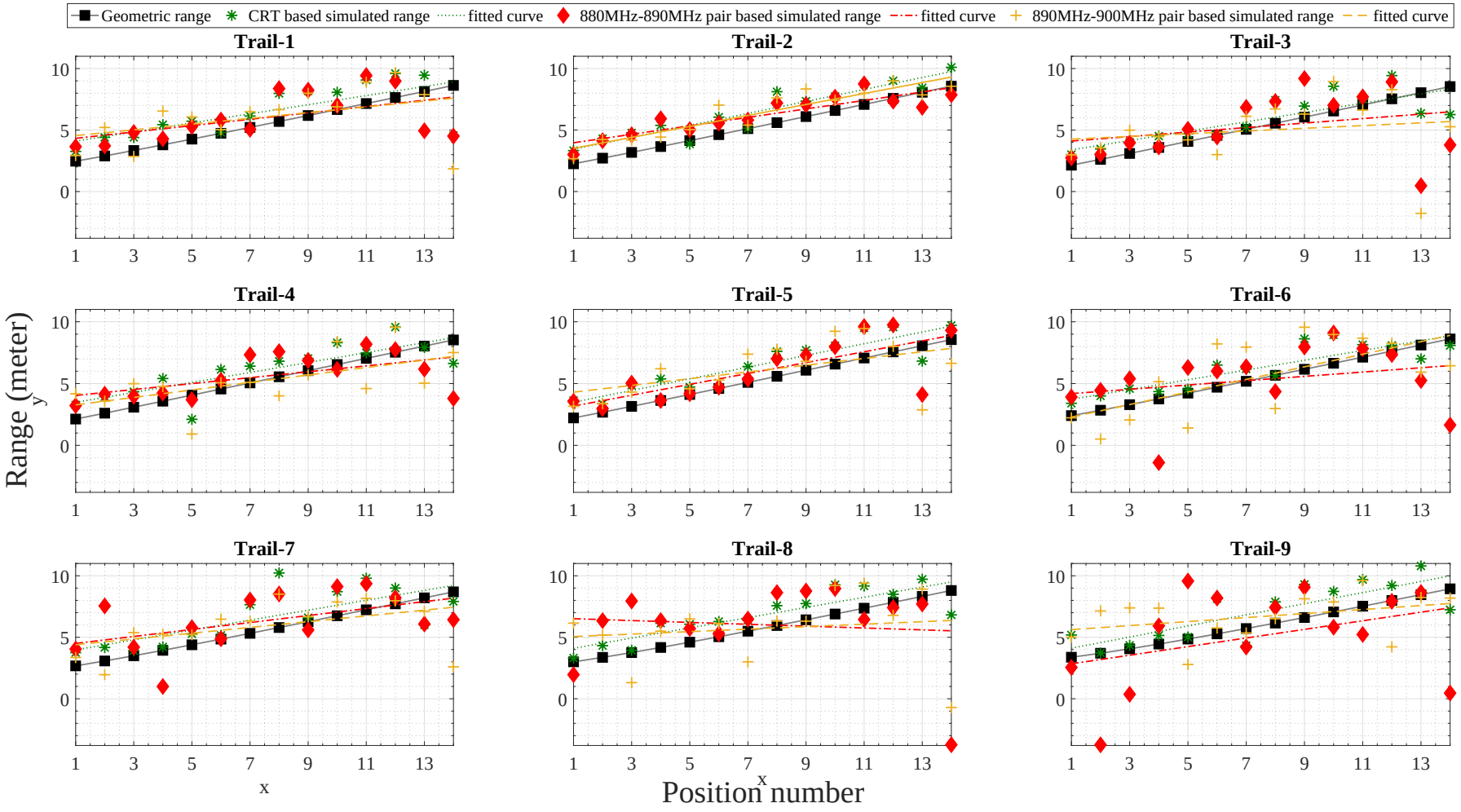

FIGURE 4.5: Curve fit results of polynomial fit of degree 1. The CRT based results are shown in green (dotted), where as the two cases of dual frequency FD-PDoA based estimates are shown in red (dashed-dotted) and mustard (dashed). The first single frequency pair is of $f_2 = 880\,\text{MHz}$, $f_3 = 890\,\text{MHz}$, whereas the second frequency pair is of $f_2 = 890\,\text{MHz}$, $f_3 = 900\,\text{MHz}$.

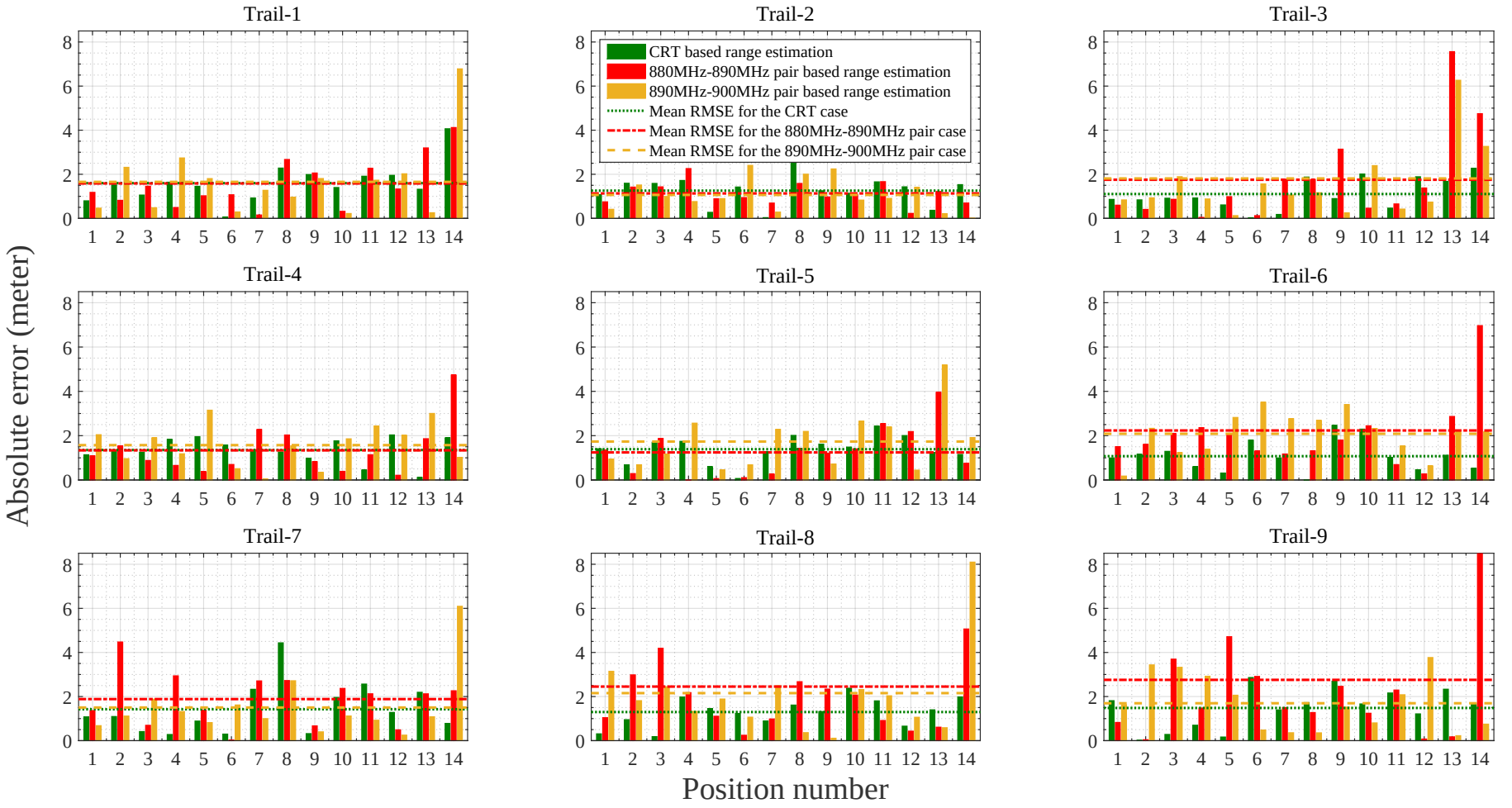

FIGURE 4.6: Absolute error plots for the three cases of CRT based, 880MHz – 890MHz pair and the 890MHz – 900MHz pair. The horizontal lines are the average RMSE values for each of the three cases.

TABLE 4.1: Coprime and D_o values for the calculation of $R_{\max,k}$'s for the case of CRT based unequal MF–PDoA.

k	ξ_k	$D_{o,k}$ (m)	$R_{\max,k}$ (m)	Δf_k (MHz)
1	5	10	25	6
2	3	10	15	10
3	4	15	30	5
4	7	4.76	17	9

all of the trails, the MF–PDoA based range estimates are maintaining a certain positive offset from the geometric ranges. This is more evident if we employ a polynomial fit of degree-1 to all of the estimated range results. In Figure 4.5, we observe no extreme deviation of the MF–PDoA based range estimates from the geometric line, especially for the farthest positions on each of the 9 trails. On the other hand, both the single frequency pair based range estimates are deviating a lot (below and above) from the respective geometric range values.

Another interesting behavior noted is that the MF–PDoA curves are never cutting the geometric line, remaining positively biased for all of the 9 trails. MF–PDoA gives us a reliable average range estimate rather than extremely deviated estimates. Looking position wise on each trail, up till position p4 in all of the trails 1–4 and 7, all three curves are very closely spaced. The possible reason could be that there is a strong LoS signal present in these cases. For the later positions on trails 1–4 and 7, the three curves are diverging from each other. For the case of Trail–1, both the single frequency pairs are giving the same performance as both the 880 MHz–890 MHz pair based and 890 MHz–900 MHz pair based lines are overlapping for all of the 14 positions. In comparison, the MF–PDoA curve in Trail–1 is giving a better performance, specially towards the end positions on Trail–1. The best result is of the Trail–6 as the 890 MHz-900 MHz pair based curve is almost overlapping the geometric curve for all of the 14 positions. For the trails 2, 3, 4 and 7, both the 880 MHz–890 MHz pair based and 890 MHz–900 MHz pair based lines lines are overlapping for at least half of the positions. Moreover, both of the single frequency pair based range estimate lines are not much deviating from each other for the rest of the positions on trail number 2, 3, 4 and 7. Drawing inference from this, the single frequency pair based range estimates are giving almost identical estimates for quite many positions. It can be concluded that the MF–PDoA based approach is more robust to multipath effects. It is understandable that with the given antenna setup we can only achieve coarse-grained localization of RFID

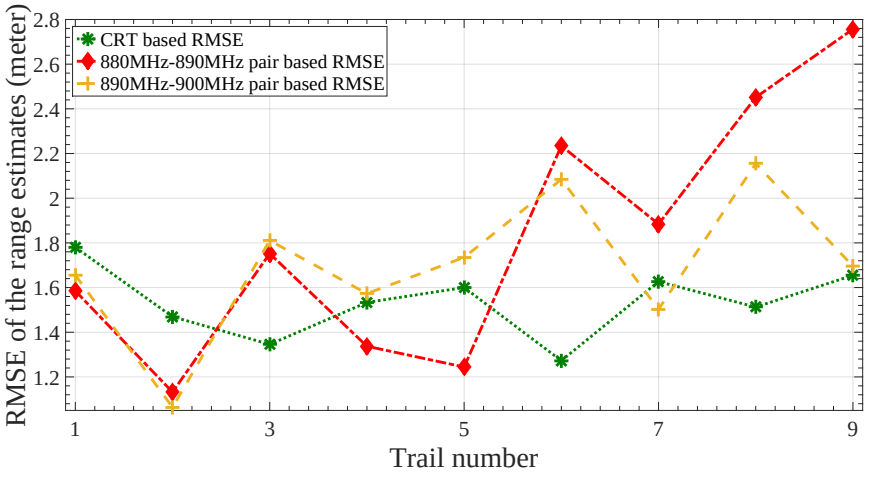

FIGURE 4.7: RMSE values for all of the 14 positions for the three cases of MF–PDoA based and the two single frequency pair based range estimates.

tagged objects. In this perspective, the MF–PDoA based lines in Figure 4.5 are giving a good enough range estimate of the RFID tag. To further elaborate the superiority of the MF–PDoA based approach, I refer to the absolute error plots in Figure 4.6. The single frequency pair based range estimates suffer badly at the farthest positions, i.e., $p13$ and $p14$, as the absolute error bar is having spikes for these positions. Except one spike for the Trail 8, on average all the CRT based MF–PDoA error values are smaller (or comparable) than the error values for the single frequency-pair based range results.

In order to get some reference value, I calculated the error values for the three range estimates. The RMSE is calculated by

$$\text{RMSE}(\hat{R}) = \sqrt{\frac{1}{N_p}\sum_{p=1}^{14}\left(|R_{\text{geo}} - R_{\text{sim}}|^2\right)}, \tag{4.18}$$

where $N_p = 14$ is the number of tag positions for each of our trails, R_{geo} is the geometrical range and R_{sim} is the simulated range. I computed the overall mean of RMSE for all of the 14 positions in the CRT based MF–PDoA and the single frequency pair based FD-PDoA cases. I have used these single mean RMSE values as a reference and plotted them as a reference value (dotted, dashed-dotted and dashed horizontal lines) in Figure 4.5. As the RMSE is an average value for all the 14 positions of any one of the trails, we observe that in the CRT based MF–PDoA case, the absolute error values are not going that high above the RMSE line in Figure 4.6. Comparatively, the error values of the single frequency-pair based results do have some high spikes in Figure 4.6.

The RMSE values for the cases of the CRT based MF–PDoA based and the two single frequency-pair based range estimation are plotted in Figure 4.7. It is evident that the RMSE values for the CRT based MF–PDoA technique are varying the least, thus giving more reliable and consistent range estimation.

As a final analysis, I applied the MF–PDoA based approach (equal frequency separation) to the measurement data of the AVL measurement campaign. The selected frequency pairs are 884 MHz–890 MHz and 890 MHz–896 MHz. By comparing Figure 3.26 with that of Figure 4.8, for the case of LoS for both of the Tag and the Reference scenarios, the negative bias of range estimation results is removed, i.e, in Figure 4.8 the estimated curves are not cuting through the geometric curve. Whereas, as expected from such a narrowband UHF RFID ranging setup, the performance in the NLoS scenario is still not that satisfactory, as shown in Figure 4.9.

4.4 Summary

Exploiting the benefits of the system analyzer developed in chapter 3, it has been shown in this chapter that the theoretical concept of CRT based MF–PDoA (for selecting the unequally spaced frequency pairs) is considered to provide better range estimation in multipath environments. For this, another measurement campaign was carried out in a lab environment with a lot of scatterers around. Both variants of MF–PDoA, i.e., equal separation pairs and the CRT based unequal frequency separation pairs, are explained and applied for the range estimation inside the IHF lab.

Later in the chapter, the equal frequency based approach is also applied to the AVL engine test bed channel data. It has been shown that the MF–PDoA based range estimation is giving better results than the single pair FD-PDoA approach.

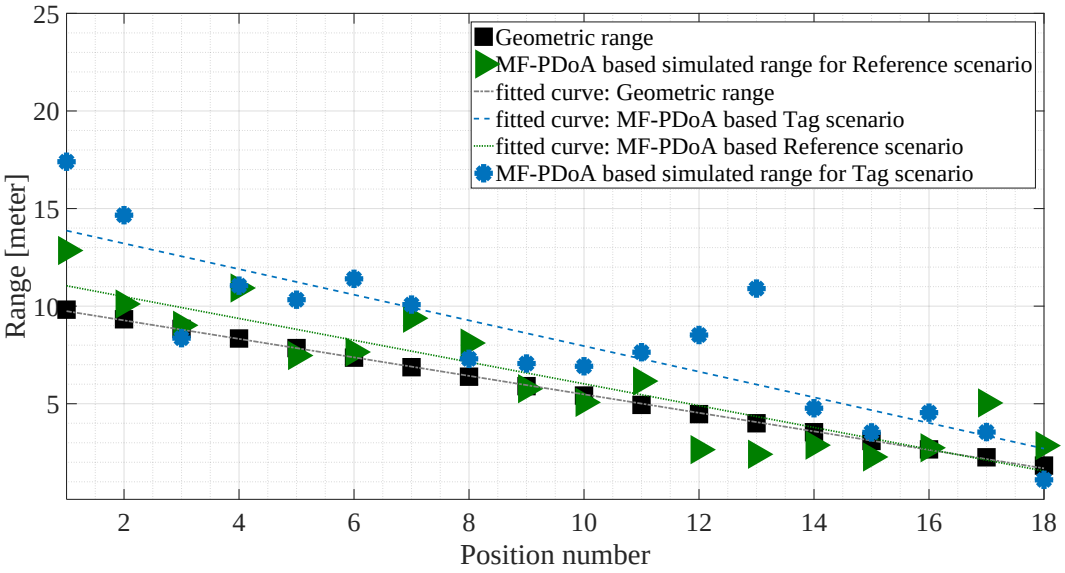

FIGURE 4.8: MF–PDoA based range estimation of the AVL channel measurement for the LoS scenario.

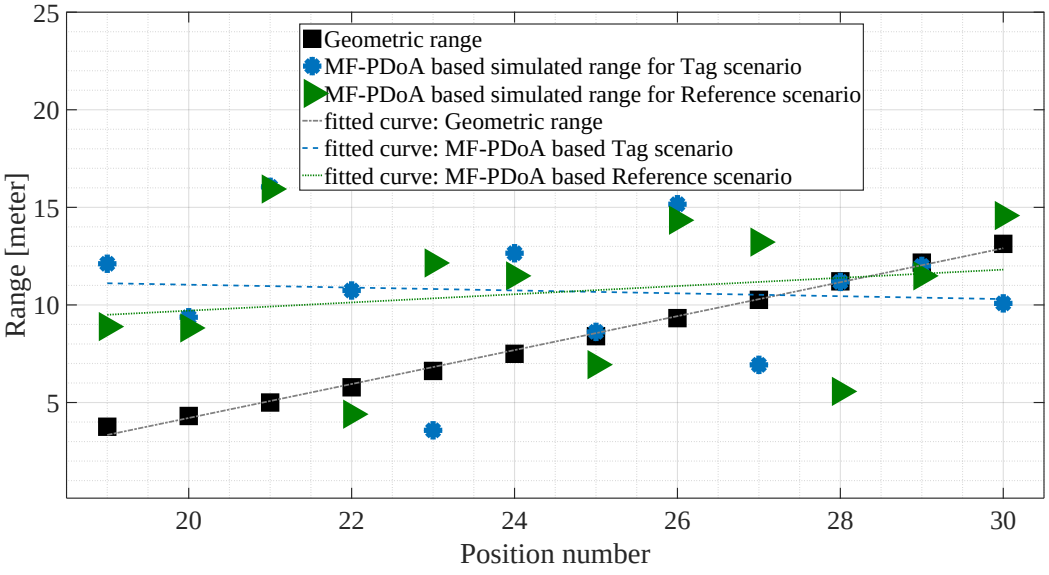

FIGURE 4.9: MF–PDoA based range estimation of the AVL channel measurement for the NLoS scenario.

Chapter 5

Conclusion and Future Research

5.1 Conclusion

In this research, I have presented a measurement based system analyzer which relies on physical channel measurements. The system analyzer is capable of performing coarse-grained two dimensional tag localization in a severe multipath-indoor environment. The system analyzer gives flexibility for system design, as I can plug in different real channel measurements and scale the analyzer in terms of the operating frequency, input power levels, etc. The RF components of the system analyzer are built using the SimRF™ toolbox of Simulink®. By this, unlike the previous simulation/emulation platforms, the presented system analyzer utilizes real channel measurements and is based on true RF signals. Moreover, there is a provision to incorporate real system nonlinearities in the system analyzer. By this, the system analyzer can be utilized to model the real hardware setups more accurately.

Wireless channel data from the measurement campaign (conducted at AVL, Graz) was utilized to test the feasibility of the algorithms of DoA estimation and range estimation. The RFID tag localization is achieved by estimating the range and the DoA of the RFID tag. I employed the SD–PDoA and FD–PDoA techniques for estimating the DoA and range of the tag, respectively. In the AVL channel, the analyzer gives near perfect DoA estimation at several tag positions where the LoS component is the dominant ray coming from both RX1 and RX2. Whereas the range estimation results are not that accurate. As predicted by theory and by previous research, with the narrowband setup,

the system analyzer's performance depicts that we can only have coarse-grained localization inside AVL engine test bed facility. Like if we divide the room into four halves, we can estimate the RFID tagged object into one of the four halves.

In general, different algorithms for RFID localization can be probed with this measurement based system analyzer. I tested the theoretical concept of CRT based MF–PDoA by utilizing the system analyzer in another multipath environment, i.e., the IHF lab at the Graz University of Technology. It has been shown that the CRT based MF–PDoA technique is more immune in severe multipath scenarios and gives better range estimation results in comparison to the case of single frequency pair based FD–PDoA approach.

As the system analyzer is a measurement based one, therefore giving realistic estimation results. In case one may not have an access to the hardware equipment utilized in this research, e.g., antennas, VNA etc., the channel data (S-parameters) can be generated via some microwave software, e.g., CST [140] and imported as touchstone file. This channel data then can be plugged into the system analyzer to estimate the DoA and the range or to develop new design topologies.

5.2 Future Research

The system analyzer developed in this research can be further extended by some more research in the following directions:

1. As for the case study of the AVL channel, the tag antenna was part of the channel measurements. But in some other scenarios, we may need to incorporate the RFID tag antenna nonlinearities, e.g., tag differential RCS (dRCS) and the backscatter phase as a function of the incident power, hence of the distance to the tag [72]. The dRCS (related to the modulation factor) changes linearly vs incident power but the phase does not. This is depicted in Figures 5.1 and 5.2, courtesy Honeywell Inc. [141]. A custom-built RFID reader, e.g., Tagformance™Pro [142] can be used to measure these nonlinearities for a particular tag. Plugging the tag antenna out of the channel measurements and re-adjusting the system analyzer topology, these nonlinear effects of the RFID tag antenna can be modeled in the system analyzer. By doing so, the RFID tag model presented in Figure 3.4 will be incorporated. Eventually, the system analyzer will become more realistic.

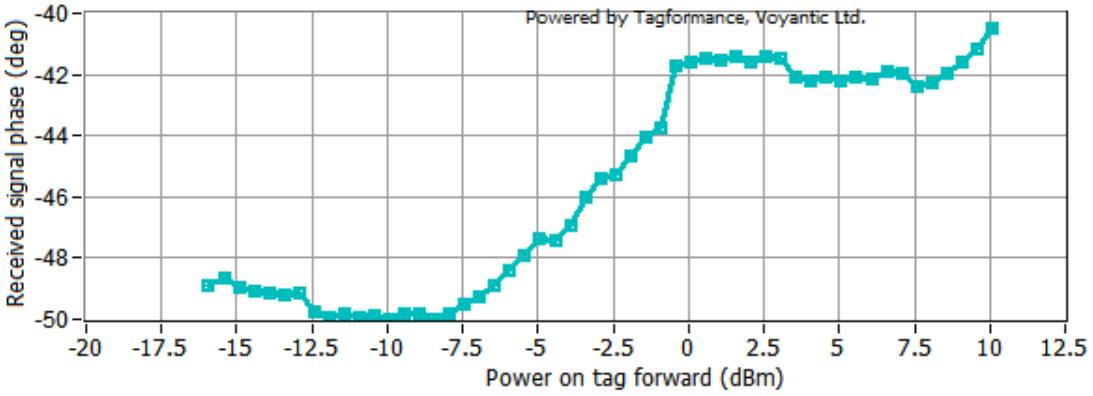

FIGURE 5.1: Received signal phase vs incident power on the tag over the forward channel. As it is evident that the phase varies non linearly with change in power (courtesy Honeywell Inc., USA).

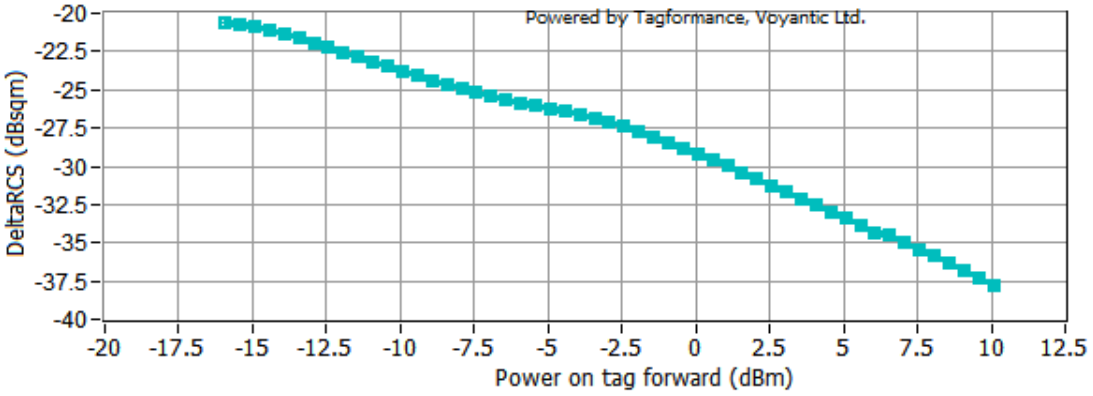

FIGURE 5.2: Differential radar cross section vs incident power over the forward channel. The dRCS varies almost linearly by change in power (courtesy Honeywell Inc., USA).

2. As a precise validation of the system analyzer with an RF tag model (as discussed in the previous point), the specific tag characteristics can be preloaded and the range and the DoA estimation can be achieved based on the channel measurements (S-parameters). Then measuring the received phases of the backscatter signals by using a measurement reader like Tagformance™ [142], the range and the DoA can be estimated. Eventually, comparing the results from the aforementioned methods will be a further validation of the system analyzer presented in this research.

3. In this work, I have designed the RFID tag based on pure ASK. As mentioned in chapter 1, a possible extension can be to implement some pulse shaping filter, again bringing the system analyzer close to a realistic system.

4. For the case of MF–PDoA based range estimation, the reader output power and phase changes as the reader hops (especially in the US band which has 52 subchannels in 26 MHz space) [143]. This can also be incorporated in the system design of my system analyzer for range estimation.

Appendix A

Power Delay Profiles for the Tag and the Reference Scenarios in the AVL Channel Measurement Campaign

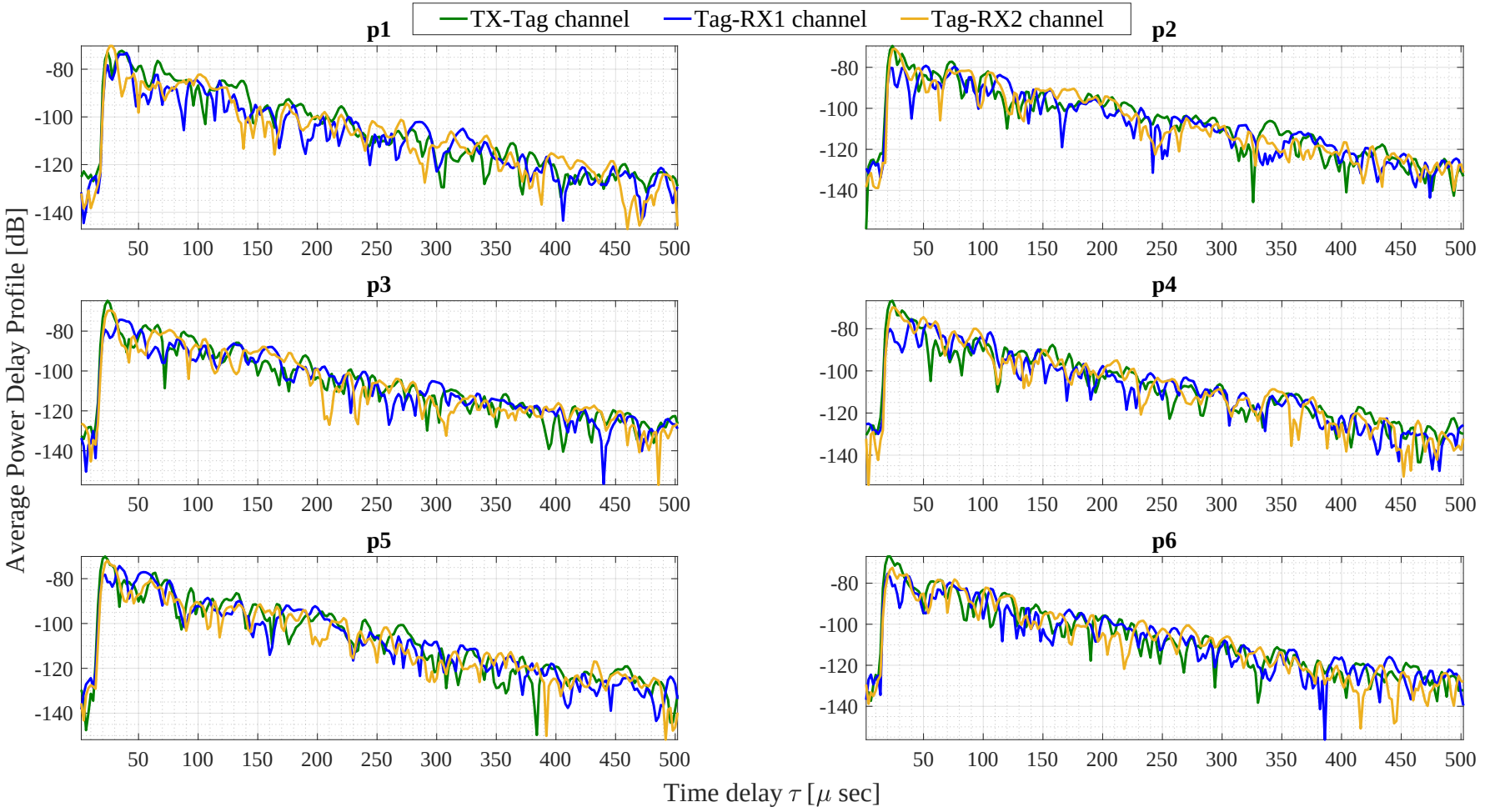

FIGURE A.1: $p1 - p6$, Tag Scenario

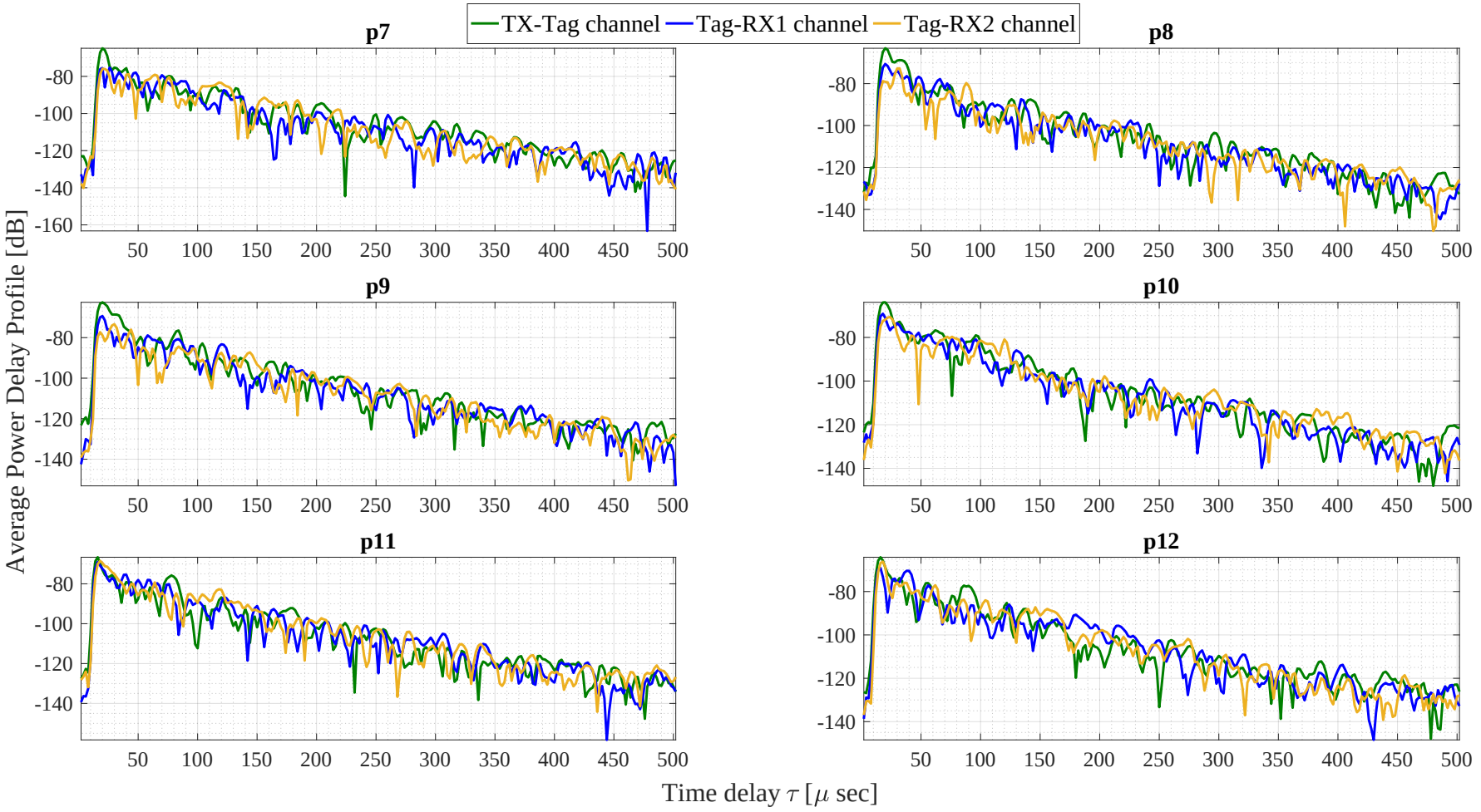

FIGURE A.2: $p7 - p12$, Tag Scenario

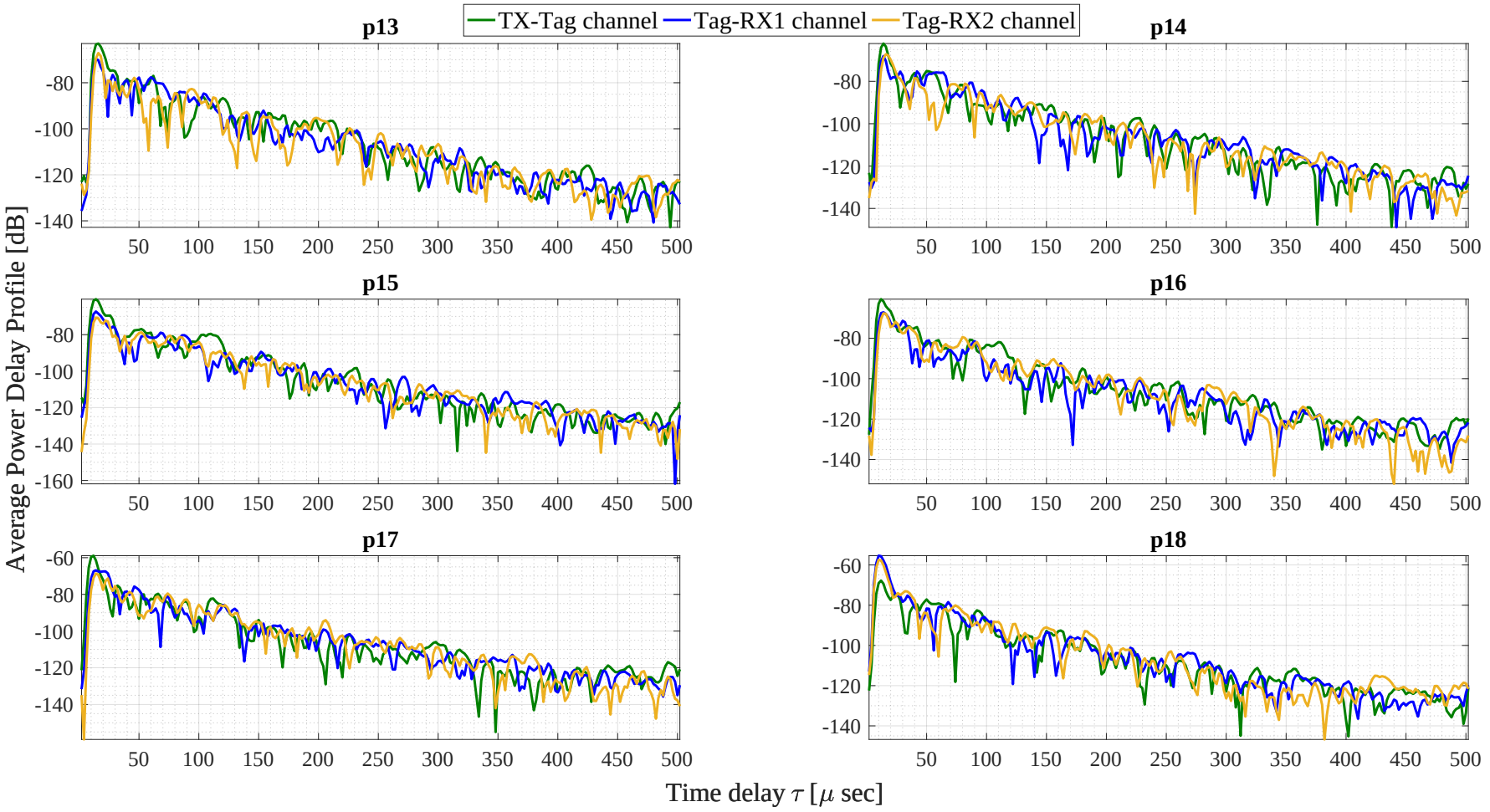

FIGURE A.3: $p13 - p18$, Tag Scenario

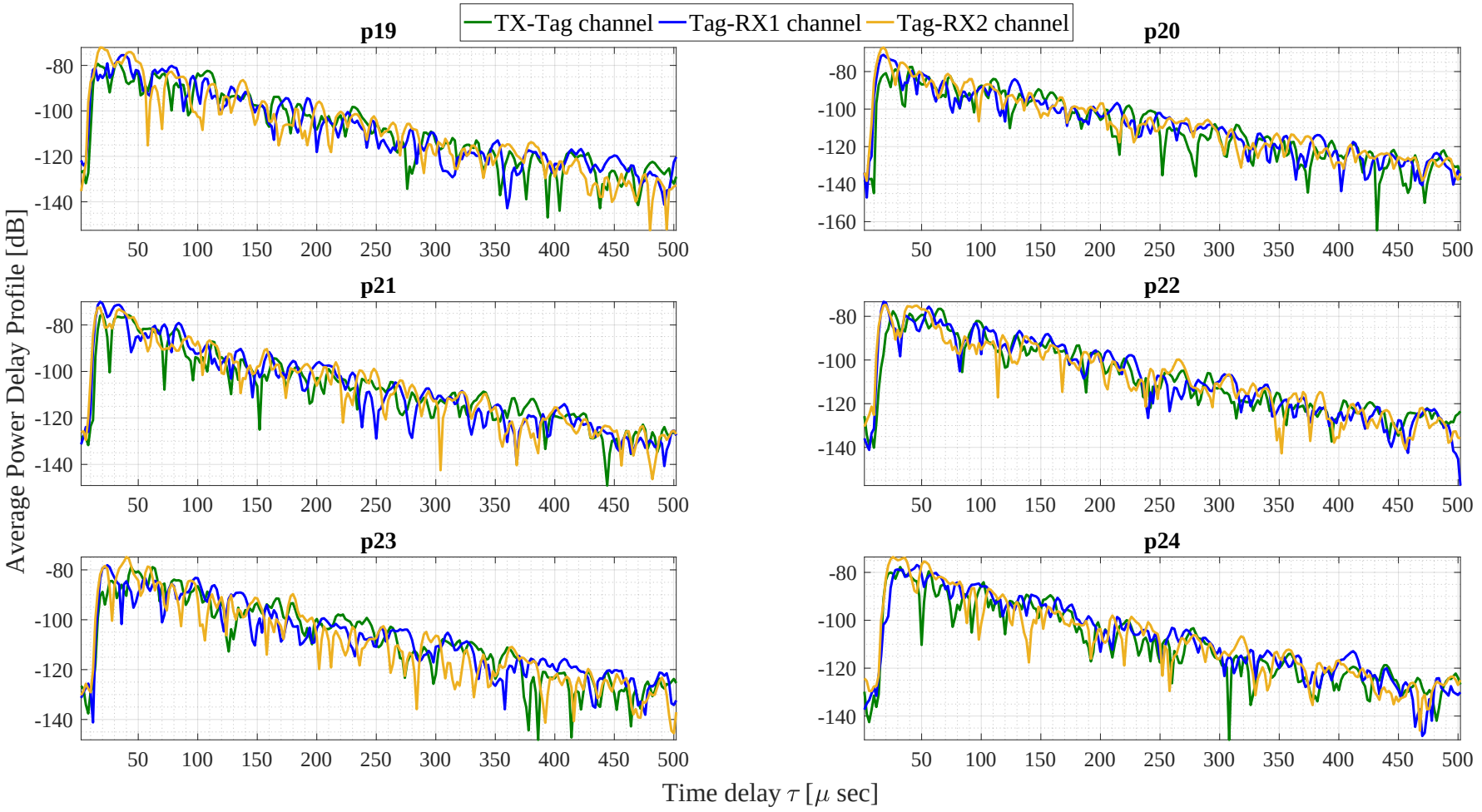

FIGURE A.4: $p19 - p24$, Tag Scenario

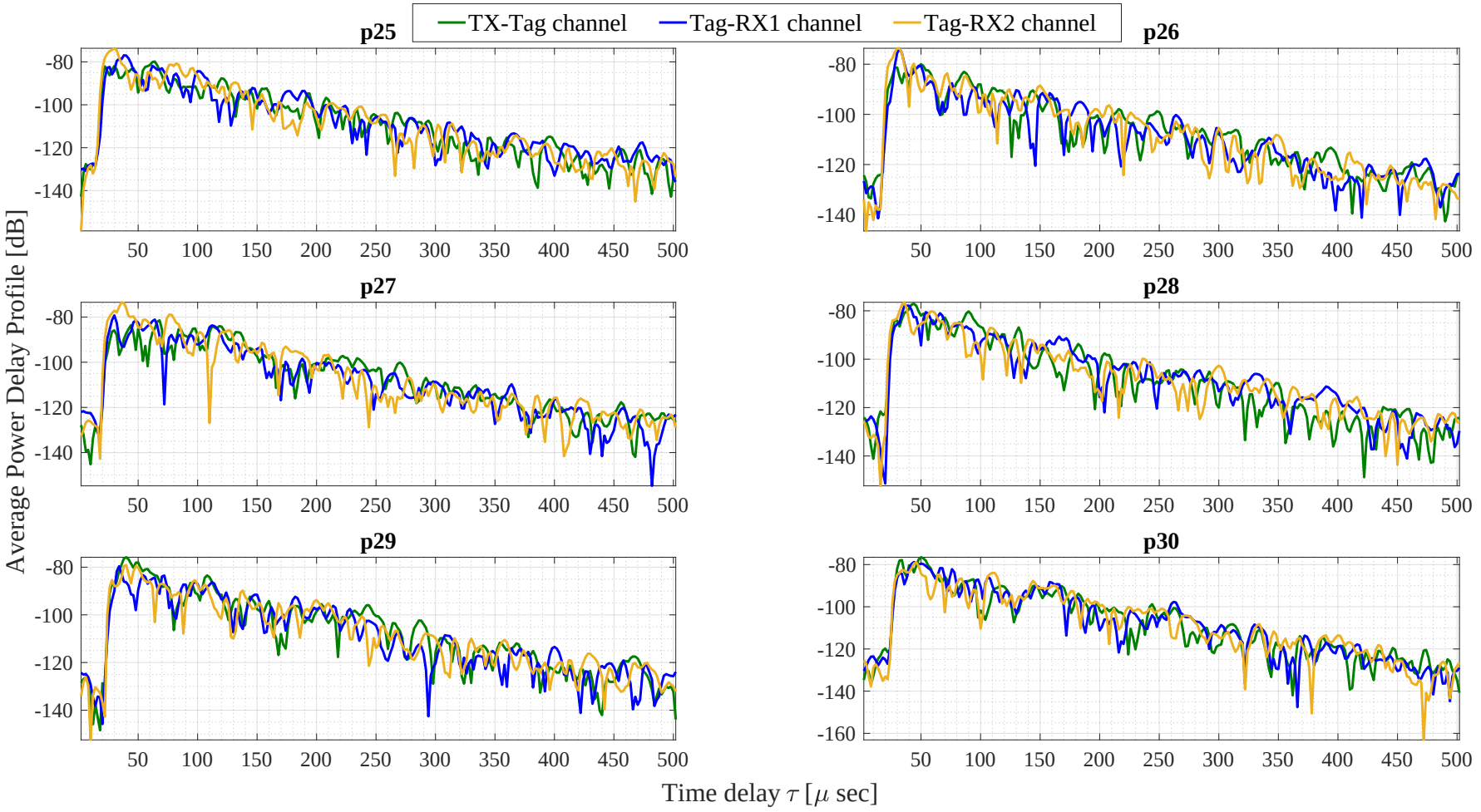

FIGURE A.5: $p25 - p30$, Tag Scenario

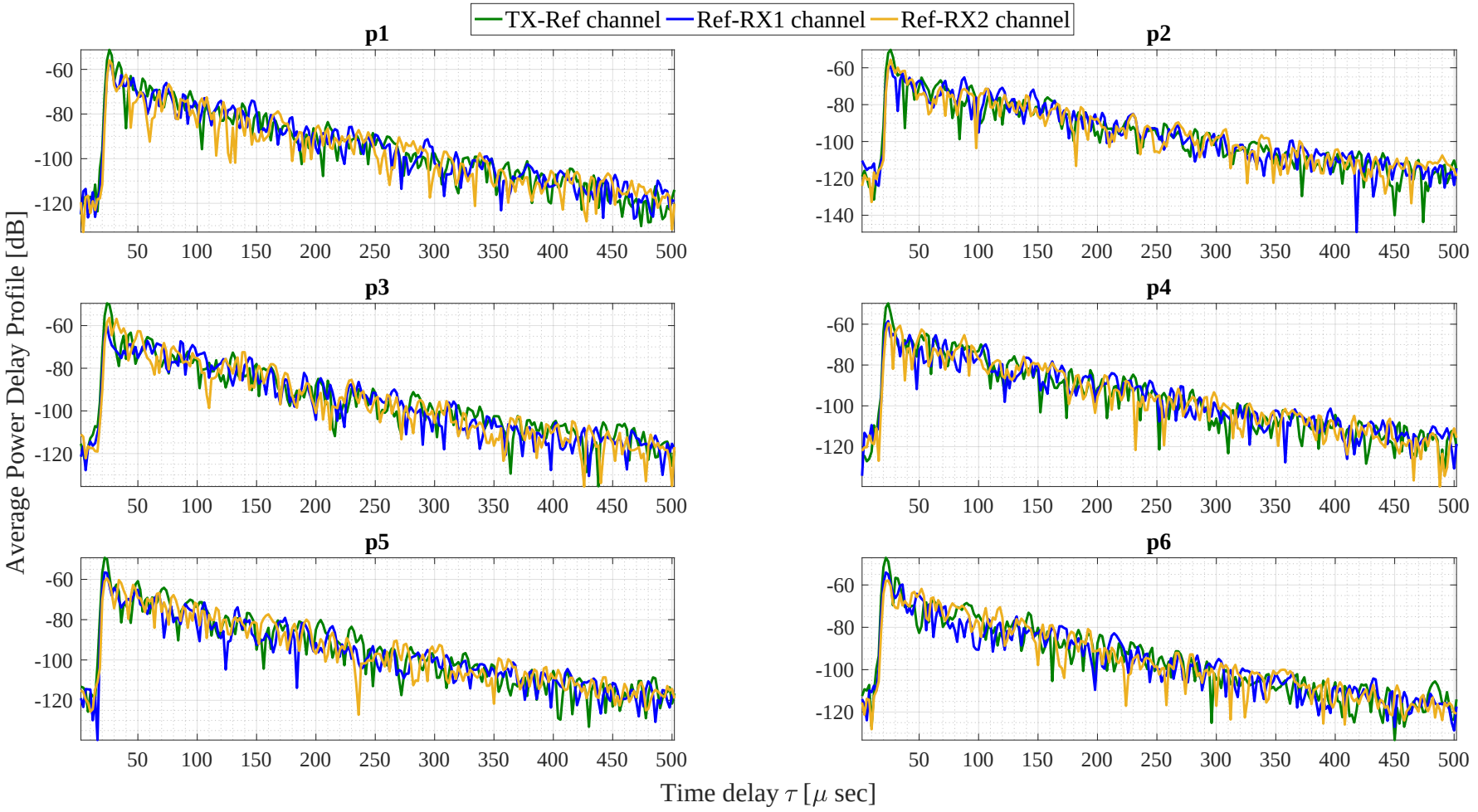

FIGURE A.6: $p1 - p6$, Reference Scenario

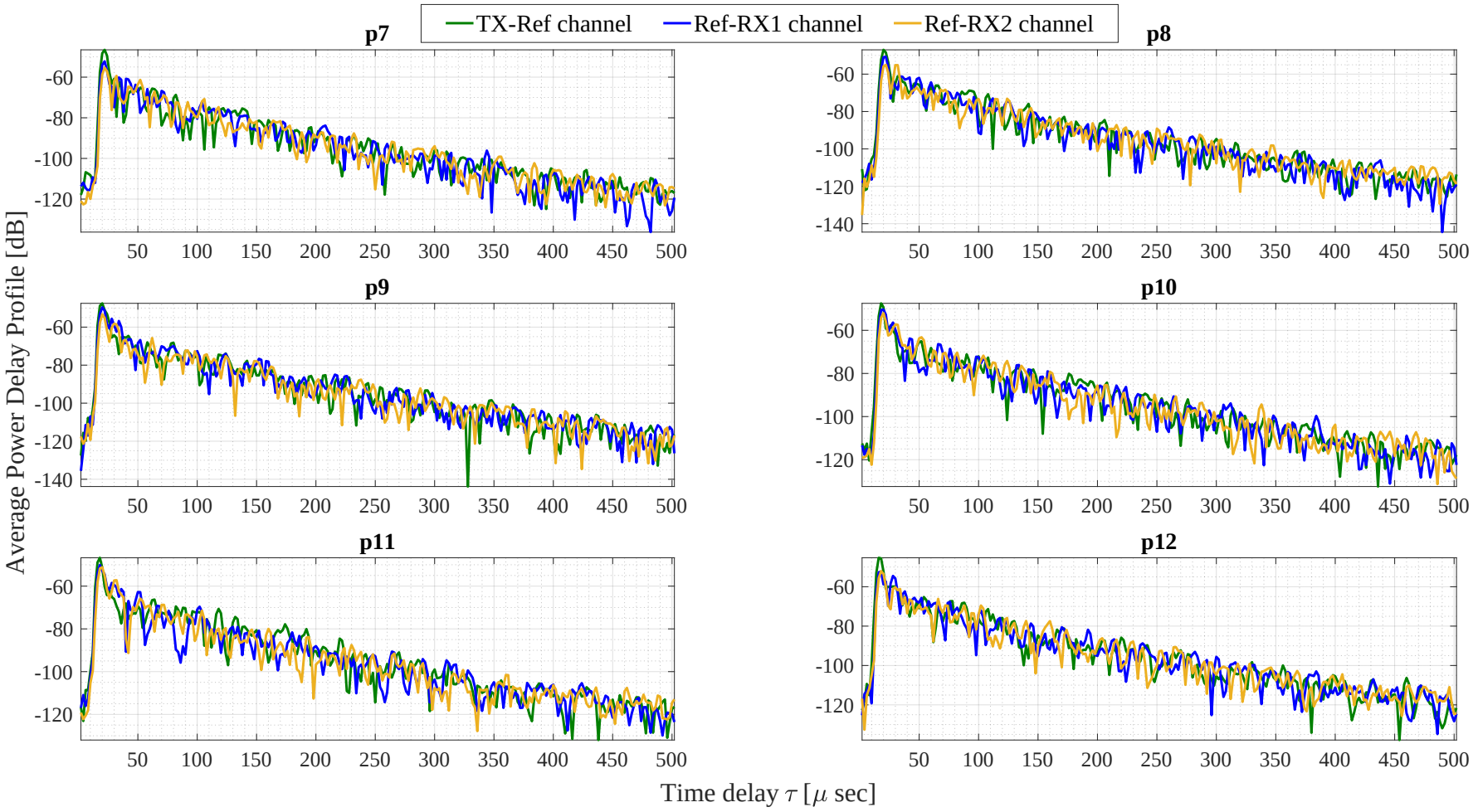

FIGURE A.7: $p7 - p12$, Reference Scenario

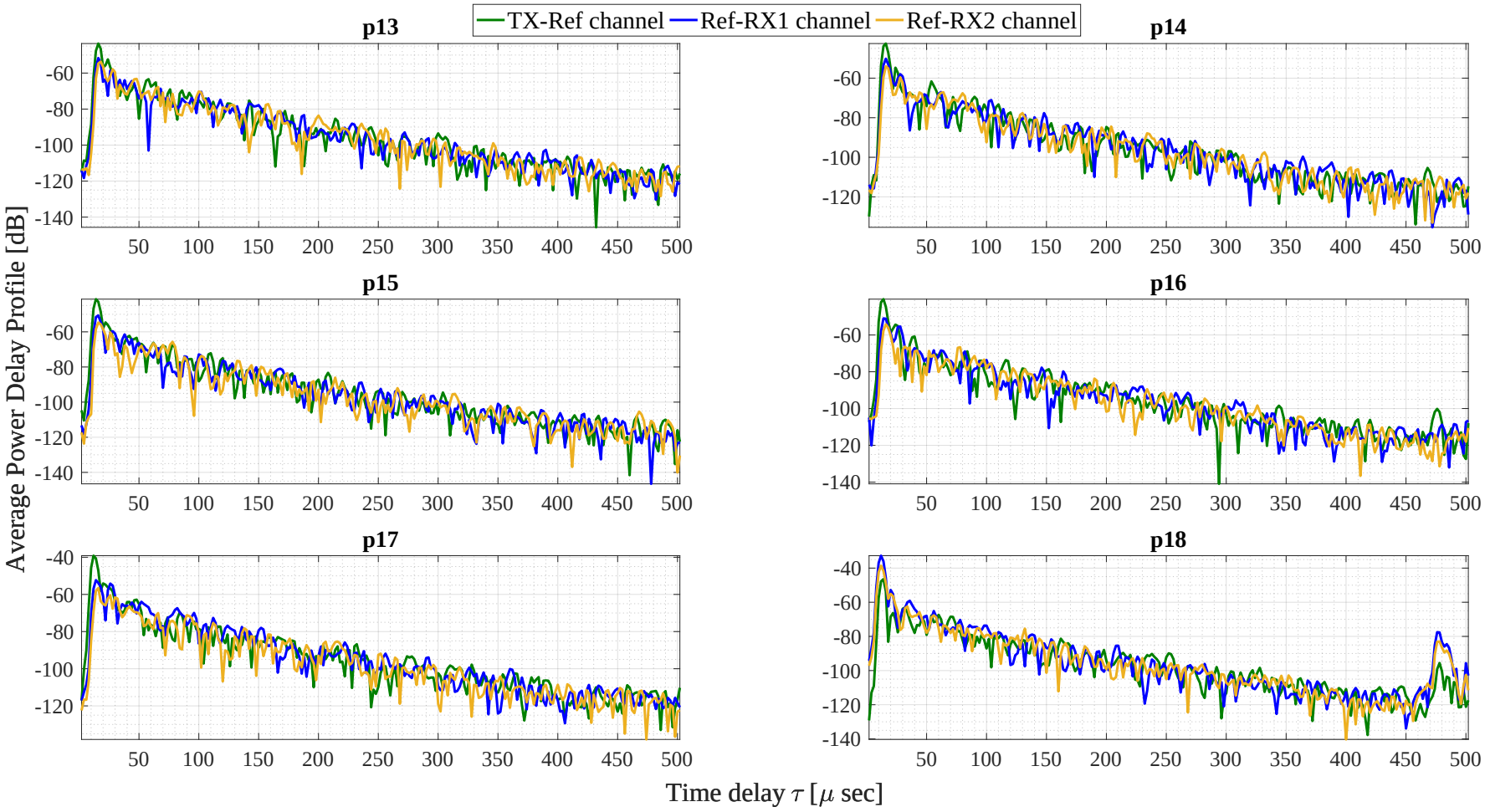

FIGURE A.8: p13-p18, Reference Scenario

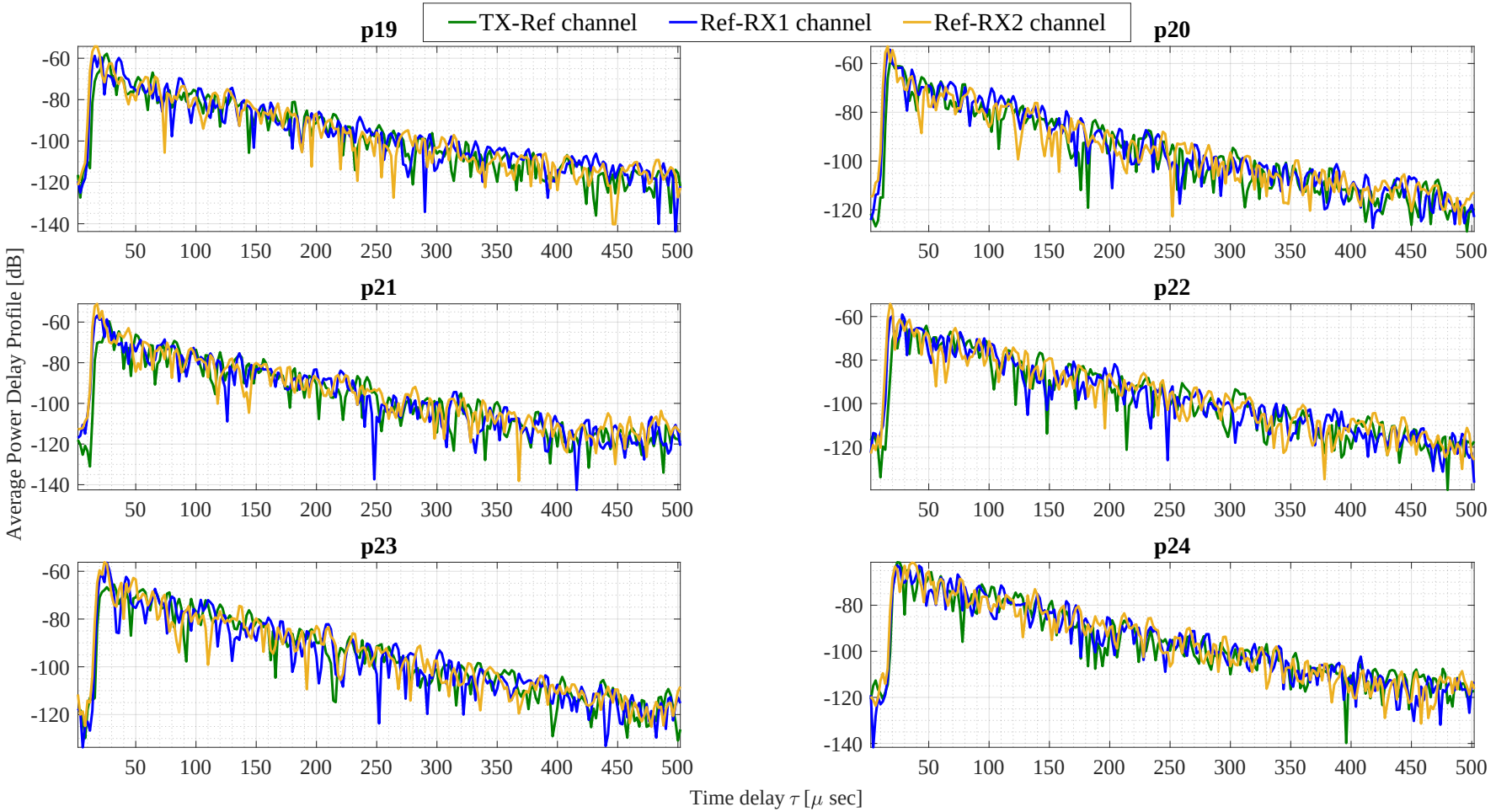

FIGURE A.9: $p19 - p24$, Reference Scenario

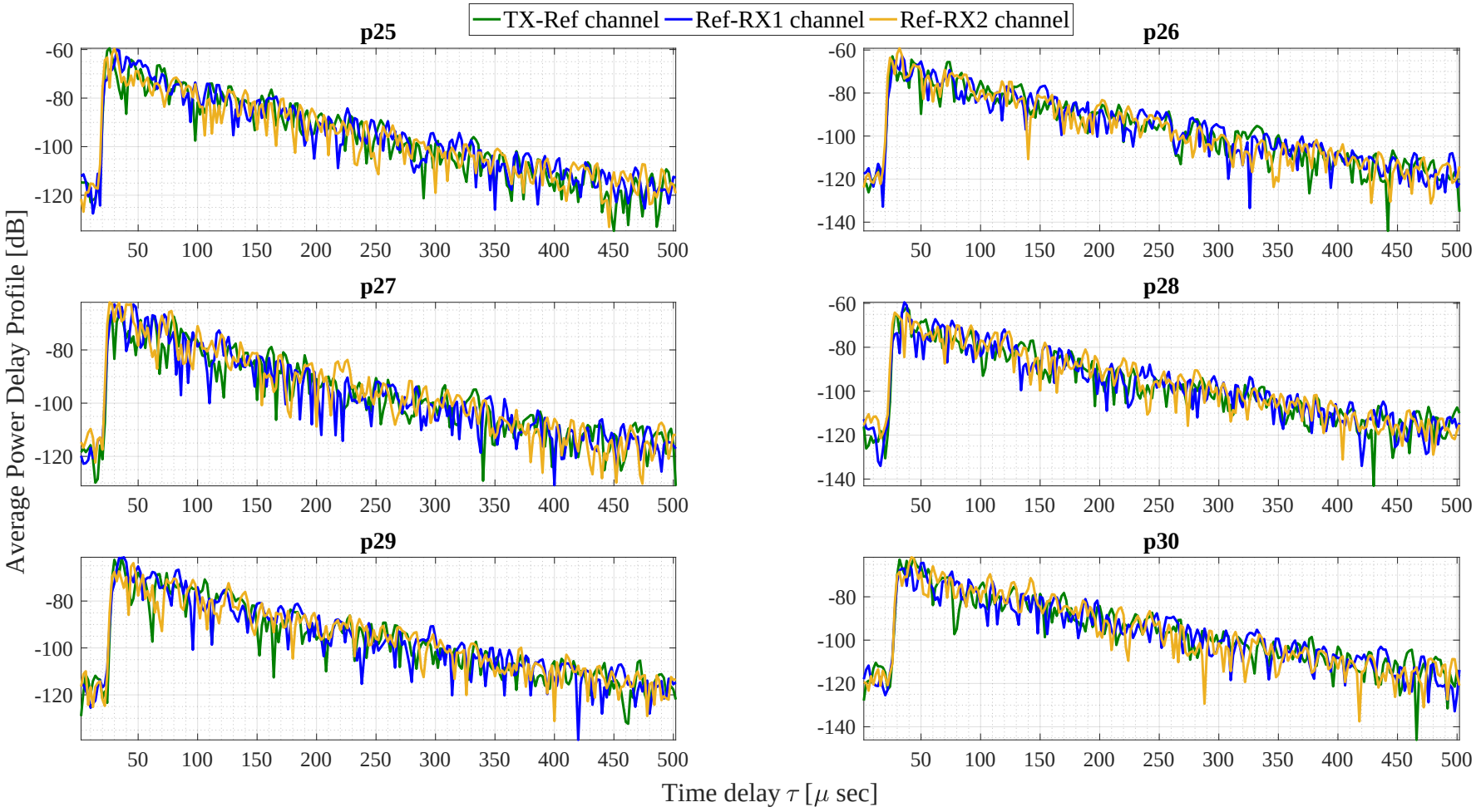

FIGURE A.10: $p25 - p30$, Reference Scenario

Appendix B

Own Publications

1. **Hasan Noor Khan**, Jasmin Grosinger, Lukas Görtschacher, Dominik Amschl, Peter Priller, Ulrich Muehlmann, and Wolfgang Bösch.,"Statistical analysis of the power delay profile of a SIMO UHF backscatter RFID channel in an engine test bed," *in Proceedings of Loughborough Antennas & Propagation Conference (LAPC), Loughborough*, 2016, pp. 1-5.

2. Lukas Görtschacher, Jasmin Grosinger, **Hasan Noor Khan**, and Wolfgang Bösch, "Fast Two Dimensional Position Update System for UHF RFID Tag Tracking," *accepted at the 2017 International Microwave Symposium (IMS).*

3. Lukas Görtschacher, Jasmin Grosinger, **Hasan Noor Khan**, Bernhard Auinger, Dominik Amschl, Peter Priller, Ulrich Muehlmann, and Wolfgang Bösch,"SIMO UHF RFID reader using sensor fusion for tag localization in a selected environment," *Elektrotechnik und Informationstechnik Springer Journal*", June 2016, Volume 133, Issue 3, pp 183–190,

4. Lukas Görtschacher, Jasmin Grosinger, **Hasan Noor Khan**, Dominik Amschl, Peter Priller, Ulrich Muehlmann, and Wolfgang Bösch,"SDR based RFID reader for passive tag localization using Phase Difference of Arrival Techniques,"*in Proceedings of IEEE MTT-S International Microwave Symposium (IMS)*, San Francisco, CA, 2016, pp. 1-4.

5. **Hasan Noor Khan**, Jasmin Grosinger, Bernhard Auinger, Dominik Amschl, Peter Priller, Ulrich Muehlmann, and Wolfgang Bösch, "Measurement based indoor SIMO RFID simulator for tag positioning," *in Proceedings of International*

EURASIP Workshop on RFID Technology (EURFID), Rosenheim, 2015, pp. 112-119.

6. Philipp Franz Freidl, **Hasan Noor Khan**, Michael Ernst Gadringer and Wolfgang Bösch, "Measurements and analysis of mm-Wave RFID channels," *in Proceedings of IEEE International Black Sea Conference on Communications and Networking (BlackSeaCom)*, Odessa, 2014, pp. 88-91.

Bibliography

[1] A. G. Bell, "Upon the production and reproduction of sound by light," *Telegraph Engineers, Journal of the Society of*, vol. 9, no. 34, pp. 404–426, 1880.

[2] P. Nikitin, "Leon Theremin (Lev Termen)," *IEEE Antennas and Propagation Magazine*, vol. 54, no. 5, pp. 252–257, Oct 2012.

[3] P. Wright, *SpyCatcher: The Candid Autobiography of a Senior Intelligence Officer*. Dell, 1988.

[4] H. Davis, "Eavesdropping using microwaves-addendum," 2005. [Online]. Available: http://eetimes.com/design/audio-design/4015284/Eavesdropping-using-microwaves-addendum

[5] G. Brooker and J. Gomez, "Lev Termen's Great Seal bug analyzed," *IEEE Aerospace and Electronic Systems Magazine*, vol. 28, no. 11, pp. 4–11, Nov 2013.

[6] D. M. Dobkin, *The RF in RFID: UHF RFID in Practice*. Newnes, 2012.

[7] H. Stockman, "Communication by means of reflected power," in *Institute of Radio Engineers*, vol. 36, October 1948, pp. 1196–1204. [Online]. Available: http://simson.net/ref/1948/stockman.pdf

[8] "EPC™ Radio-Frequency Identity Protocols Class-1 Generation-2 UHF RFID, Protocols for Communications at 860 MHz–960 MHz," EPCglobal Inc.®, EPCglobal Class-1 Gen-2, version 1.2.0 Standard, October 2008.

[9] "Auto-ID Labs." [Online]. Available: https://autoidlabs.org/

[10] B. Violino, "Wal–Mart Draws Line in the Sand," June 2003. [Online]. Available: http://www.rfidjournal.com/articles/view?462

[11] ——, "Wal–Mart Expands RFID Mandate," August 2003. [Online]. Available: http://www.rfidjournal.com/articles/view?539

[12] J. Landt, "Shrouds of Time: The History of RFID," The Association for Automatic Identification and Data Capture Technologies, Tech. Rep., 2001. [Online]. Available: http://www.aimglobal.org/technologies/rfid/resources/shrouds_of_time.pdf

[13] R. Want, "An introduction to RFID technology," *IEEE Pervasive Computing*, vol. 5, no. 1, pp. 25–33, Jan 2006.

[14] A. Rida, Y. Li, and M. Tentzeris, *RFID-enabled sensor design and applications*. Boston: Artech House, 2010.

[15] K. Finkenzeller, *RFID Handbook: Fundamentals and Applications in Contactless Smart Cards, Radio Frequency Identification and Near-Field Communication*. Wiley, 2010.

[16] M. Potdar, E. Chang, and V. Potdar, "Applications of RFID in Pharmaceutical Industry," in *Industrial Technology, 2006. ICIT 2006. IEEE International Conference on*, Dec 2006, pp. 2860–2865.

[17] D. Tang, R. Zhu, W. Gu, and K. Zheng, "RFID Applications in Automotive Assembly Line Equipped with Friction Drive Conveyors," in *Computer Supported Cooperative Work in Design (CSCWD), 2011 15th International Conference on*, June 2011, pp. 586–592.

[18] Y. Bo, F. Haiyan, and Z. Caijiang, "Application of RFID technology in Meat Circulation Management," in *Control Conference, 2008. CCC 2008. 27th Chinese*, July 2008, pp. 808–812.

[19] E. Welbourne, L. Battle, G. Cole, K. Gould, K. Rector, S. Raymer, M. Balazinska, and G. Borriello, "Building the internet of things using RFID: The RFID ecosystem experience," *Internet Computing, IEEE*, vol. 13, no. 3, pp. 48–55, May 2009.

[20] D. Bandyopadhyay and J. Sen, "Internet of things: Applications and challenges in technology and standardization," *Wireless Personal Communications*, vol. 58,

no. 1, pp. 49–69, 2011. [Online]. Available: http://dx.doi.org/10.1007/s11277-011-0288-5

[21] A. Al-Fuqaha, M. Guizani, M. Mohammadi, M. Aledhari, and M. Ayyash, "Internet of things: A survey on enabling technologies, protocols, and applications," *IEEE Communications Surveys Tutorials*, vol. 17, no. 4, pp. 2347–2376, Fourthquarter 2015.

[22] K. Ashton, "That 'Internet of Things' thing," June 2009. [Online]. Available: http://www.rfidjournal.com/articles/view?4986

[23] M. Bolic, M. Rostamian, and P. M. Djuric, "Proximity detection with RFID: A step toward the internet of things," *Pervasive Computing, IEEE*, vol. 14, no. 2, pp. 70–76, Apr 2015.

[24] C. Yang, W. Shen, and X. Wang, "Applications of internet of things in manufacturing," in *2016 IEEE 20th International Conference on Computer Supported Cooperative Work in Design (CSCWD)*, May 2016, pp. 670–675.

[25] S. Lu and X. Wang, "Toward an intelligent solution for perishable food cold chain management," in *2016 7th IEEE International Conference on Software Engineering and Service Science (ICSESS)*, Aug 2016, pp. 852–856.

[26] T. F. Aydos and J. C. E. Ferreira, "RFID-based system for Lean Manufacturing in the context of Internet of Things," in *2016 IEEE International Conference on Automation Science and Engineering (CASE)*, Aug 2016, pp. 1140–1145.

[27] L. Mainetti, L. Patrono, and M. L. Stefanizzi, "An internet of sport architecture based on emerging enabling technologies," in *2016 International Multidisciplinary Conference on Computer and Energy Science (SpliTech)*, July 2016, pp. 1–6.

[28] S. Bhushan, B. Bohara, P. Kumar, and V. Sharma, "A new approach towards IoT by using health care-IoT and food distribution IoT," in *2016 2nd International Conference on Advances in Computing, Communication, Automation (ICACCA) (Fall)*, Sept 2016, pp. 1–7.

[29] C. Boyer and S. Roy, "—Invited paper—Backscatter communication and RFID: coding, energy, and MIMO analysis," *IEEE Transactions on Communications*, vol. 62, no. 3, pp. 770–785, March 2014.

[30] W. H. Tranter, K. S. Shanmugan, T. S. Rappaport, and K. L. Kosbar, *Principles of Communication Systems Simulation with Wireless Applications.* Prentice Hall, 2004.

[31] V. Beroulle and D. H. Oum-El-Keir Aktouf, "System-level simulation for the dependability improvement of UHF RFID systems," *ICWMC 2016*, p. 58, 2016.

[32] D. Arnitz, "Tag Localization in Passive UHF RFID," Ph.D. dissertation, Graz University of Technology, Austria, May 2011.

[33] D. Arnitz, U. Muehlmann, T. Gigl, and K. Witrisal, "Wideband system-level simulator for passive UHF RFID," in *2009 IEEE International Conference on RFID*, April 2009, pp. 28–33.

[34] A. Janek, C. Steger, R. WeiB, J. Preishuber-Pfluegl, and M. Pistauer, "Functional verification of future higher class UHF RFID tag architectures based on cosimulation," in *2008 IEEE International Conference on RFID*, April 2008, pp. 336–343.

[35] V. Derbek, C. Steger, S. Kajtazovic, J. Preishuber-Pfluegl, and M. Pistauer, "Behavioral model of UHF RFID tag for system and application level simulation," in *BMAS 2005. Proceedings of the 2005 IEEE International Behavioral Modeling and Simulation Workshop, 2005.*, Sept 2005, pp. 60–63.

[36] V. Beroulle, R. Khouri, T. Vuong, and S. Tedjini, "Behavioral modeling and simulation of antennas: radio-frequency identification case study," in *Proceedings of the 2003 IEEE International Workshop on Behavioral Modeling and Simulation*, Oct 2003, pp. 102–106.

[37] C. Floerkemeier and R. Pappu, "Evaluation of RFIDSim - a physical and logical layer RFID simulation engine," in *2008 IEEE International Conference on RFID*, April 2008, pp. 350–356.

[38] C. Floerkemeier and S. Sarma, "RFIDSim—a physical and logical layer simulation engine for passive RFID," *IEEE Transactions on Automation Science and Engineering*, vol. 6, no. 1, pp. 33–43, Jan 2009.

[39] K. K.-W. Yu, "RFIDSim–A Discrete Event Simulator for Radio Frequency Identification Systems," Ph.D. dissertation, Massachusetts Institute of Technology, USA, 2003.

[40] "Parameters for air interface communications at 860 MHz to 960 MHz," International Organization for Standardization, ISO/IEC 18000-6C Standard.

[41] M. C. O'Connor, "Gen 2 EPC Protocol Approved as ISO 18000-6C," July 2006. [Online]. Available: http://www.rfidjournal.com/articles/view?2481

[42] R. Barr, "An Efficient, Unifying Approach to Simulation Using Virtual Machines," Ph.D. dissertation, Cornell University, USA, 2004.

[43] V. Derbek, J. Preishuber-Pflueg, C. Steger, and M. Pistauer, "Architecture for model-based UHF RFID system design verification," in *Proceedings of the 2005 European Conference on Circuit Theory and Design, 2005.*, vol. 2, Aug 2005, pp. II/181–II/184 vol. 2.

[44] V. Derbek, C. Steger, S. Kajtazovic, J. Preishuber-Pfluegl, and M. Pistauer, "Behavioral model of UHF RFID tag for system and application level simulation," in *BMAS 2005. Proceedings of the 2005 IEEE International Behavioral Modeling and Simulation Workshop, 2005.*, Sept 2005, pp. 60–63.

[45] J. Li and C. Tao, "Analysis and simulation of UHF RFID system," in *2006 8th international Conference on Signal Processing*, vol. 4, Nov 2006.

[46] Y. Han, Q. Li, and H. Min, "System modelling and simulation of RFID," 2005.

[47] S. A. Chakra, U. O. Farrukh, and B. A. Garcia, "Electrical model simulation for a UHF RFID system," in *2009 First International Conference on Computational Intelligence, Communication Systems and Networks*, July 2009, pp. 155–159.

[48] R. Szumny, K. Kurek, S. Kozlowski, and J. Modelski, "Measurements and analysis of the propagation channel for various indoor environments," in *EUROCON 2007 - The International Conference on "Computer as a Tool"*, Sept 2007, pp. 990–996.

[49] E. Bonek, N. Czink, V.-M. Holappa, M. Alatossava, L. Hentilä, J.-P. Nuutinen, and A. Pal, *Indoor MIMO meaurements at 2.55 and 5.25 GHz-a comparison of temporal and angular characteristics.* na, 2006.

[50] P. G. Flikkema and S. G. Johnson, "A comparison of time- and frequency-domain wireless channel sounding techniques," in *Southeastcon '96. Bringing Together Education, Science and Technology., Proceedings of the IEEE*, Apr 1996, pp. 488–491.

[51] H. K. Chung, N. Vloeberghs, H. K. Kwon, S. J. Lee, and K. C. Lee, "MIMO channel sounder implementation and effects of sounder impairment on statistics of multipath delay spread," in *VTC-2005-Fall. 2005 IEEE 62nd Vehicular Technology Conference, 2005.*, vol. 1, Sept 2005, pp. 349–353.

[52] M. Patzold, *Mobile Radio Channels*. Wiley, 2011.

[53] Elektrobit, "PROP Sim C2 Wideband Radio Channel Simulator." [Online]. Available: https://www.wirelessnetworksonline.com/doc/prop-sim-c2-wideband-radio-channel-simulator-0001

[54] C. Angerer, "Design and Exploration of Radio Frequency Identification Systems by Rapid Prototyping," Ph.D. dissertation, Institut für Nachrichtentechnik und Hochfrequenztechnik, Vienna University of Technology, 2010.

[55] P. V. Nikitin and K. V. S. Rao, "Antennas and propagation in UHF RFID systems," in *2008 IEEE International Conference on RFID*, April 2008, pp. 277–288.

[56] S. Preradovic and N. C. Karmakar, "RFID readers–a review," in *2006 International Conference on Electrical and Computer Engineering*, Dec 2006, pp. 100–103.

[57] K. Penttila, L. Sydanheimo, and M. Kivikoski, "Implementation of Tx/Rx isolation in an RFID reader," *International Journal of Radio Frequency Identification Technology and Applications*, vol. 1, no. 1, pp. 74–89, 2006. [Online]. Available: http://www.inderscienceonline.com/doi/abs/10.1504/IJRFITA.2006.010708

[58] P. Nikitin and K. Rao, "Theory and measurement of backscattering from RFID tags," *Antennas and Propagation Magazine, IEEE*, vol. 48, no. 6, pp. 212–218, Dec 2006.

[59] J. Grosinger and A. L. Scholtz, "Antennas and wave propagation in novel wireless sensing applications based on passive UHF RFID," *Elektrotechnik und Informationstechnik*, vol. 128, no. 11-12, pp. 408–414, 2011. [Online]. Available: http://dblp.uni-trier.de/db/journals/ei/ei128.html#GrosingerS11

[60] J. D. Griffin, "High-Frequency Modulated-Backscatter Communication Using Multiple Antennas," Ph.D. dissertation, School of Electrical and Computer Engineering, Georgia Institute of Technology, 2009.

[61] M. S. Trotter, J. D. Griffin, and G. D. Durgin, "Power-optimized waveforms for improving the range and reliability of RFID systems," in *2009 IEEE International Conference on RFID*, April 2009, pp. 80–87.

[62] A. M. Younes, K. Hassan, and K. ElMahgoub, "Link-level simulation for far field UHF RFID with off-line channel coding," in *2013 Second International Japan-Egypt Conference on Electronics, Communications and Computers (JEC-ECC)*, Dec 2013, pp. 7–11.

[63] J. Grosinger, "Backscatter Radio Frequency Systems and Devices for Novel Wireless Sensing Applications," Ph.D. dissertation, Institut für Nachrichtentechnik und Hochfrequenztechnik, Vienna University of Technology, 2012.

[64] K. Kurokawa, "Power waves and the scattering matrix," *IEEE Transactions on Microwave Theory and Techniques*, vol. 13, no. 2, pp. 194–202, Mar 1965.

[65] K. V. S. Rao, P. V. Nikitin, and S. F. Lam, "Antenna design for UHF RFID tags: a review and a practical application," *IEEE Transactions on Antennas and Propagation*, vol. 53, no. 12, pp. 3870–3876, Dec 2005.

[66] ——, "Impedance matching concepts in RFID transponder design," in *Fourth IEEE Workshop on Automatic Identification Advanced Technologies (AutoID'05)*, Oct 2005, pp. 39–42.

[67] J. Grosinger, L. Görtschacher, and W. Bösch, "Passive RFID sensor tag concept and prototype exploiting a full control of amplitude and phase of the tag signal," *IEEE Transactions on Microwave Theory and Techniques*, vol. 64, no. 12, pp. 4752–4762, Dec 2016.

[68] J. P. Curty, M. Declercq, C. Dehollain, and N. Joehl, *Design and Optimization of Passive UHF RFID Systems*, 2007th ed. Springer, 10 2006. [Online]. Available: http://amazon.com/o/ASIN/0387352740/

[69] L. W. Mayer, "Antenna Design for Future Multi-Standard and Multi-Frequency RFID Systems," Ph.D. dissertation, Fakultät für Elektrotechnik und Informationstechnik, Vienna University of Technology, 2009.

[70] P. V. Nikitin and K. V. S. Rao, "Performance limitations of passive UHF RFID systems," in *2006 IEEE Antennas and Propagation Society International Symposium*, July 2006, pp. 1011–1014.

[71] B. Rembold, "Optimum modulation efficiency and sideband backscatter power response of RFID-tags," *Frequenz-Journal of RF Engineering and Telecommunications*, vol. 63, no. 1-2, pp. 9–13, 2009.

[72] P. Nikitin, K. Rao, and R. Martinez, "Differential RCS of RFID tag," *Electronics Letters*, vol. 43, no. 8, pp. 431–432, April 2007.

[73] D. Paret, *RFID at Ultra and Super High Frequencies: Theory and application.* Wiley, 2010.

[74] D.-Y. Kim, H.-S. Jo, H. Yoon, C. Mun, B.-J. Jang, and J.-G. Yook, "Reverse-Link Interrogation Range of a UHF MIMO-RFID System in Nakagami-m Fading Channels," *Industrial Electronics, IEEE Transactions on*, vol. 57, no. 4, pp. 1468–1477, April 2010.

[75] G. Smietanka and J. Götze, "Modeling and simulation of MISO diversity for UHF RFID communication," in *2012 Federated Conference on Computer Science and Information Systems (FedCSIS)*, Sept 2012, pp. 813–820.

[76] R. Zekavat and R. M. Buehrer, *Handbook of Position Location: Theory, Practice and Advances (IEEE Series on Digital & Mobile Communication).* Wiley-IEEE Press, 2012.

[77] D. Bartlett, *Essentials of Positioning and Location Technology (The Cambridge Wireless Essentials Series).* Cambridge University Press, 2013.

[78] H. Liu, H. Darabi, P. Banerjee, and J. Liu, "Survey of wireless indoor positioning techniques and systems," *IEEE Transactions on Systems, Man, and Cybernetics, Part C (Applications and Reviews)*, vol. 37, no. 6, pp. 1067–1080, Nov 2007.

[79] R. Campos and L. Lovisolo, *RF Positioning: Fundamentals, Applications, and Tools*, ser. Gnss Technology and Applications. Artech House, 2015.

[80] F. Zheng and T. Kaiser, *Digital Signal Processing for RFID (Information and Communication Technology Series,)*. Wiley, 2016.

[81] S. Gezici and H. V. Poor, "Position estimation via ultra-wide-band signals," *Proceedings of the IEEE*, vol. 97, no. 2, pp. 386–403, Feb 2009.

[82] T. Kaiser and F. Zheng, *Ultra Wideband Systems with MIMO*. Wiley, 2010.

[83] H. Arthaber, T. Faseth, and F. Galler, "Spread-spectrum based ranging of passive UHF EPC RFID tags," *IEEE Communications Letters*, vol. 19, no. 10, pp. 1734–1737, Oct 2015.

[84] S. B. Miles, S. E. Sarma, and J. R. Williams, Eds., *RFID Technology and Applications*. Cambridge University Press, 2008.

[85] M. Kanaan, M. Heidari, F. Akgul, and K. Pahlavan, "Technical aspects of localization in indoor wireless networks," *Bechtel Telecommunications Technical Journal*, vol. 5, no. 1, pp. 47–58, 2006.

[86] C. Atock, "Where's my stuff? [supply chain management]," *Manufacturing Engineer*, vol. 82, no. 2, pp. 24–27, April 2003.

[87] J. Heidrich, D. Brenk, J. Essel, S. Schwarzer, K. Seemann, G. Fischer, and R. Weigel, "The roots, rules, and rise of RFID," *IEEE Microwave Magazine*, vol. 11, no. 3, pp. 78–86, May 2010.

[88] S. A. Ahson and M. Ilyas, *RFID Handbook: Applications, Technology, Security, and Privacy*. CRC Press, 2008.

[89] R. Miesen, R. Ebelt, F. Kirsch, T. Schäfer, G. Li, H. Wang, and M. Vossiek, "Where is the Tag?" *Microwave Magazine, IEEE*, vol. 12, no. 7, pp. S49–S63, Dec 2011.

[90] P. V. Nikitin, R. Martinez, S. Ramamurthy, H. Leland, G. Spiess, and K. V. S. Rao, "Phase based spatial identification of UHF RFID tags," in *2010 IEEE International Conference on RFID (IEEE RFID 2010)*, April 2010, pp. 102–109.

[91] M. Scherhaufl, M. Pichler, E. Schimback, D. Muller, A. Ziroff, and A. Stelzer, "Indoor localization of passive UHF RFID tags based on phase-of-arrival evaluation," *IEEE Transactions on Microwave Theory and Techniques*, vol. 61, no. 12, pp. 4724–4729, Dec 2013.

[92] W. Von Aulock, "Properties of phased arrays," *Proceedings of the IRE*, vol. 48, no. 10, pp. 1715–1727, Oct 1960.

[93] L. Brennan, "Angular accuracy of a phased array radar," *Antennas and Propagation, IRE Transactions on*, vol. 9, no. 3, pp. 268–275, May 1961.

[94] H. L. V. Trees, *Detection, Estimation, and Modulation Theory, Optimum Array Processing (Part IV)*. Wiley-Interscience, 2002.

[95] J. Wang and D. Katabi, "Dude, where's my card?: RFID positioning that works with multipath and non-line of sight," in *Proceedings of the ACM SIGCOMM 2013 Conference on SIGCOMM*, ser. SIGCOMM '13. New York, NY, USA: ACM, 2013, pp. 51–62. [Online]. Available: http://doi.acm.org/10.1145/2486001.2486029

[96] C. Zhou and J. D. Griffin, "Accurate phase-based ranging measurements for backscatter RFID tags," *IEEE Antennas and Wireless Propagation Letters*, vol. 11, pp. 152–155, 2012.

[97] A. Povalac and J. Sebesta, "Phase difference of arrival distance estimation for RFID tags in frequency domain," in *RFID-Technologies and Applications (RFID-TA), 2011 IEEE International Conference on*, Sept 2011, pp. 188–193.

[98] M. Bolic, D. Simplot-Ryl, and I. Stojmenovic, Eds., *RFID Systems: Research Trends and Challenges*. Wiley, 2010.

[99] "MATLAB®, Version 8.5.0.197613 (R2015a)," The MathWorks Inc., Natick, Massachusetts, United States, 2015.

[100] "Simulink®, Version 8.5 (R2015a)," The MathWorks Inc., Natick, Massachusetts, United States, 2015.

[101] "SimRF™, Version 4.4 (Release 2015a)," The MathWorks Inc., Natick, Massachusetts, United States, 2015.

[102] "RF Blockset™, Version 6.0 (R2017a)," The MathWorks Inc., Natick, Massachusetts, United States, 2017. [Online]. Available: https://de.mathworks.com/help/pdf_doc/simrf/rn.pdf

[103] "RF Toolbox™, Version 2.16 (R2015a)," The MathWorks Inc., Natick, Massachusetts, United States, 2015.

[104] "Communications System Toolbox™, Version 6.0 (Release 2015a)," The MathWorks Inc., Natick, Massachusetts, United States, 2015.

[105] "DSP System Toolbox™, Version 9.0 (Release 2015a)," The MathWorks Inc., Natick, Massachusetts, United States, 2015.

[106] D. Dardari, R. D'Errico, C. Roblin, A. Sibille, and M. Z. Win, "Ultrawide bandwidth RFID: The next generation?" *Proceedings of the IEEE*, vol. 98, no. 9, pp. 1570–1582, Sept 2010.

[107] D. Arnitz, U. Muehlmann, and K. Witrisal, "Characterization and modeling of UHF RFID channels for ranging and localization," *IEEE Transactions on Antennas and Propagation*, vol. 60, no. 5, pp. 2491–2501, May 2012.

[108] N. Decarli, F. Guidi, and D. Dardari, "Passive UWB RFID for tag localization: Architectures and design," *IEEE Sensors Journal*, vol. 16, no. 5, pp. 1385–1397, March 2016.

[109] L. Görtschacher, J. Grosinger, H. N. Khan, D. Amschl, P. Priller, U. Muehlmann, and W. Bösch, "SDR based RFID reader for passive tag localization using phase difference of arrival techniques," in *Proceedings of the IEEE MTT-S (IMS), International Microwave Symposium*, 2016.

[110] T. Faseth, M. Winkler, H. Arthaber, and G. Magerl, "The influence of multipath propagation on phase-based narrowband positioning principles in UHF RFID," in *Antennas and Propagation in Wireless Communications (APWC), 2011 IEEE-APS Topical Conference on*, Sept 2011, pp. 1144–1147.

[111] M. Hasani, A. Vena, L. Sydänheimo, M. M. Tentzeris, and L. Ukkonen, "A novel enhanced–performance flexible RFID-enabled embroidered wireless integrated module for sensing applications," *IEEE Transactions on Components, Packaging and Manufacturing Technology*, vol. 5, no. 9, pp. 1244–1252, Sept 2015.

[112] E. Welbourne, M. Balazinska, G. Borriello, and W. Brunette, "Challenges for pervasive RFID-based infrastructures," in *Pervasive Computing and Communications Workshops, 2007. PerCom Workshops '07. Fifth Annual IEEE International Conference on*, March 2007, pp. 388–394.

[113] A. Lazaro, D. Girbau, and D. Salinas, "Radio Link Budgets for UHF RFID on Multipath Environments," *Antennas and Propagation, IEEE Transactions on*, vol. 57, no. 4, pp. 1241–1251, April 2009.

[114] W. Yong and L. Qing, "Research on UHF RFID wireless channel," in *2016 Sixth International Conference on Instrumentation Measurement, Computer, Communication and Control (IMCCC)*, July 2016, pp. 752–755.

[115] A. A. M. Saleh and R. Valenzuela, "A statistical model for indoor multipath propagation," *IEEE Journal on Selected Areas in Communications*, vol. 5, no. 2, pp. 128–137, February 1987.

[116] S. J. Howard and K. Pahlavan, "Measurement and analysis of the indoor radio channel in the frequency domain," *IEEE Transactions on Instrumentation and Measurement*, vol. 39, no. 5, pp. 751–755, Oct 1990.

[117] A. Loeffler and H. Gerhaeuser, "Stochastic and deterministic broadband UHF RFID channel models for indoor localization," in *Smart SysTech 2013; European Conference on Smart Objects, Systems and Technologies*, June 2013, pp. 1–7.

[118] P. Bello, "Characterization of randomly time-variant linear channels," *IEEE Transactions on Communications Systems*, vol. 11, no. 4, pp. 360–393, December 1963.

[119] H. N. Khan, J. Grosinger, L. Görtschacher, D. Amschl, P. Priller, U. Muehlmann, and W. Bösch, "Statistical analysis of the power delay profile of a SIMO UHF backscatter RFID channel in an engine test bed," in *2016 Loughborough Antennas Propagation Conference (LAPC)*, Nov 2016, pp. 1–5.

[120] L. Görtschacher, J. Grosinger, B. Auinger, D. Amschl, P. Priller, U. Muehlmann, and W. Bösch, "SIMO RFID system performance in an engine test bed," in *RFID Technology (EURFID), 2015 International EURASIP Workshop on*, Oct 2015, pp. 120–125.

[121] SanaSalous, *Radio Propagation Measurement and Channel Modelling*. Wiley, 2013.

[122] Motorola, *RFID Antenna Family*, May 2015. [Online]. Available: http://www.barcodesinc.com/pdf/Motorola/an-series.pdf

[123] A. F. Molisch, *Wireless Communications*. Wiley, 2010.

[124] M. S. Varela and M. G. Sanchez, "RMS delay and coherence bandwidth measurements in indoor radio channels in the UHF band," *IEEE Transactions on Vehicular Technology*, vol. 50, no. 2, pp. 515–525, Mar 2001.

[125] M. Wittmann, J. Marti, and T. Kurner, "Impact of the power delay profile shape on the bit error rate in mobile radio systems," *IEEE Transactions on Vehicular Technology*, vol. 46, no. 2, pp. 329–339, May 1997.

[126] J. Karedal, S. Wyne, P. Almers, F. Tufvesson, and A. F. Molisch, "A measurement-based statistical model for industrial ultra-wideband channels," *IEEE Transactions on Wireless Communications*, vol. 6, no. 8, pp. 3028–3037, August 2007.

[127] T. Rappaport, *Wireless Communications: Principles and Practice*, 2nd ed. Upper Saddle River, NJ, USA: Prentice Hall PTR, 2001.

[128] J. D. Parsons, *The Mobile Radio Propagation Channel, 2nd Edition*. Wiley, 2000.

[129] L. J. Greenstein, V. Erceg, Y. S. Yeh, and M. V. Clark, "A new path-gain/delay-spread propagation model for digital cellular channels," *IEEE Transactions on Vehicular Technology*, vol. 46, no. 2, pp. 477–485, May 1997.

[130] "SimRF™ Getting Started Guide, Version 4.4 (R2015a)," The MathWorks Inc., Natick, Massachusetts, United States, 2015.

[131] S. K. Kim, S. S. Nam, and S. H. Cho, "A FPGA design of the I/Q signal combining for UHF RFID reader receiver," in *2010 2nd IEEE InternationalConference on Network Infrastructure and Digital Content*, Sept 2010, pp. 556–560.

[132] D. Silage, *Digital Communication Systems Using MATLAB and Simulink, Second Edition*. Bookstand Publishing, 2009.

[133] W. Y. Yang, Y. S. Cho, W. G. Jeon, J. W. Lee, J. H. Paik, J. K. Kim, M.-H. Lee, K. I. Lee, K. W. Park, and K. S. Woo, *MATLAB/Simulink for Digital Communication*. A-Jin Publishing, 2009.

[134] H. N. Khan, J. Grosinger, B. Auinger, D. Amschl, P. Priller, U. Muehlmann, and W. Bösch, "Measurement based indoor SIMO RFID simulator for tag positioning," in *International EURASIP Workshop on RFID Technology (EURFID)*, Oct 2015, pp. 112–119.

[135] C. Hekimian-Williams, B. Grant, X. Liu, Z. Zhang, and P. Kumar, "Accurate localization of RFID tags using phase difference," in *RFID, 2010 IEEE International Conference on*, April 2010, pp. 89–96.

[136] C. Ding, D. Pei, and A. Salomaa, *Chinese Remainder Theorem: Applications in Computing, Coding, Cryptography.* River Edge, NJ, USA: World Scientific Publishing Co., Inc., 1996.

[137] X. Li, Y. Zhang, and M. G. Amin, "Multifrequency-based range estimation of RFID tags," in *2009 IEEE International Conference on RFID*, April 2009, pp. 147–154.

[138] L. Qiu, Z. Huang, S. Zhang, C. Jing, H. Li, and S. Li, "Multifrequency phase difference of arrival range measurement: principle, implementation, and evaluation," *International Journal of Distributed Sensor Networks*, 2015.

[139] X. G. Xia and G. Wang, "Phase unwrapping and a robust Chinese remainder theorem," *IEEE Signal Processing Letters*, vol. 14, no. 4, pp. 247–250, April 2007.

[140] "CST Microwave Studio," CST–Computer Simulation Technology, Darmstadt, Germany. [Online]. Available: https://www.cst.com/applications/mwandrf

[141] Honeywell Inc., USA. [Online]. Available: https://www.honeywell.com/industries/scanning-and-mobile-productivity

[142] "Tagformance™ Pro, RFID Testing and Measurement for Tag Development and Selection," Voyantic Ltd., Espoo, Finland. [Online]. Available: http://voyantic.com/products/tagformance-pro

[143] V. Pillai, P. Nikitin, and F. Lam, "Phase hopping to reduce interference and improve radio frequency identification (RFID) tag throughput," May 28 2013, US Patent 8,451,094. [Online]. Available: http://www.google.tl/patents/US8451094